School of Physics and Astronomy

Resonant-State Expansion for Optical Systems with Frequency Dispersion

Hame Singh Sehmi

PhD Thesis

School of Physics and Astronomy

Cardiff University

February 21, 2019

DECLARATION

This work has not been submitted in substance for any other degree or award at this or any other university or place of learning, nor is being submitted concurrently in candidature for any degree or other award.

Signed …… (candidate) Date 28/06/18

STATEMENT 1

This thesis is being submitted in partial fulfillment of the requirements for the degree of PhD (insert MCh, MD, MPhil, PhD etc, as appropriate)

Signed …… (candidate) Date 28/06/18

STATEMENT 2

This thesis is the result of my own independent work/investigation, except where otherwise stated, and the thesis has not been edited by a third party beyond what is permitted by Cardiff University's Policy on the Use of Third Party Editors by Research Degree Students. Other sources are acknowledged by explicit references. The views expressed are my own.

Signed …… (candidate) Date 28/06/18

STATEMENT 3

I hereby give consent for my thesis, if accepted, to be available online in the University's Open Access repository and for inter-library loan, and for the title and summary to be made available to outside organisations.

Signed …… (candidate) Date 28/06/18

STATEMENT 4: PREVIOUSLY APPROVED BAR ON ACCESS

I hereby give consent for my thesis, if accepted, to be available online in the University's Open Access repository and for inter-library loans **after expiry of a bar on access previously approved by the Academic Standards & Quality Committee.**

Signed …… (candidate) Date 28/06/18

Firstly, I would like to thank my supervisor Dr Egor Muljarov for all the teaching, support and patience given to me. The rare combination of selflessness and academic prowess made it thoroughly enjoyable to be your student and I hope our paths cross again in the future.

Secondly, I thank my second supervisor Prof Wolfgang Langbein for the astute and insightful discussions which contributed an enormous amount to this project, and whose attention to detail has left me with lifelong habit to strive to do the same.

I would also like to thank Sêr Cymru National Research Network in Advanced Engineering and Materials for funding this project and presenting me with many outreach opportunities to share my research with the next generation.

Finally, I would like to thank my family, who have supported me unconditionally and are the most important people in the world to me. I dedicate this thesis to my father, mother, sister and brother.

Abstract

The resonant-state expansion (RSE) is generalised to open optical systems with an arbitrary dispersion of the dielectric constant. In the non-dispersive case we use frequency independent refractive index, moving onto to cases which display dispersion. The RSE converts the Maxwell wave equation into a linear matrix eigenvalue problem in the basis of unperturbed resonant states, in this way numerically exactly finding all relevant eigenmodes of the optical system. The present generalisation is verified by applying it to the analytically solvable system of a spherical metallic nano-particle in vacuum, with the dispersion of the dielectric constant described by the Drude model and extended with the addition of Lorentz poles. Approximating the frequency dispersion of the permittivity of materials with simple analytical functions is of fundamental importance for understanding and modeling the optical response of materials and resulting structures. In the generalised Drude-Lorentz model, the permittivity is described in the complex frequency plane by a number of simple poles having complex weights, which is a physically relevant and mathematically simple approach: By construction, it respects causality and represents physical resonances of the material, and can be implemented easily in numerical simulations. We report here an efficient method of optimising the fit of measured data with the Drude-Lorentz model having an arbitrary number of poles. We show examples of such optimisations for metals and semiconductors, for different frequency ranges. We use this to produce accurate parameters for us to realistically simulate large perturbations starting from dielectric materials such as sand, to dispersive materials such as gold and gallium arsenide. We also analyse the evolution of surface plasmons in gold and use the RSE to perturb gallium arsenide into the gain threshold.

Publications and Presentations

H S Sehmi, W Langbein, and E A Muljarov. Optimizing the Drude-Lorentz model for material permittivity: Method, program, and examples for gold, silver, and copper. *Physical Review B*, 95(11):1–8, 2017.

H S Sehmi, W Langbein, and E A Muljarov. Optimizing the Drude-Lorentz model for material permittivity: Examples for semiconductors. In *Progress in Electromagnetics Research Symposium*, volume Part F1343, pages 994–1000, 2017.

Oral

H S Sehmi, W Langbein, and E A Muljarov. Optimizing the Drude-Lorentz model for material permittivity: Examples for semiconductors. *Progress In Electromagnetic Research Symposium (PIERS)*, St. Petersburg, Russia (May 2017).

Poster

H S Sehmi, W Langbein, and E A Muljarov. Optimizing the Drude-Lorentz model for material permittivity: Method, program, and examples for gold, silver, and copper. *ECR poster competition*, Cardiff, UK, (June 2017).

H S Sehmi, W Langbein, and E A Muljarov. Optimizing the Drude-Lorentz model for material permittivity: Method, program, and examples for gold, silver, and copper. *Symposium on Bio-Nano-Photonics*, Cardiff, UK, (September 2017).

Contents

Chapter 1

Introduction

1.1 Resonant states

The concept of resonant states (RSs) is a mathematically rigorous way of treating the resonances which, formally, are the eigenmodes of the system. These are found by solving Maxwell's wave equation satisfying outgoing wave boundary conditions, specifically electromagnetic waves. In open optical systems the RS eigenfrequencies ω_n are generally complex which physically reflects the fact that the energy leaks out of the system. The real part of ω_n corresponds to the frequency position of the resonance in an optical spectrum of the system and the imaginary part to its half width at half maximum, also determining the quality factor of the resonance as half of the ratio between the two. In quantum mechanics RSs are known as Gamow or Siegert states [1, 2] and have real-valued eigenenergies and orthogonal and normalised wavefunctions. However in open systems the eigenstates have a finite lifetime so the energies will be complex-valued. This leads to the corresponding eigenfunctions non-orthogonal in the usual sense and to grow exponentially in the outer space. The energies and wave vectors have negative imaginary parts resulting in a wave function $\propto \exp[-\Gamma(t - r/v)]$ where $\Gamma = -\operatorname{Im}\omega_n$, v is the phase velocity. This shows the exponential growth as the wave front propagates away from the system which was excited at an earlier time. Because of leakage to outside of the system the stationary bound states are not strictly stationary but are called resonant states (RSs) [3].

As mentioned before the leakage due to complex frequencies means that the RSs which grow exponentially outside of the system cannot be normalised by the usual integration of the square modulus [3]. Instead the normalisation and orthogonality is given by an integral over the finite volume of the system and the energy flux to the outside in the form of a surface term as has been shown in [4].

Moving away from the real-energy axis into the complex plane can cause problems in perturbation theory due to a continuum of stationary scattered states. These can effectively be eliminated from the spectrum and replaced by a countable number of RSs. This is achieved by imposing boundary conditions of no incoming waves, i.e. no waves travelling towards the system. Due to the RSs forming an infinite but countable set of states instead of the uncountable infinite continuum states, we can use matrix diagonalisation algorithms to treat the perturbation. While the RSs are general solutions to Maxwell's wave equations we want to find the solutions to a non-magnetic system with $\mu = 1$.

By using the equations $B = \mu H$ and $D = \varepsilon E$ we can transform Maxwell's equations,

$$\nabla \times E = -\frac{\partial B}{\partial t} \qquad \longrightarrow \qquad \nabla \times E = -\mu \frac{\partial H}{\partial t} \tag{1.1}$$

$$\nabla \times H = J + \frac{\partial D}{\partial t} \qquad \longrightarrow \qquad \nabla \times H = J + \varepsilon \frac{\partial E}{\partial t}\,, \tag{1.2}$$

where the quantities E and H are the electric and magnetic field intensities and the quantities D and B are the electric and magnetic flux densities. D is also called the electric field displacement, and B, the magnetic induction. J is the electric current density.

We can then use Eq. (1.1), Eq. (1.2) and $J = \sigma E$ to give us

$$\begin{aligned} \nabla \times \nabla \times E &= -\mu \frac{\partial}{\partial t} \left(\nabla \times H \right) \\ &= -\mu \frac{\partial}{\partial t} \left[J + \varepsilon \frac{\partial E}{\partial t} \right] \\ &= -\mu \frac{\partial}{\partial t} \left[\sigma E + \varepsilon \frac{\partial E}{\partial t} \right] \end{aligned} \tag{1.3}$$

and apply *outgoing wave* boundary conditions. We do this by introducing the

solution to Maxwells wave equation, the solution being $\widetilde{\mathbf{E}}_n(\mathbf{r},t) = \mathbf{E}_n(\mathbf{r})\exp(-i\omega_n t)$, and substituting it into Eq. (1.3) giving us

$$\nabla \times \nabla \times \mathbf{E}_n(\mathbf{r}) = k_n^2\, \hat{\boldsymbol{\varepsilon}}(\mathbf{r})\mathbf{E}_n(\mathbf{r})\,. \tag{1.4}$$

Here $\mathbf{r}$ is the spatial position, $\hat{\boldsymbol{\varepsilon}}(\mathbf{r})$ is the dielectric constant and $\mathbf{E}_n(\mathbf{r})$ is its electric field eigenfunction in 3D space. The time-dependent part of the RS wave function is given by $\exp(-i\omega_n t)$, where $\omega_n = ck_n$, so that the RSs are solutions of Eq. (1.4) which are either stationary or decaying in time given that $\operatorname{Im}\omega_n < 0$. We use both ω and k throughout this thesis for the frequency depending on the units wanted. As follows from Eq. (1.4) and the divergence theorem, the RSs are orthogonal according to [5]

$$0 = (k_{n'}^2 - k_n^2)\int_V d\mathbf{r}\mathbf{E}_n(\mathbf{r})\,\cdot\,\hat{\boldsymbol{\varepsilon}}(\mathbf{r})\mathbf{E}_m(\mathbf{r}) + \oint_{S_V} dS\left(\mathbf{E}_n\,\cdot\,\frac{\partial\mathbf{E}_m}{\partial s} - \mathbf{E}_m\,\cdot\,\frac{\partial\mathbf{E}_n}{\partial s}\right), \tag{1.5}$$

where the first integral in Eq. (1.5) is taken over an arbitrary simply connected volume V while the second integral is taken over the closed surface S_V, the boundary of V.

Fig. 1.1 shows an example of RSs for a dielectric microsphere which shows the Fabry-Pérot modes at higher frequencies and the whispering gallery modes at lower frequencies. The Fabry-Pérot modes are almost evenly spaced with a near-constant imaginary part of frequency. The high-quality whispering gallery modes are formed in the ray picture due to the total internal reflection within the sphere. We expect the distribution of modes to be symmetric with respect to the imaginary axis due to using the complex conjugate solution as well.

We show in detail how we find the RSs of a sphere in Sec. 3.2.

1.2 Resonant-state expansion

Analytic solutions are often not possible with eigenvalue problems, so many of them which involve perturbation theory are approximately solved, usually by comparing the "solution of interest" to another, ideally analytic, solution. The most common

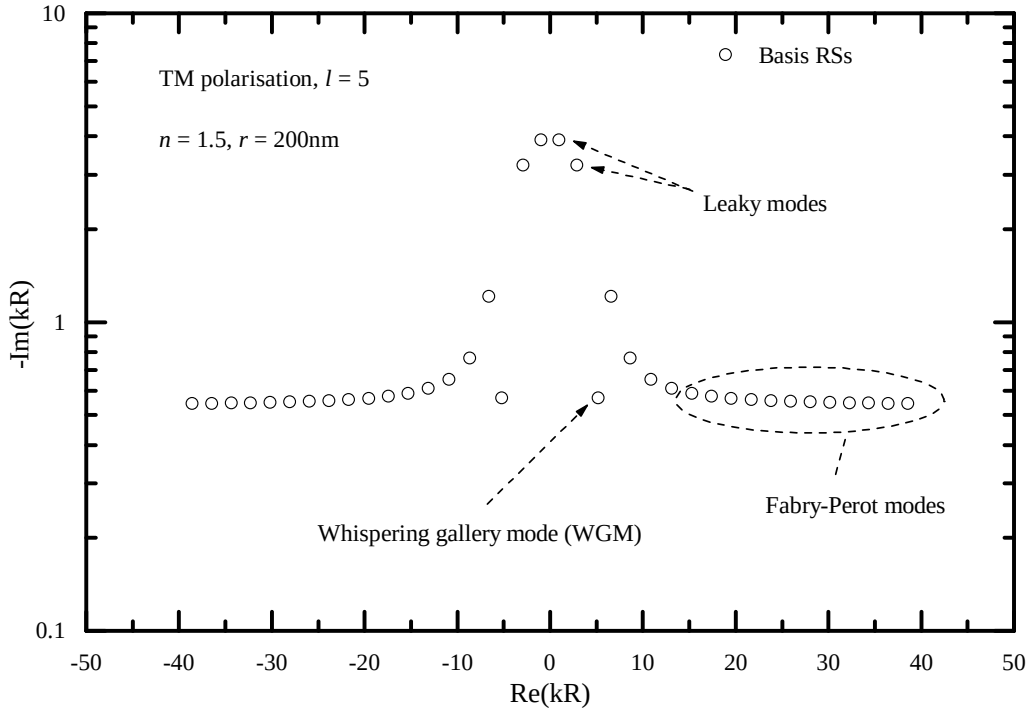

Figure 1.1: RSs for a dielectric sphere with a radius of 200nm, at the fundamental l-number for TM polarisation. Refractive index $n = 1.5$. The sphere has a rich spectrum of modes containing both leaky and high-quality whispering gallery modes (WGM), the latter having a small $\mathrm{Im}\, k_n$.

method in quantum mechanics is to write out the solution as a series expansion in terms of the perturbation which introduces the idea of orders of perturbation [6]. Because the series expansion can become very complex, the solution used will be made up of only a few orders of perturbation, usually the first and second orders. This then leads to poor convergence properties as we increase the perturbation strength [7, 8, 9, 10, 11, 12]. We want to be able to use a method which has greater accuracy which we achieve by getting a finite number of states for the solutions of Maxwell's equations for electromagnetic open systems.

In order to overcome this disadvantage we can formulate the solution as a matrix diagonalisation problem which takes into account all orders of perturbation for the basis used. Because, in theory, we can have an infinite number of basis states, we use a suitable truncatrion in order to make the basis finite. The condition we use, $|nk_n| < k_f$ where $k_f \sim 1$ depending on the material, has the benefit of truncating both far-field RSs and the RS frequencies which arise from introducing dispersion to $\hat{\boldsymbol{\varepsilon}}(\mathbf{r})$ (discussed in Sec. 3.3). This means we can calculate very large perturbations

accurately. Typical perturbation theories will also use a finite number of states but for a finite order of perturbation. Because of the completeness of RSs inside the system, we can expand the RSs of a perturbed system into the unperturbed RSs. This is the basis of the resonant-state expansion (RSE) being a powerful perturbation tool [4, 5, 13, 14].

Other available methods, finite-difference time-domain [15] or finite element method [16, 17], struggle with such sharp resonances due to needing a large time domain (FDTD) because of the slow decay of the optical modes in time. Finite element methods also need excessively large domain in real space to describe the far-field asymptotics properly. The RSE is not hindered by the need to have a large real space domain as it produces the eigenstates and their wave numbers directly from the diagonalisation of the matrix determined by near-field properties only. Furthermore, RSs being discrete eigenstates of the optical system provide a natural discretisation of the problem.

A crucial element of the RSE is the introduction of the Green's function (GF) which provides the complete system response and allows for the calculation of observables such as emission, scattering, or transmission. This is explored in detail in a previous paper where the transmission for a layered planar structure is written in terms of the GF [5]. We also show how you can extract the rest of the observables using the GF in three dimensions in a later paper [18]. The wave vectors of resonant states are the most essential part of the calculation as they most strongly affect the optical properties of the system through the poles of the GF. This pole structure is what eventually allows us to describe the permittivity of materials simply and accurately.

The unperturbed RSs can be used to calculate the GF $\hat{\mathbf{G}}_k(\mathbf{r},\mathbf{r}')$, of the system using the Mittag-Leffler theorem [19, 20]. The GF satisfies the same outgoing wave boundary conditions and Maxwell's wave equation with a delta function source term,

$$-\nabla\times\nabla\times\hat{\mathbf{G}}_k(\mathbf{r},\mathbf{r}')+k^2\hat{\boldsymbol{\varepsilon}}(\mathbf{r})\hat{\mathbf{G}}_k(\mathbf{r},\mathbf{r}')=\hat{\mathbf{1}}\delta(\mathbf{r}-\mathbf{r}')\,, \tag{1.6}$$

where $\hat{\mathbf{1}}$ is the unit tensor and ω is the frequency of the electromagnetic field in

vacuum which is real for treating observables, but it is possible to make an analytic continuation into the complex ω-plane, which is used in the RSE. The GF expansion in terms of the direct (dyadic) product of the RS vector fields is given in previous RSE papers [4, 5, 13].

$$\hat{\mathbf{G}}_k(\mathbf{r},\mathbf{r}') = \sum_n \frac{\mathbf{E}_n(\mathbf{r}) \otimes \mathbf{E}_n(\mathbf{r}')}{2k_n(k-k_n)} \tag{1.7}$$

where the direct vector product (dyadic product) $\otimes$ is defined as $\mathbf{c}(\mathbf{a}\otimes\mathbf{b})\mathbf{d} = (\mathbf{c}\cdot\mathbf{a})(\mathbf{b}\cdot\mathbf{d})$. By substituting Eq. (1.7) into Eq. (1.6) we can write the sum rule

$$\sum_n \frac{\mathbf{E}_n(\mathbf{r}) \otimes \mathbf{E}_n(\mathbf{r}')}{2k_n} = 0 \tag{1.8}$$

to give us

$$\hat{\mathbf{G}}_k(\mathbf{r},\mathbf{r}') = \sum_n \frac{\mathbf{E}_n(\mathbf{r}) \otimes \mathbf{E}_n(\mathbf{r}')}{2k(k-k_n)}. \tag{1.9}$$

Eq. (1.8) along with the closure relation

$$\frac{1}{2}\sum_n \hat{\boldsymbol{\varepsilon}}(\mathbf{r})\,\mathbf{E}_n(\mathbf{r}) \otimes \mathbf{E}_n(\mathbf{r}') = \hat{\mathbf{1}}\delta(\mathbf{r}-\mathbf{r}')\,, \tag{1.10}$$

are what demonstrate the completeness of the RSs.

Eq. (1.9) requires that the RSs are normalised according to

$$1+\delta_{k_n,0} = \int_V d\mathbf{r}\mathbf{E}_n(\mathbf{r})\cdot\hat{\boldsymbol{\varepsilon}}(\mathbf{r})\mathbf{E}_n(\mathbf{r}) + \lim_{k\to k_n}\frac{\oint_{S_V} dS\left(\mathbf{E}_n\cdot\dfrac{\partial\mathbf{E}}{\partial s} - \mathbf{E}\cdot\dfrac{\partial\mathbf{E}_n}{\partial s}\right)}{k^2-k_n^2} \tag{1.11}$$

where $\mathbf{E}(\omega,\mathbf{r})$ is an analytic continuation of the RS wave function $\mathbf{E}_n(\mathbf{r})$ around the point ω_n in the complex ω-plane and $\delta_{\omega_n,0}$ is the Kronecker delta accounting for a factor of two in the normalisation of $\omega_n = 0$ modes. For any spherical surface S_R of radius R, the limit in Eq. (1.11) can be taken explicitly leading for $\omega_n \neq 0$ modes [4, 5] to

$$1 = \int_{V_R} d\mathbf{r}\mathbf{E}_n\cdot\hat{\boldsymbol{\varepsilon}}\mathbf{E}_n + \frac{1}{2k_n^2}\oint_{S_R} dS\left[\mathbf{E}_n\cdot\frac{\partial}{\partial r}r\frac{\partial\mathbf{E}_n}{\partial r} - r\left(\frac{\partial\mathbf{E}_n}{\partial r}\right)^2\right] \tag{1.12}$$

where $r = |\mathbf{r}|$, with the origin at the center of the chosen sphere. Static $\omega_n = 0$

modes, if they exist in the GF spectrum, are normalised according to

$$2 = \int d\mathbf{r}\mathbf{E}_n \cdot \hat{\boldsymbol{\varepsilon}}\mathbf{E}_n \tag{1.13}$$

which comes from reducing Eq. (1.11) given $\omega_n = 0$. Their wave functions decay at large distances as $1/r^2$ or quicker, and the volume of integration in Eq. (1.11) can be extended to the full space for which the surface integral is vanishing.

The completeness of RSs allows us to treat exactly a modified (perturbed) problem

$$\nabla \times \nabla \times \boldsymbol{\mathcal{E}}_\nu(\mathbf{r}) = \varkappa_\nu^2 [\hat{\boldsymbol{\varepsilon}}(\mathbf{r}) + \Delta\hat{\boldsymbol{\varepsilon}}(\mathbf{r})] \boldsymbol{\mathcal{E}}_\nu(\mathbf{r}) \,, \tag{1.14}$$

in which the RS frequency $\varkappa_\nu$ and the electric field $\boldsymbol{\mathcal{E}}_\nu$ are modified as compared to ω_n and $\mathbf{E}_n$, respectively, due to a perturbation $\Delta\hat{\boldsymbol{\varepsilon}}(\mathbf{r})$ with compact support, i.e. vanishing outside a finite volume. Note that this volume contains all the inhomogenieties in $\hat{\boldsymbol{\varepsilon}}(\mathbf{r})$ while the surface integral contains the gradients normal to the surface in the homogeneous space outside the system. We treat this problem by solving Eq. (1.14) with the help of the GF,

$$\boldsymbol{\mathcal{E}}_\nu(\mathbf{r}) = -\varkappa_\nu^2 \int d\mathbf{r}' \hat{\mathbf{G}}_{\varkappa_\nu}(\mathbf{r}, \mathbf{r}') \Delta\hat{\boldsymbol{\varepsilon}}(\mathbf{r}') \boldsymbol{\mathcal{E}}_\nu(\mathbf{r}') \,. \tag{1.15}$$

We use the spectral representaion of the GF [5]

$$\boldsymbol{\mathcal{E}}_\nu(\mathbf{r}) = -\varkappa_\nu^2 \sum_n \mathbf{E}_n(\mathbf{r}) \frac{\int d\mathbf{r}' \mathbf{E}_n(\mathbf{r}') \cdot \Delta\hat{\boldsymbol{\varepsilon}}(\mathbf{r}') \boldsymbol{\mathcal{E}}_\nu(\mathbf{r}')}{2\varkappa_\nu(\varkappa_\nu - k_n)} \,, \tag{1.16}$$

to expand all of the perturbed wave functions into the unperturbed ones. This allows us to write the perturbed states as linear combinations of the normalised unperturbed RSs,

$$\boldsymbol{\mathcal{E}}_\nu(\mathbf{r}) = \sum_n b_{n\nu} \mathbf{E}_n(\mathbf{r}) \,. \tag{1.17}$$

This is the *RSE method*. The use of the unperturbed GF is an essential element of the RSE as Eq. (1.15) guarantees that the perturbed wave functions satisfy the outgoing boundary condition. By substituting Eq. (1.17) into Eq. (1.16) and equating coefficients with the same basis functions $\mathbf{E}_n(\mathbf{r})$ we arrive at a linear matrix

eigenvalue problem

$$\varkappa_\nu \sum_m (\delta_{nm} + V_{nm}/2) b_{m\nu} = \omega_n b_{n\nu} \,, \tag{1.18}$$

which is reduced, using a substitution $b_{n\nu} = c_{n\nu}\sqrt{\varkappa_\nu / k_n}$, to the matrix equation [4]

$$\sum_m \left(\frac{\delta_{nm}}{k_n} + \frac{V_{nm}}{2\sqrt{k_n k_m}} \right) c_{m\nu} = \frac{1}{\varkappa_\nu} c_{n\nu} \,. \tag{1.19}$$

We use Eq. (1.19) as it can be solved by diagonalising a symmetric complex matrix while Eq. (1.18) is a generalised eigenvalue problem.

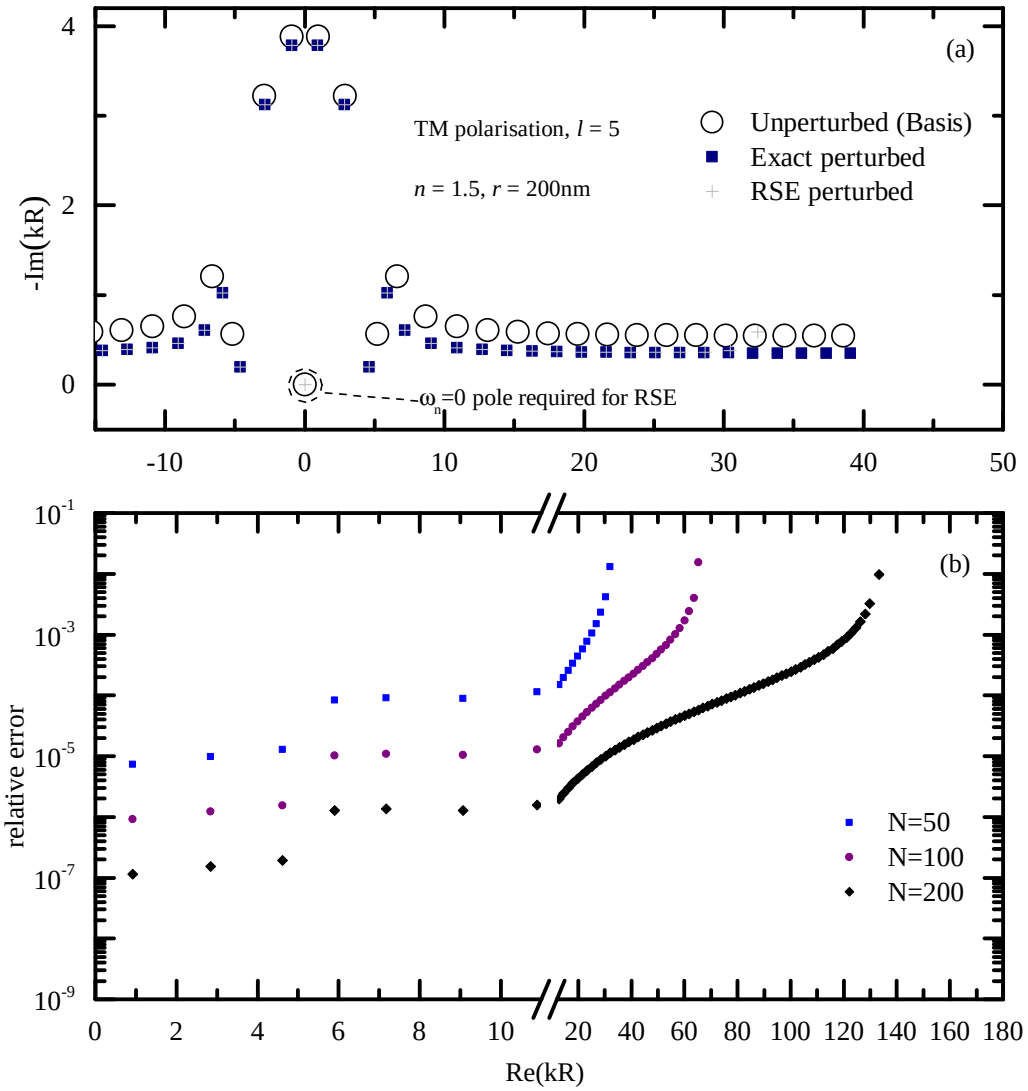

Figure 1.2: RSs for a dielectric sphere at the fundamental l-number for TM polarisation, perturbed from $n = 1.5$ to $n = 2.5$. We also show the relative error and how is changes as we increase the basis size (N = number of RSs in the basis).

This allows us to find the wave frequencies $\varkappa_\nu$ and the expansion coefficients $c_{n\nu}$

of the perturbed RSs. The matrix elements of the perturbation are given by

$$V_{nm} = \int \mathbf{E}_n(\mathbf{r}) \cdot \Delta\hat{\boldsymbol{\varepsilon}}(\mathbf{r})\mathbf{E}_m(\mathbf{r})\, d\mathbf{r}\,. \tag{1.20}$$

Using constant values for $\Delta\hat{\boldsymbol{\varepsilon}}(\mathbf{r})$ we can describe the perturbation of a dielectric microsphere showing the sharp resonances in the spectrum, for example caused by whispering gallery modes (WGMs). We will refer to the RS frequencies as 'poles' due to them presenting the simple poles of the GF.

Fig. 1.2 is a demonstration of the RSE for a purely dielectric sphere with the same parameters as Fig. 1.1. To clarify, a dielectric material is one with bound charges but will still exhibit absorption at certain frequencies, this leads to the permittivity being frequency independent. In the first graph we can see that the RSE results line up well with the exact solution for low frequencies. The method of finding the basis states and the exact perturbed solution is explained in full in Sec. 3.2. Also discussed in Sec. 3.2 is the zero frequency pole ($\omega_n = 0$) which is required for completeness and the accuracy of the method for TM polarisation [5].

We also show the relative error of the RSE result with respect to the exact solution for different numbers of RSs in the basis. We can see that the error scales as $\frac{1}{N^3}$ showing very quick convergence to the exact solution.

1.3 Materials with dispersion

For purely dielectric materials the phase velocity does not depend on the frequency, which means we can measure the instantaneous response of the electric field to the presence of a material. This is known as the electric field displacement ($D = \varepsilon E$) where ε is the permittivity which is constant for dielectric materials. Materials with a frequency-dependent dielectric constant are referred to as dispersive. This is where we can measure the 'memory' of the material after the presence of it in an electric field.The frequency dependence comes about because when a time-varying electric field is applied, the polarization response of the material cannot be instantaneous. Such dynamic response can be described by the convolutional (and causal) constitutive relationship [21]

$$\widetilde{D}(\mathbf{r},t) = \int_{-\infty}^{t} \widetilde{\varepsilon}(\mathbf{r},t-t')\widetilde{E}(\mathbf{r},t')dt' \tag{1.21}$$

where the permittivity $\widetilde{\varepsilon}(\mathbf{r},t)$, is now a function of time. By taking the Fourier transform (FT) of Eq. (1.21) we get an equation which depends on frequency according the to convolution theorem. The FT of $\widetilde{D}(\mathbf{r},t)$ is $D(\mathbf{r},\omega)$ which is given by

$$D(\mathbf{r},\omega) = \varepsilon(\mathbf{r},\omega)E(\mathbf{r},\omega), \tag{1.22}$$

where $\varepsilon(\mathbf{r},\omega)$ and $E(\mathbf{r},\omega)$ are the FT of $\widetilde{\varepsilon}(\mathbf{r},t)$ and $\widetilde{E}(\mathbf{r},t)$ respectively. Note that $\varepsilon(\omega) = (n+i\kappa)^2$ where n is the refractive index and κ is the absorption index, both being measurable quantities and functions of ω. This is discussed in Sec. 1.3.1.

1.3.1 Experimental data

Our main source of experimental data for dispersive materials is the Johnson and Christy paper [22] on the optical properties of the noble metals: gold, silver and copper. The tables of data in the paper provide values for n and κ, as well as the experimental errors, for the frequency range between 0.64 eV and 6.6 eV. This is the optical range where we see dispersion when plotting permittivity against frequency.

From Fig. 1.3 we can see that the infra-red range where n is small and κ is large, the free electron behaviour dominates which is described well by the Drude model, see Sec. 1.3.2 and Sec. A, as a realistic and analytic model. This results in larger percentage errors for n than κ. We can also see that the interband absorption range dominates the visible (1.77-3.26 eV) and UV (3.26 eV and above) range where n and κ are on the order of unity.

While the results from the JC paper are not universal they are a well known starting point for theoretical analysis with errors of about 12% for n and about 4% for κ. The data was retrieved from conducting experiments on thin films of the material in question. The refractive index $n(\omega)$ and absorption index $\kappa(\omega)$ are determined at a number of real frequencies ω_j providing $n_j = n(\omega_j)$ and $\kappa_j = \kappa(\omega_j)$.

We then define $\Delta\varepsilon_j = \Delta\varepsilon(\omega_j)$, treating all quantities in Eqs. (1.23) and (1.24)

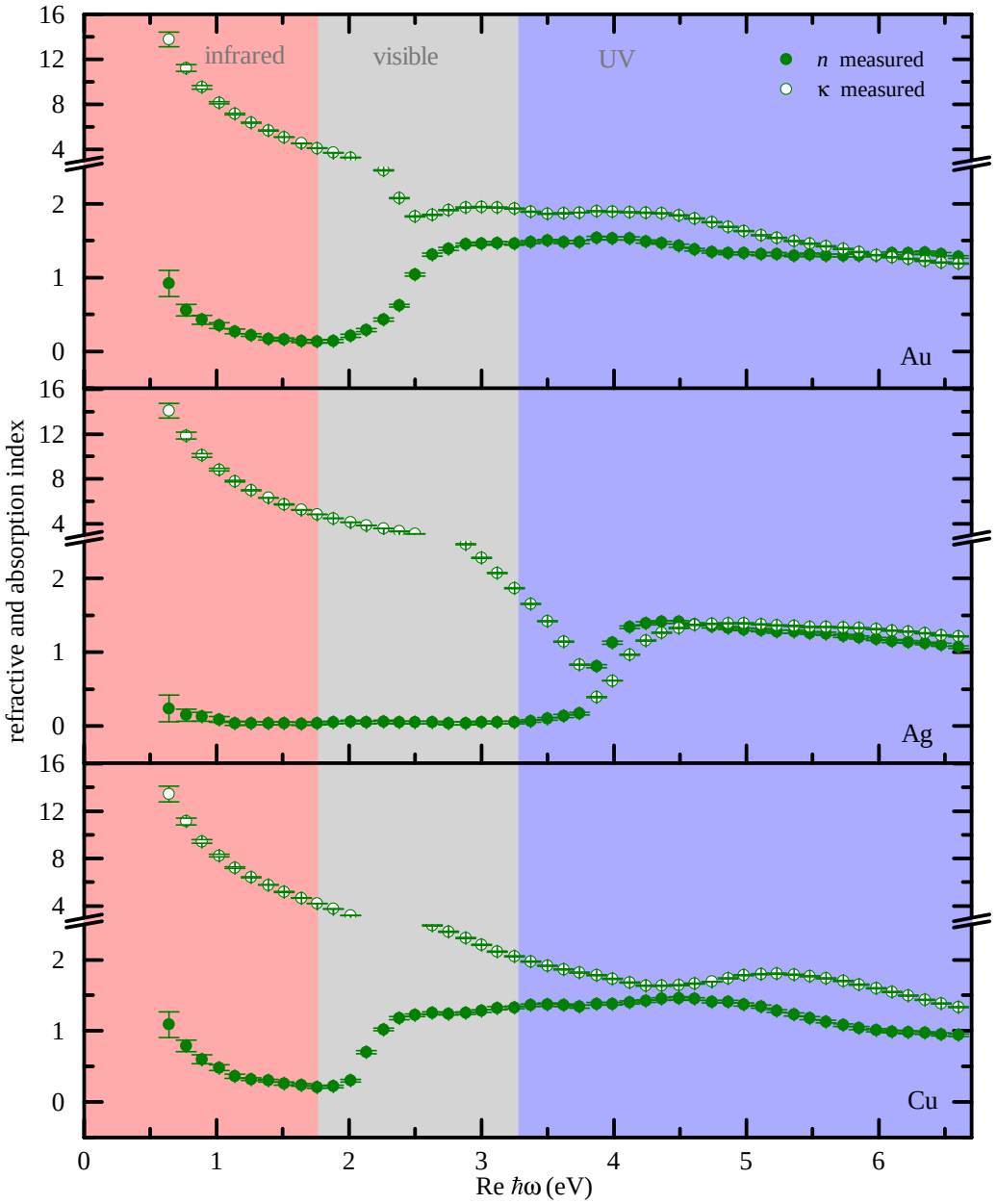

Figure 1.3: The refractive and absorption index from Johnson and Christy's paper for gold, silver and copper [22]. The shaded regions are guides for the eye to see the frequency ranges.

as functions of ω. The quantities $\varepsilon' = n^2 - \kappa^2$ and $\varepsilon'' = 2n\kappa$ are purely real. We introduce a fit method in chapter 2 in which we choose to fit ε instead of n and κ due to the linear parameters present in ε, see Sec. 2.3 for more details. These quantities are shown in Fig. 1.4. The measured values are assumed here to have an error defined by the root-mean square (RMS) deviation, Δn_j and $\Delta \kappa_j$, respectively. We therefore calculate $\varepsilon = \varepsilon' + i\varepsilon'' = (n + i\kappa)^2$ and determine its RMS error $\Delta\varepsilon$ by

assuming statistically independent errors Δn and $\Delta\kappa$, which yields

$$\Delta\varepsilon' = \sqrt{\left(\frac{\partial\varepsilon'}{\partial n}\Delta n\right)^2 + \left(\frac{\partial\varepsilon'}{\partial\kappa}\Delta\kappa\right)^2} = 2\sqrt{(n\Delta n)^2 + (\kappa\Delta\kappa)^2}\,, \tag{1.23}$$

$$\Delta\varepsilon'' = \sqrt{\left(\frac{\partial\varepsilon''}{\partial n}\Delta n\right)^2 + \left(\frac{\partial\varepsilon''}{\partial\kappa}\Delta\kappa\right)^2} = 2\sqrt{(\kappa\Delta n)^2 + (n\Delta\kappa)^2}\,. \tag{1.24}$$

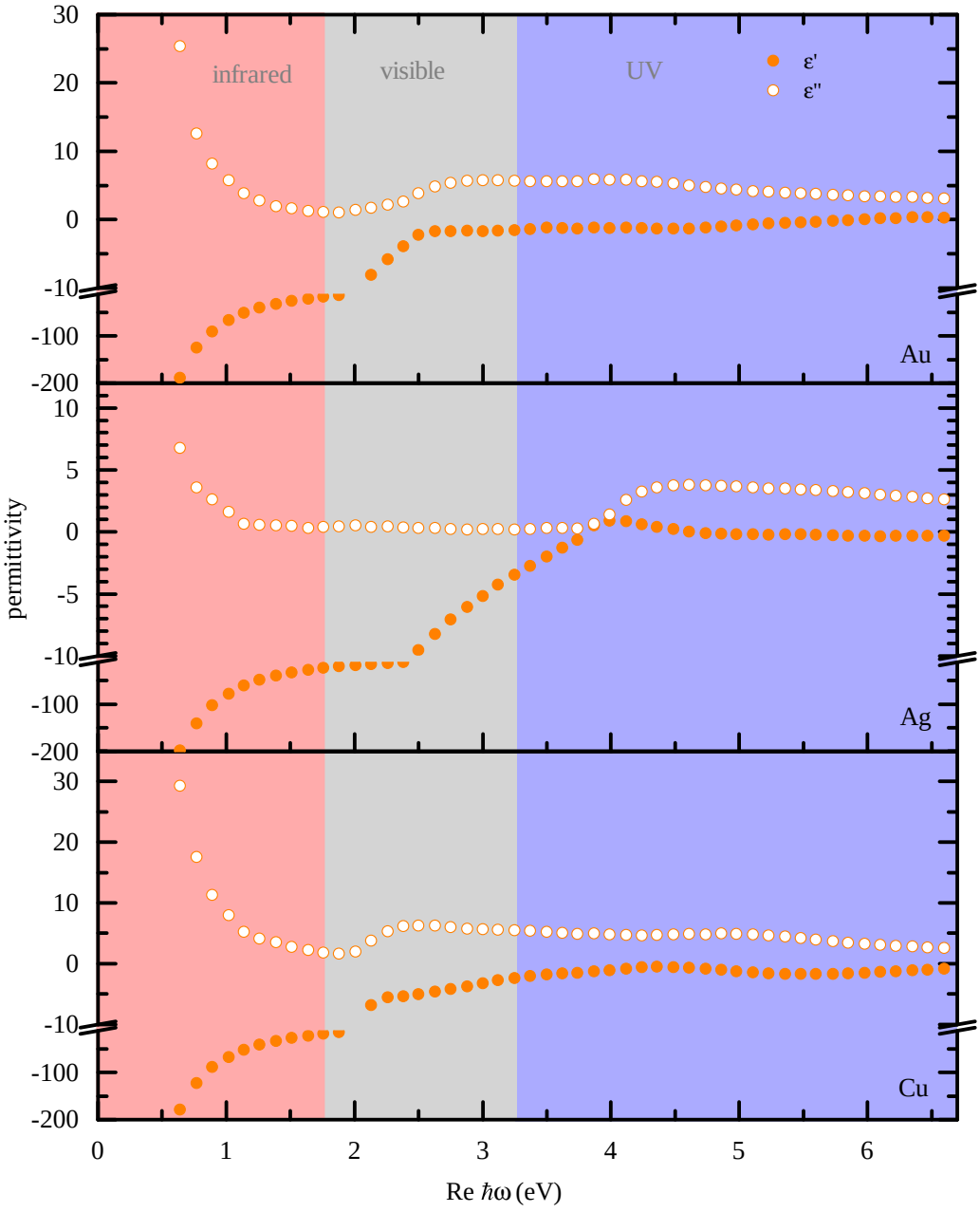

Figure 1.4: As in Fig. 1.3 but for real and imaginary parts of ε.

1.3.2 Ohm's law and the Drude model

While it is always possible to resort to interpolations of experimental data, the advantages of having a simpler analytic model for the permittivity are tremendous. Ideally we want an accurate model with a small number of physically meaningful parameters. This makes analysis of $\varepsilon(\omega)$ easier to understand when considering modification due to any external perturbations. A recurring model in literature is the Drude model which describes metals well for certain frequency ranges [23]. The model owes its simplicity to neglecting any electron interactions and assumes a high number of "free electrons". The model is derived from taking the Fourier transform of the equation of motion and using the definition of a dipole moment to arrive at an expression for the susceptibility. We derive the Drude model fully in Sec. A. In the Drude model we can write the expression for the permittivity as

$$\varepsilon(\omega) = 1 + \frac{\omega_p^2}{\omega(\omega + i\gamma)} \tag{1.25}$$

where ω_p^2 is the plasma frequency and γ is the damping rate. As we will expand on in Sec. 2.2, we can write ω_p^2 in terms of the complex conductivity σ and the high frequency term ε_∞; $\omega_p^2 = \frac{\gamma\sigma}{\varepsilon_\infty}$. We can visualise the Drude pole of the permittivity as having a frequency position on the imaginary axis at $-i\gamma$.

Another model we can use is the Ohm's law dispersion which arises from splitting Eq. (1.25) into multiple terms and neglecting the high frequency asymptotes which are $\varepsilon \propto \omega^{-2}$:

$$\varepsilon(\omega) = \varepsilon_\infty + \frac{i\sigma}{\omega} - \cancel{\frac{i\sigma}{\omega + i\gamma}} \tag{1.26}$$

The Ohm's law model is only suited for very low frequencies ($\omega << \gamma$) and is therefore not practical.

1.3.3 Beyond the Drude Model

The Drude model has its limits and while being able to accurately describe the visible/near-uv region for certain materials, if the interband transitions are close to this range we need to introduce extra terms. Simple Lorentz oscillator terms,

discussed in Sec. 2.2.1, can be used to describe any feature of the line shape but suffer from the same problem as the interpolation of the experimental data would, meaning you would need too many of them which gives you a complicated expression with many parameters leading to an intractable number of transitions. This is due to the transitions being asymmetric in terms of the line shape leading to the inclusion of many artificial transitions which give no insight into the dispersion of the material.

In a paper by Etchegoin et al [23], a model called the critical point model is discussed which, like the Drude model, has poles at a particular frequency with a complex weight. This type of analytic model can describe the interband transitions in metals and semiconductors with minimal parameters even when many "critical points" are used. When looking at $\varepsilon(\omega)$ the critical points $L_k(\omega)$, or *Lorentz poles* as we will call them throughout this thesis, take the form of

$$L_k(\omega) = \frac{i\sigma_k}{\omega - \Omega_k} + \frac{i\sigma_k^*}{\omega - \Omega_k^*} \tag{1.27}$$

where σ_k is the complex conductivity and Ω_k is the position in frequency space.

It is possible to include a family of analytic models for transitions in solids, which satisfy a certain set of minimum requirements and reproduce most of the line shapes in $\varepsilon(\omega)$ observed experimentally. A mixture of the Drude model and the critical point model discussed will give rise to an analytic model which fits any set of experimental data given.

1.4 Plan of this thesis

We have discussed the RSE for non-dispersive materials in Sec. 1.2 which is suitable for dielectric materials, however metals, semiconductors, and even realistic dielectric materials (glass), all have frequency dispersion which requires an analytic model to descibe the permittivity. This drastically changes the perturbation matrix Eq. (1.20) and as a result changes the RSE method. Substituting $\hat{\boldsymbol{\varepsilon}}(\mathbf{r}, \omega)$ into Eq. (1.20) makes the RSE non-linear and in need of significant reformulation (see chapter 3).

In chapter 2 we introduce a method of fitting experimental data for the permittivity to what we call the Drude-Lorentz model. The method is semi-analytic,

meaning half of the parameters are solved quickly by matrix diagonalisation with unique solutions, and another part by gradient decent, which is iterative and thus slower, and can lead to several solutions. The method takes into account the experimental errors where they are given. This makes it fast and reliable at fitting the Drude-Lorentz model to a set of experimental data and gives us a good base to model the material using RSs and perturb them using the RSE which requires this form of the dispersion. This work has already been published for metals [24] and semiconductors [25].

In chapter 3 we introduce the method behind using a dispersive permittivity in the RSE and what we need to alter, in order to implement the method correctly. We call this the dispersive RSE. We test an unperturbed dispersive basis states which is perturbed to another set of dispersive basis with a different $\varepsilon(\omega)$. We use the fit program to give us accurate parameters for materials which we use for non-dispersive to dispersive perturbation for realistic materials. We also explore the evolution of surface plasmons with respect to nanosphere radius for gold and how to model gain for GaAs at the first interband transition using the RSE.

Chapter 2

Drude-Lorentz model and fit program

2.1 Motivation

The interest in nanotechnology has increased greatly over the past decade, particularly in nanophotonics, which exploits optical properties of structures on the nanoscale, composed of different materials. Working with objects which approach or are smaller than the wavelength of visible light come with its own challenges, the scattering and transmission properties can vary significantly. This can lead to metamaterials where materials can be engineered to produce properties which do not exist natuarally, for example, lenses which have a negative refractive index for imaging of nanoparticles.

In order to design photonic structures and predict and optimise their properties, such as optical field enhancement, chirality, or enhanced radiative emission via the Purcell effect, the electromagnetic response of the underlying materials has to be simulated. An effective medium approach of the optical response is suited for many structures in which nonlocal effects can be neglected. The properties describing the linear optical response of non-chiral media are the frequency dependent permittivity tensor $\hat{\boldsymbol{\varepsilon}}(\omega)$ and permeability tensor $\hat{\boldsymbol{\mu}}(\omega)$. In most relevant natural materials, the permeability is close to unity, so that we concentrate here on $\hat{\boldsymbol{\varepsilon}}(\omega)$. However, the method is applicable equivalently to $\hat{\boldsymbol{\mu}}(\omega)$ or, in general, to other material response

functions.

Using an analytical model of $\hat{\varepsilon}(\omega)$, which contains only simple poles, is motivated by physical arguments, such as the presence of resonances in the material self energy and response functions. Furthermore, this form of the permittivity can be efficiently implemented in numerical methods, such as the finite difference in time domain (FDTD) method [26], and in the more analytic and rigorous approaches, such as the dispersive resonant-state expansion[27]. The pole structure of the permittivity naturally includes a zero-frequency pole of the Ohm's law dispersion, which however works well only in the long wavelength limit and is not suited to describe the material properties in the optical range. Real metals are much better described by the Drude model[22], which takes into account the finite mass of the charge carriers. Adding real-valued Lorentz components[28] to the Drude model is suited to represent electronic interband transitions. A further refinement of the model uses complex weights (residues) of the Lorentz poles[23]. This is known in some of the literature as the critical point model[26, 29, 30]. We use this generalisation in the present work and call it a Drude-Lorentz (DL) model.

A fit of the material permittivity with the DL model has been performed in a number of publications [23, 26, 29, 30] for its further use in FDTD solvers. However, the experimental errors available in the literature[22] have not been taken into account in those fits. Here we provide an efficient algorithm of fitting experimental data, using available errors, with the DL model with an arbitrary number of Lorentz poles. This algorithm combines an exact analytical approach for determining the linear parameters of the model, with a numerical solver for optimising its nonlinear parameters. We illustrate the resulting pole positions and their weights in the complex plane to give some physical insight how the model approximates the electronic transitions in real materials.

2.2 Drude-Lorentz general model

The analytic model for the permittivity of materials can be seen as a collection of resonances. Without an applied electric field, the electrons around the nuclei are

symmetric and at rest however they will start to resonante with the introduction of an electromagnetic wave. We can extrapolate from this response to an electric field with the Drude-Lorentz model. This is derived fully from simple harmonic motion of the resonant electrons in the appendix, Sec. A.

Quite generally, the permittivity $\hat{\boldsymbol{\varepsilon}}(\mathbf{r},\omega)$ can be treated as an analytic function in the complex frequency plane, having a countable number of simple poles and therefore, according to the Mittag-Leffler theorem, can be expressed as

$$\hat{\boldsymbol{\varepsilon}}(\omega) = \hat{\boldsymbol{\varepsilon}}_\infty + \sum_j \frac{i\hat{\boldsymbol{\sigma}}_j}{\omega - \Omega_j}\,, \tag{2.1}$$

where $\hat{\boldsymbol{\varepsilon}}_\infty$ is the high-frequency value of the permittivity and Ω_j are the resonance frequencies, which are the poles of the permittivity, determining its dispersion, with the weight tensors $\hat{\boldsymbol{\sigma}}_j$ corresponding to generalised conductivities of the medium at these resonances. The Lorentz reciprocity theorem requires that all tensors in Eq. (2.1) are symmetric, and the causality principle requires that $\hat{\boldsymbol{\varepsilon}}(\omega)$ has no poles in the upper half plane of ω and that $\hat{\boldsymbol{\varepsilon}}^*(\omega) = \hat{\boldsymbol{\varepsilon}}(-\omega^*)$[21]. Therefore, for a physically relevant dispersion, each pole of the permittivity with a positive real part of Ω_j has a partner at $\Omega_{-j} = -\Omega_j^*$ with $\hat{\boldsymbol{\sigma}}_{-j} = \hat{\boldsymbol{\sigma}}_j^*$. Poles with zero real part of Ω_j have real $\hat{\boldsymbol{\sigma}}_j$. For simplicity, we assume in the following an isotropic response, such that the conductivities and thus the permittivity are described by scalars. We note however that it is straightforward to extend the presented treatment to a nonisotropic response.

We first separate the poles with zero real part of the frequency, which describe the conductivity of materials in the Drude model:

$$\varepsilon_{\mathrm{D}}(\omega) = \varepsilon_\infty + \frac{i\sigma}{\omega} - \frac{i\sigma}{\omega + i\gamma} = \varepsilon_\infty - \frac{\gamma\sigma}{\omega(\omega + i\gamma)}\,, \tag{2.2}$$

where ε_∞ is the permittivity at high frequencies and σ is the real DC conductivity. The pole at zero frequency represents Ohm's law, corresponding to the ω^{-1} low-frequency limit of the dispersion. Together with the second pole, at $-i\gamma$, it provides the ω^{-2} high-frequency asymptotics, originating from the nonzero mass of the charge

carriers. In real materials, the carrier mass and the damping can show a frequency dependence, which is not included in the Drude model. To describe such effects, the DC conductivity can be split [31] into several Drude contributions, with fractions η_d and dampings γ_d, so that

$$\varepsilon_{\mathrm{D}}(\omega) = \varepsilon_\infty + \frac{i\sigma}{\omega} - \sigma \sum_{d=1}^{D} \frac{i\eta_d}{\omega + i\gamma_d}\,, \tag{2.3}$$

where $\sum_{d=1}^{D} \eta_d = 1$. Adding the poles Ω_k with nonzero real part, which are called Lorentz poles and describe material resonances at finite resonance frequencies, such as phonons or electronic interband transitions, we arrive at

$$\varepsilon(\omega) = \varepsilon_{\mathrm{D}}(\omega) + \sum_{k=1}^{L} \left(\frac{i\sigma_k}{\omega - \Omega_k} + \frac{i\sigma_k^*}{\omega + \Omega_k^*} \right)\,, \tag{2.4}$$

where L is the number of pairs of Lorentz poles. The generalised conductivities $\sigma_k = \sigma_k' + i\sigma_k''$ are complex. We denote real and imaginary parts of complex quantities with prime and double prime, respectively, and keep using this notation throughout the thesis.

The model of the permittivity $\varepsilon(\omega)$ given by the analytic function Eq. (2.4) with $\Omega_k'' \leq 0$ respects the constrain of causality by construction. The parameters of the model, which are the conductivities and the resonance frequencies, have to be determined from the experimentally measured data.

2.2.1 Classical Lorentz oscillator and optical gain

To describe the interaction between atoms and electric fields in classical terms, we say that the electron (a particle with some small mass) is bound to the nucleus of the atom (with a much larger mass) by a force that behaves according to Hooke's Law - that is, a spring-like force. An applied electric field would then interact with the charge of the electron, causing 'stretching' or 'compression' of the spring, which would set the electron into oscillating motion. This is what we call a classic Lorentz oscillator (CLO).

Using a pendulum as an aid we can visualises these resonances. At low frequen-

cies the driving force is present on the object and it has the same phase as the displacement of the object, this is analogous to the displacements of electrons in an electric field. The permittivity for a CLO is,

$$\varepsilon(\omega) = \varepsilon_\infty + \frac{\omega_p^2}{(\omega_0^2 - \omega^2) + i\omega\gamma}\,, \tag{2.5}$$

where ω_p^2 is the plasma frequency and ω_0 is the resonance. Since the polarisation vector and electric field are related by the electric susceptibility, we analyse the magnitude and phase of χ (see Sec. A for more details), where $\chi(\omega) = \varepsilon(\omega) - \varepsilon_\infty$. By splitting $\varepsilon(\omega)$ into real and imaginary parts we get

$$\varepsilon_r(\omega) - 1 = \frac{\varepsilon'(\omega) - \varepsilon_\infty}{\varepsilon_\infty} = \frac{\omega_p^2(\omega_0^2 - \omega^2)}{(\omega_0^2 - \omega^2)^2 + \omega^2\gamma^2} \tag{2.6}$$

$$\varepsilon_i(\omega) = \frac{\varepsilon''(\omega)}{\varepsilon_\infty} = \frac{\omega_p^2\gamma\omega}{(\omega_0^2 - \omega^2)^2 + \omega^2\gamma^2}. \tag{2.7}$$

The amplitude and the phase can be written as $|\chi(\omega)| = \sqrt{(\varepsilon_r(\omega) - 1)^2 + \varepsilon_i(\omega)^2}$ and $\phi_\chi = \arctan(\varepsilon_i(\omega)/(\varepsilon_r(\omega) - 1))$. The amplitude is 'medium' for low frequencies due to $|\chi(0)| \approx \omega_p^2/\omega_0^2$ when $\omega \approx 0$, with the phase being $\phi_\chi \approx \arctan(0) = 0$. At the resonance frequency, $\omega = \omega_0$, the amplitude is the highest due to $|\chi(\omega_0)| \approx \omega_p^2/\omega_0\gamma$ where $\gamma << \omega_0$ and the phase is $\phi_\chi \approx \arctan(\infty) = \pi/2$ meaning the driving force and the displacement are $\pi/2$ out of phase. For high frequencies the amplitude vanishes as the driving force and displacement are π out of phase due to $|\chi(\infty)| = 0$ and $\phi_\chi \approx \arctan(0) = 0$ or π. This is shown in Fig. 2.1.

When compared to the complex weighted Lorentz poles, the classical Lorentz oscillator has a purely imaginary conductivity which translates to a purely real Lorentz weight. This leads to a phase of $\pi/2$ which is appropriate when describing isolated features, i.e. individual interband transitions. We will use this method for modelling optical gain in GaAs by fitting the first interband transition with Lorentz oscillators only and changing the sign of the purely imaginary conductivity σ of the lowest frequency oscillator, corresponding to the transitions close to the band gap, leading to $i\sigma$ being purely real in Eq. (1.27). The fit of the first GaAs interband transition is explored in detail in Sec. 3.6 as well as how we can perturb an absorptive

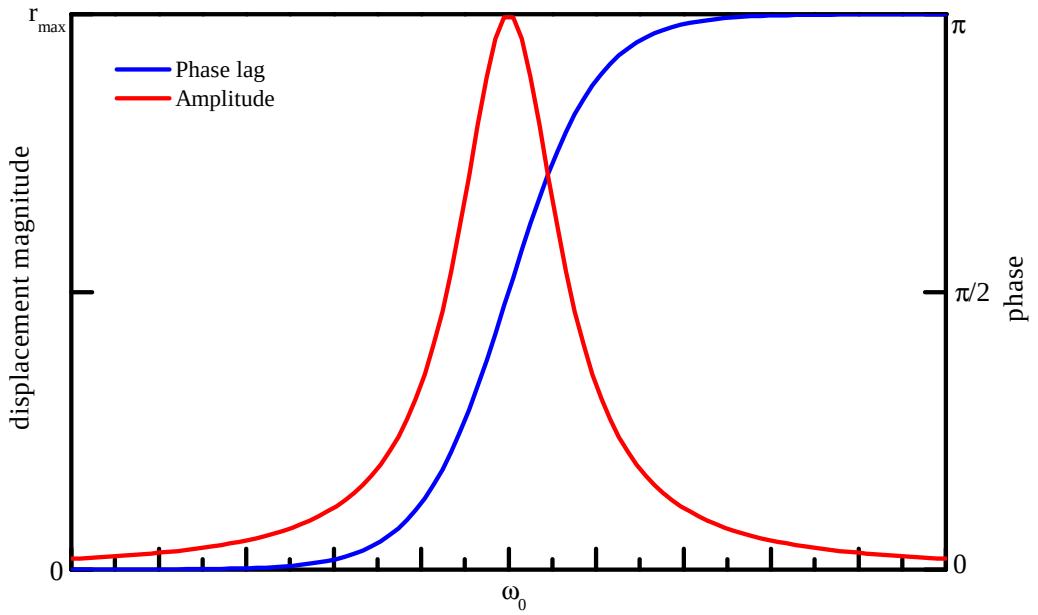

Figure 2.1: Sketch of amplitude and phase lag of a harmonic oscillator, where $\mathbf{r}_{\max}$ is the maximum displacement.

system to one with optical gain.

2.3 Fit procedure and algorithm

With the analytic model Eq. (2.4) of the permittivity, the task of fitting the experimental data reduces to finding the parameters of the model which minimise the error weighted deviation E between the analytic and the measured values of ε, as this maximises the probability of the model given the data. Assuming Gaussian errors, we use the squared deviation, weighted with the RMS errors:

$$E = \sum_{j=1}^{N} \left(\frac{\varepsilon'(\omega_j) - \varepsilon'_j}{\Delta\varepsilon'_j} \right)^2 + \left(\frac{\varepsilon''(\omega_j) - \varepsilon''_j}{\Delta\varepsilon''_j} \right)^2 , \tag{2.8}$$

where ε_j are experimental values and $\Delta\varepsilon_j$ are the corresponding errors discussed in Sec. 1.3.1. Considering that typical experimental data sets consist of tens to hundreds of points, and $\varepsilon(\omega)$ is an analytic function of ω with a large number of parameters, typically in the order of ten, a robust and efficient algorithm is needed. To achieve this goal, we first make use of an exact, analytical minimisation with respect to the parameters in which ε is linear – these are all the conductivities

and ε_∞. This is the reason why it is advantageous to fit ε instead of the complex refractive index $n + i\kappa$, as for the latter none of the parameters is linear. Then for the rest of the parameters, in which ε is nonlinear – these are the pole frequencies – we use an iterative minimisation with a gradient decent and a suited selection of starting points.

We assume that the frequencies ω_j are sorted in ascending order, and that the minimum (maximum) frequency is ω_1 (ω_N).

2.3.1 Exact minimisation over linear parameters

An exact minimisation of the RMS deviation is available for all the parameters in which the model is linear. To make this linear dependence clearer, we write the permittivity as

$$\varepsilon(\omega_j) = \sum_{l=0}^{2L+D} A_l g_l(\omega_j) \tag{2.9}$$

with $1 + D + 2L$ *real linear* parameters A_l and the related complex functions $g_l(\omega_j)$ as given in Table 2.1.

l	A_l	$g_l(\omega)$
0	ε_∞	1
d	$\sigma\eta_d$	$-\dfrac{\gamma_d}{\omega(\omega + i\gamma_d)}$
$2k + D - 1$	σ'_k	$\dfrac{i}{\omega - \Omega_k} + \dfrac{i}{\omega + \Omega_k^*}$
$2k + D$	σ''_k	$\dfrac{-1}{\omega - \Omega_k} + \dfrac{1}{\omega + \Omega_k^*}$

Table 2.1: Linear parameters A_l and related functions $g_l(\omega_j)$ used in the model, with the integers $d = 1..D$ and $k = 1..L$.

Minimisation of the total error E, given by Eq. (2.8), with respect to A_l can be done analytically by setting the derivatives to zero,

$$\frac{\partial E}{\partial A_l} = 2\sum_{j=1}^{N} \left(\frac{g'_l(\omega_j)\left(\sum_m A_m g'_m(\omega_j) - \varepsilon'_j\right)}{(\Delta\varepsilon'_j)^2} + \frac{g''_l(\omega_j)\left(\sum_m A_m g''_m(\omega_j) - \varepsilon''_j\right)}{(\Delta\varepsilon''_j)^2} \right) = 0. \tag{2.10}$$

These provide a set of $1 + D + 2L$ linear equations for A_m which can be written

as

$$\sum_{m=0}^{2L+D} H_{lm} A_m = B_l, \tag{2.11}$$

where

$$H_{lm} = \sum_{j=1}^{N} \left(\frac{g'_l(\omega_j) g'_m(\omega_j)}{(\Delta\varepsilon'_j)^2} + \frac{g''_l(\omega_j) g''_m(\omega_j)}{(\Delta\varepsilon''_j)^2} \right), \tag{2.12}$$

$$B_l = \sum_{j=1}^{N} \left(\frac{g'_l(\omega_j) \varepsilon'_j}{(\Delta\varepsilon'_j)^2} + \frac{g''_l(\omega_j) \varepsilon''_j}{(\Delta\varepsilon''_j)^2} \right). \tag{2.13}$$

Equation (2.11) can be solved using standard linear algebra packages with a computational complexity of $(1 + D + 2L)^2$, which is smaller than the complexity of $N(1 + D + 2L)^2$ for calculating H_{lm} and B_l for typical sizes of datasets and number of poles. We can fix the value of ε_∞ if necessary, removing it from the set of linear parameters, by subtracting our chosen value ε_∞ from $\varepsilon(\omega_j)$ (see an example in Table 2.2).

2.3.2 Minimisation over nonlinear parameters

Using the values of A_l found in Sec. 2.3.1 by exact minimisation of E, we now define, via Eq. (2.8), a new error function $\widetilde{E}$, which has been already minimised with respect to the linear parameters A_l and depends only on the nonlinear parameters, which are the Drude dampings γ_d and the complex frequencies Ω_k of the Lorentz poles. Overall, there are $D + 2L$ real parameters over which $\widetilde{E}$ has to be minimised. To represent the average deviation of the model from the measured data points relative to their experimental RMS error, we introduce

$$S = \sqrt{\frac{\widetilde{E}}{2N}}. \tag{2.14}$$

A fit to the experimental data has two sets of independent errors relative to the correct $\varepsilon(\omega)$: the error of the measurements and the errors of the fit. For a fit which is equal to the correct $\varepsilon(\omega)$, we expect, by definition, $S = 1$. If instead the magnitude of both errors are the same, and they are uncorrelated, we expect $S = \sqrt{2}$. Therefore, for a fit dominated by the measurement errors, the S values are expected

to be close to unity, below $\sqrt{2}$. Furthermore, we note that there are $1{+}2D{+}4L$ fitting parameters and $2N$ data values, which can be of comparable number. Therefore, there are only $2N-1-2D-4L$ values which cannot be exactly fitted by the model function. Indeed, the set of the fit conditions is overdetermined and thus provides a finite error of the fit, resulting in finite values of S below unity. Specifically, we would expect for the best fit a value of $S = \sqrt{1-(1+2D+4L)/(2N)}$. When the expression under the square root is zero or negative, it is possible to fit the data exactly, i.e. S can approach zero – we will see examples of this later.

During the minimisation, we found instances (specifically when fixing ε_∞) where the pole frequency and the corresponding weight diverged simultaneously with fixed ratio, representing a frequency-independent permittivity component $i\hat{\boldsymbol{\sigma}}_j/\Omega_j$. Furthermore, we observed poles at nearly equal positions, or Lorentz poles on the imaginary axis. All these situations correspond to local minima of $\widetilde{E}$ which should be avoided. We also found poles with positive imaginary part, which are not compatible with causality of the response. In order to avoid the corresponding un-physical pole properties while not significantly compromising the resulting error S, we minimise not $\widetilde{E}$, but $\widetilde{E}\zeta$ instead, where

$$\alpha_i = \left(1+\frac{s_1^2\delta^2}{|\Omega_i'|^2}\right)\left(1+\frac{s_2^2\delta^2}{|\Omega_i''|^2}\right) \tag{2.15}$$

$$\beta_i = \prod_{j>i}\left(1+\frac{s_3^2\delta^2}{\left|\Omega_i'-\Omega_j'\right|^2+\left|\Omega_i''-\Omega_j''\right|^2}\right) \tag{2.16}$$

$$\zeta = \prod_i \alpha_i\beta_i\zeta_i,\ \ \zeta_i = \begin{cases} 1 & \text{for } |\Omega_i| < \omega_N\,, \\ 1+s_4^2\left(\frac{|\Omega_i|}{\omega_N}-1\right)^2 & \text{else}\,. \end{cases} \tag{2.17}$$

The Drude poles are included in the product Eq. (2.17) using their pole frequencies $\Omega = -i\gamma_d$. The parameter δ denotes the maximum frequency distance between data points. The factors s_1 and s_2 determine the strength of the repulsion of the Lorentz poles from the imaginary and real axes respectively, s_3 determines the strength of the repulsion between Lorentz poles, and s_4 determines the strength of the repulsion for absolute pole position larger than ω_N. We used $s_1 = 0.2$, $s_2 = 0.5$, $s_3 = 0.2$ and $s_4 = 0.04$ for the results shown in this work. Generally, the repulsion parameters are

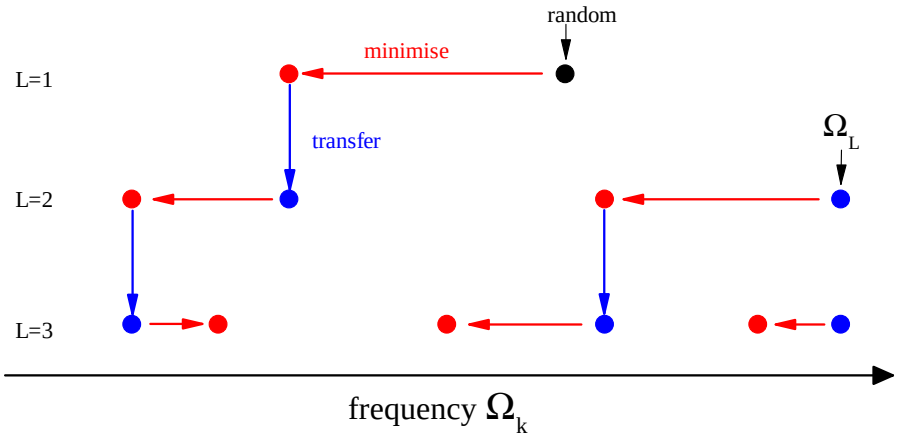

Figure 2.2: Sketch of the procedure for choosing start values for Lorentz pole frequencies Ω_k, with an increasing number of Lorentz pole pairs L.

increased from zero to suppress non-physical pole positions and to find the global minimum of $\widetilde{E}$.

To minimise $\widetilde{E}\zeta$ over the $D{+}2L$ nonlinear parameters we use known minimisation algorithms based on the gradient descent (implemented in MATLAB as function 'fminunc'). The main challenge is to select suited starting points for the parameters, from which the algorithm finds local minima. The starting points should be selected in a way that the global minimum amongst the local minima is found.

The complexity of the problem depends on the number of Drude poles D and Lorentz poles L. For $L = 0$ and $D = 1$, only a single parameter γ_1 has to be varied, which results in a reliable convergence towards the global minimum independent of the choice of its start value. Increasing D to $D + 1$, we use as starting value $\gamma_{D+1} = 2\gamma_D$.

For $L = 1$, we have an additional pair of Lorentz poles given by a single complex parameter Ω_1. For the starting value of Ω_1, we use a random logarithmic distribution within the range of the measured data, specifically

$$\Omega_1 = \omega_1 \left(\frac{\omega_N}{\omega_1}\right)^Y - i(\omega_N - \omega_1)N^{Y'-1} \tag{2.18}$$

where Y and Y' are random numbers with a uniform distribution between 0 and 1. The minimisation is repeated with different starting points until at least three resulting S values are equal within 10%, and the parameters for the lowest S are

accepted as global minimum.

The parameter space volume to be covered in such a procedure increases exponentially with L, making it computationally prohibitive to use this approach for large L. Increasing L, we therefore revert to a different strategy. Instead of guessing all Ω_k randomly, we use the optimised values for $\Omega_1, ..., \Omega_{L-1}$ of the model with $L-1$ poles as starting values for the simulation for L poles, and choose the starting value for the additional pole as $\Omega_L = [1 - i/(L+1)]\omega_N$. This procedure is sketched in Fig. 2.2. It is fast but can result in not finding the global minimum. However, we can vary the range of the experimental data to be fitted in order to provide more starting points. Here, we choose to keep the lowest frequency ω_1 fixed but vary ω_N and consequently N. Increasing or decreasing N by one, we use as starting point the optimised values for N.

Furthermore, going back, from $L+1$ to L, just removing one pair of Lorentz poles provides $L+1$ additional starting values for the simulation with L poles. It is also possible to go back multiple steps, e.g., from $L+2$ to L provides $(L+2)(L+1)/2$ starting values – this however has not been used to produce the S values in this paper.

Remaining abrupt changes of S with N can (but do not have to) indicate that the global minimum was not yet obtained, and more starting values should be employed.

2.4 Results for metals

Here we discuss examples of the DL model optimised for measured material dispersions. As previously mentioned in Sec. 1.3.1, the main example we use the data for gold by Johnson and Christy[22], which is widely used in the literature and we can compare our model with previous approaches.

The data by Johnson and Christy[22] covers the $\hbar\omega$ range from 0.64 eV to 6.6 eV, and provides n and κ with their errors as discussed in Sec. 1.3.1. Previous works[26, 30] concentrated on a narrower region 1.24 – 3.1 eV, corresponding to the extended visible light range 400 – 1000 nm. We start by using this range for the optimisation, as it is the most relevant range for applications, and also allows us to directly

compare our results with previous findings. We use $D = 1$, which is sufficient in the frequency range considered, as the photon frequency is much higher than the Drude damping, i.e., $\omega \gg \gamma$.

2.4.1 Gold

The optimised model using $L = 1$ is compared with the experimental data in Fig. 2.3(a). The refraction and absorption indices are shown as functions of the photon energy, with the measured data including error bars and lines representing the fit functions of the DL model. The poles of the model [see Eqs.(2.2) and (2.4)] are shown as circles in Fig. 2.3(b), centered at their pole positions Ω_j in the complex photon energy plane, with the complex pole weight represented by the circle area proportional to $|\sigma_j|$ and the color giving the phase. We find $S = 2.47$ for this fit, with other parameters given in Table 2.2. One can see the dominant contribution of the Drude pole having the weight about 200 times larger than the Lorentz pole. We can also see that the Lorentz pole is properly positioned to model the interband transitions of gold above 2.3 eV. The phase of σ_1 is $\pi/4$ close to the phase $\pi/2$ of a classical damped Lorentz oscillator, such as a mass on a spring. The resonance is at $\Omega_1' \sim 2.7\,\text{eV}$, around the center of the interband transition within the optimisation range, and the half-width of the resonance, $-\Omega_1'' \sim 0.7\,\text{eV}$, is approximately covering the width of the interband transitions in the same range. Comparing the model with the data in Fig. 2.3 we can see that using only a single Lorentz pole is insufficient to describe the measured data within their error, which is confirmed by the corresponding value of S above unity.

Moving to a model with two pairs of Lorentz poles, $L = 2$, the error is decreased to $S = 1.0$. The value of S below $\sqrt{2}$ indicates that this is sufficient to model the data in the optimisation range. This is also seen in Fig. 2.4, with the corresponding parameters given in Table 2.2. We show in Figs. 2.4(c) and (d) the data and the fit also for ε' and ε'', the quantities which are actually fitted, according to Eq. (2.8). Individual pole contributions to ε' and ε'' are displayed as well. The interband transitions are now described by two Lorentz poles. The first pole is at $\Omega_1' \sim 2.6\,\text{eV}$, close to the onset of the interband transition region, with a half-width of $-\Omega_1'' \sim$

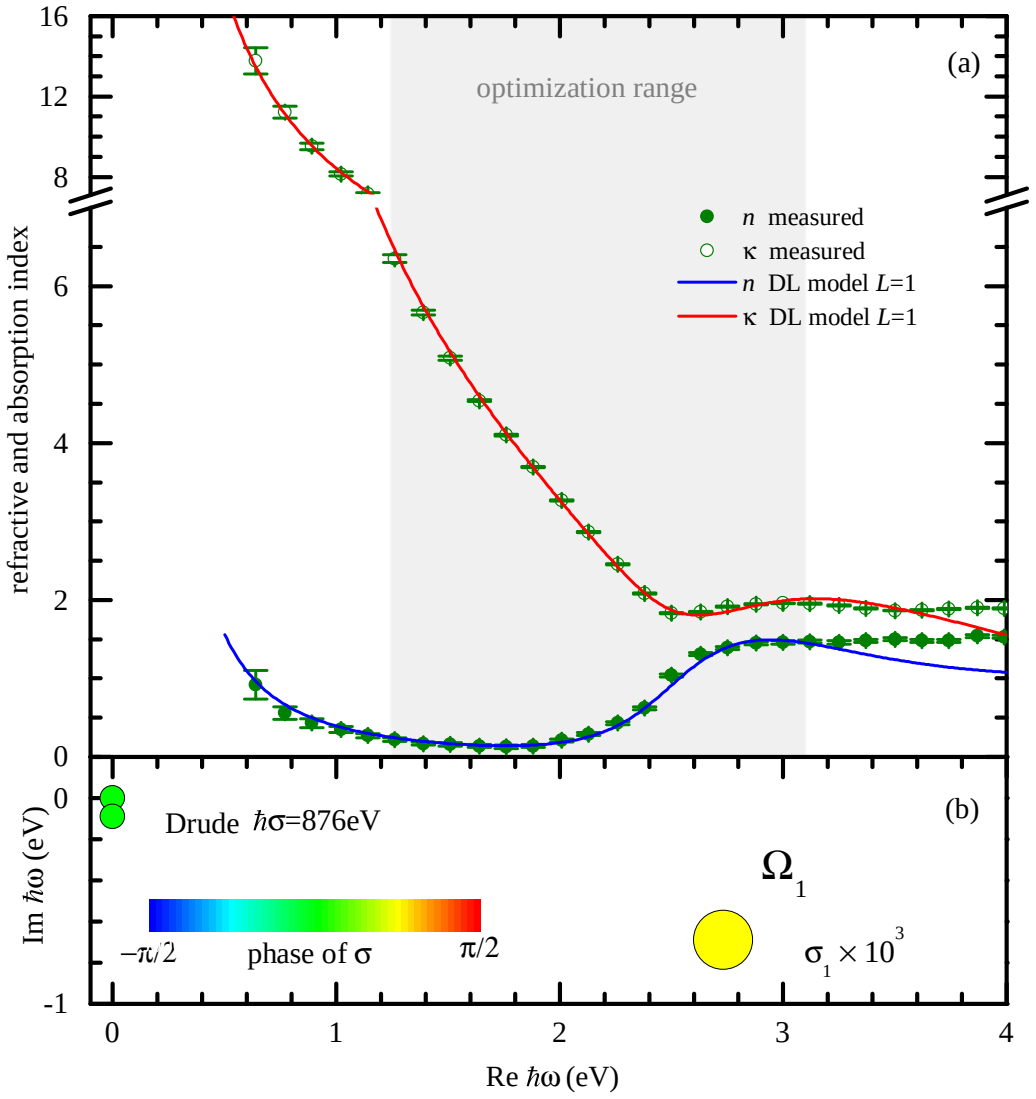

Figure 2.3: (a) Refractive index n and absorption index κ of gold according to[22] (circles and error bars) and the DL model Eq. (2.4) for $L = 1$ (solid lines) as functions of the photon energy $\hbar\omega$. The fit is optimised for the range $1.24 \leqslant \hbar\omega \leqslant 3.1\,\mathrm{eV}$. (b) Pole positions Ω_j and weights σ_j of the fitted $\varepsilon(\omega)$. The circle area is proportional to $|\sigma_j|$, and color gives the phase of σ_j as indicated. For the Lorentz poles, σ_j is multiplied by a factor of 1000 for clarity.

0.3 eV. This pole describes the edge of the interband transitions. Indeed, it has a phase close to zero, which is appropriate to describe the asymmetry of the edge, see Fig. 2.4(c). The second pole is at $\Omega_2' \sim 2.9\,\mathrm{eV}$, with a half-width of $-\Omega_2'' \sim 1.2\,\mathrm{eV}$. This pole describes the central part of the interband transition region. It has a weight about ten times higher than the first pole, and a phase close to $\pi/4$. The contribution to ε'' has accordingly a peak at around the resonance, while the contribution to ε' is more dispersive.

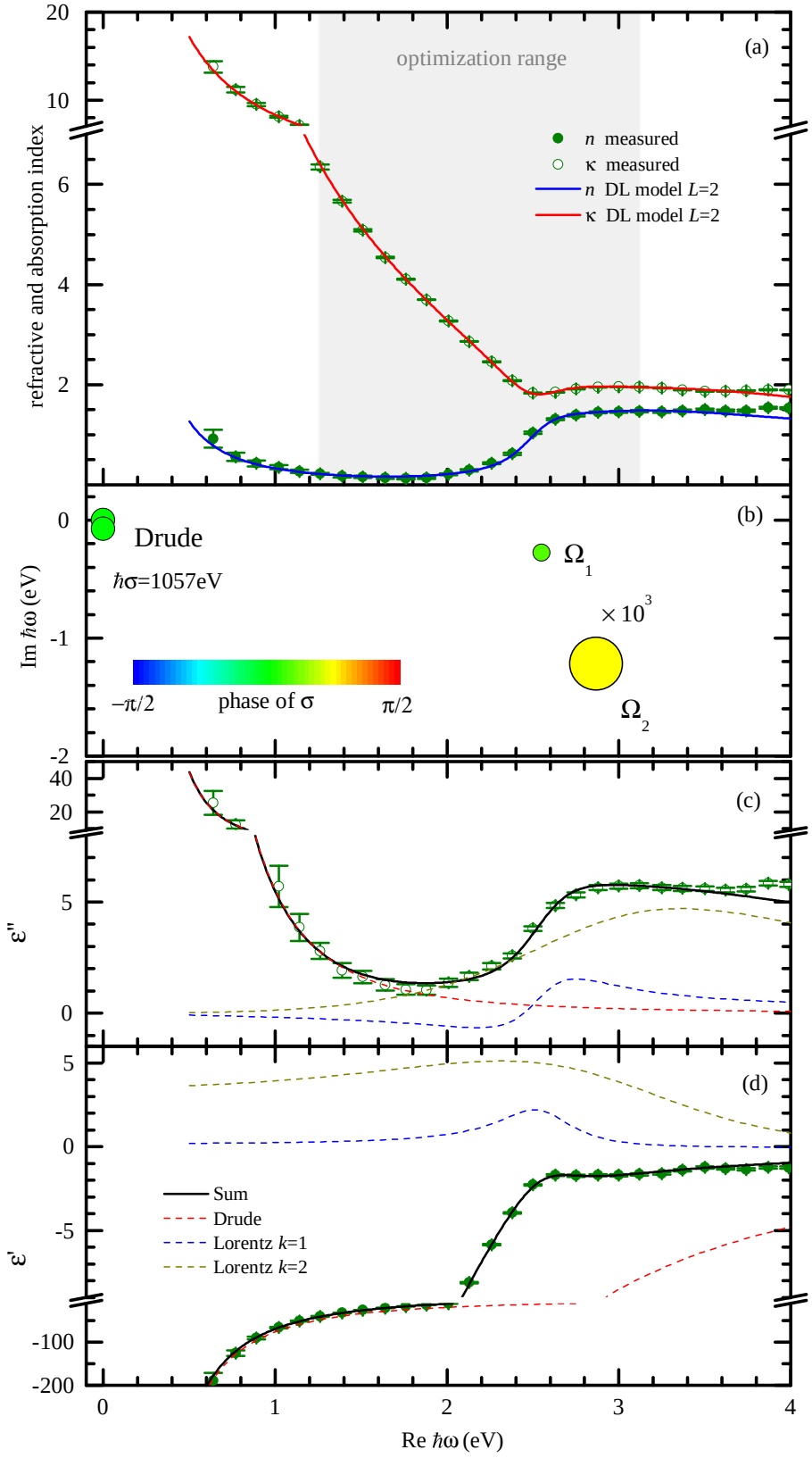

Figure 2.4: As Fig. 2.3, but for $L = 2$. Additionally, the permittivity, ε' and ε'', is shown in (c) and (d), together with the individual terms of the model Eq. (2.4).

Concerning the relation of the poles to intraband transitions in solids, it is important to emphasise that in microscopic theory the optical response is due to a large number of transitions, often described by a continuum. This continuum, however, can be represented by an infinite or a finite number of poles of the self-energy describing the effects of screening and frequency dispersion. Therefore, the model with a limited number of Lorentz oscillators presents a fully physical though approximate approach, collecting the oscillator strength and transition energies of the continuum into a finite number of poles. The resulting pole positions and weights depend on the energy range to be described and represent sets of microscopic transitions in the material.

As we have seen, we can optimise the model parameters for a given photon energy range and quantify the fit quality by the resulting value of S. Now we use a variable optimisation range, from the lowest measured photon energy to a variable upper boundary of the photon energy $\hbar\omega_N$ taking all available measured values. We show the resulting S values in Fig. 2.5(b) for different numbers of poles taken into account. We can see that with an increasing number of poles, the error S is decreasing, as expected considering the increasing number of parameters. Instead, increasing $\hbar\omega_N$ results in larger values of S, since a model of a given number of parameters is used to describe an increasing number of data.

When keeping only the $\omega = 0$ pole, corresponding to an Ohm's law dispersion, the error is always above $\sqrt{2}$. This is expected, as Ohm's law is suited only to describe the dispersion at photon energies well below the Drude damping, which is about 0.1 eV for gold. Moving to two poles, representing the Drude model, we see that the error stays below unity until $\hbar\omega_N$ approaches the interband transitions, seen in Fig. 2.5(a) as a region of increasing ε'' above 2 eV. This shows that the Drude model is well suited to describe the measured data, as long as the influence of the higher energy electronic transitions can be represented simply by a background constant ε_∞. Adding the first pair of Lorentz poles ($L = 1$), the effect of the interband transitions can be described up to about 2.6 eV, where the plateau in ε'' commences. Adding the second pair of Lorentz poles ($L = 2$), the effect of the interband transitions can be described up to about 4.9 eV, where ε'' starts to decrease. Adding the third pair

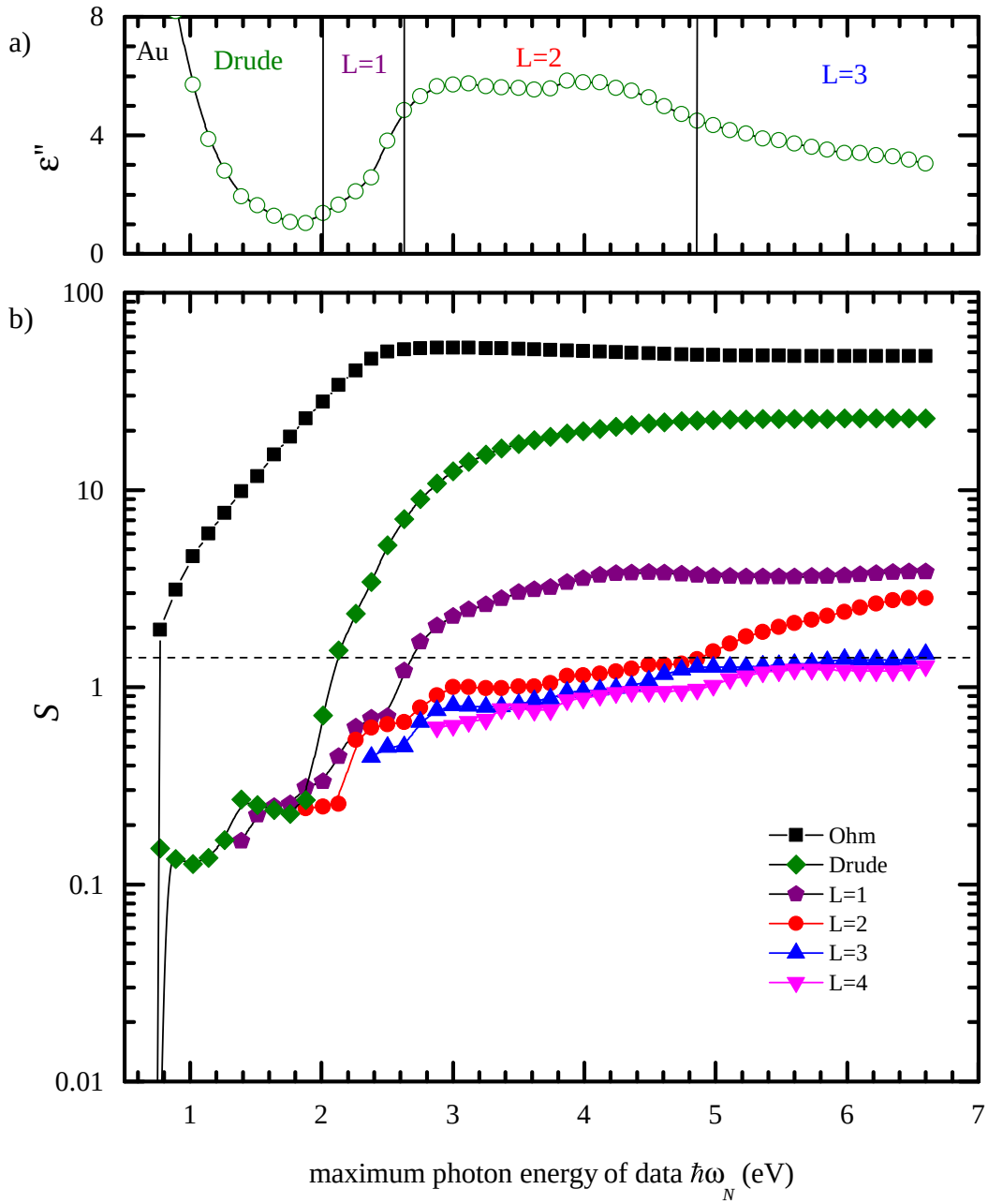

Figure 2.5: (a) ε_j'' as function of $\hbar\omega_j$. (b) Error S as function of the upper photon energy limit of the fitted data range for Au data taken from [22]. Results for various number of poles in the model are given. Lines are guides for the eye. The maximum photon energy ranges suited for the different number of poles are indicated in (a) by vertical lines.

of Lorentz poles ($L = 3$) allows us to adequately describe the full range of measured data up to 6.5 eV.

Figure 2.6 shows the error S for $L = 2$ and $L = 3$, and both lower and higher limits of the fitted range changing. Including more data points results in higher

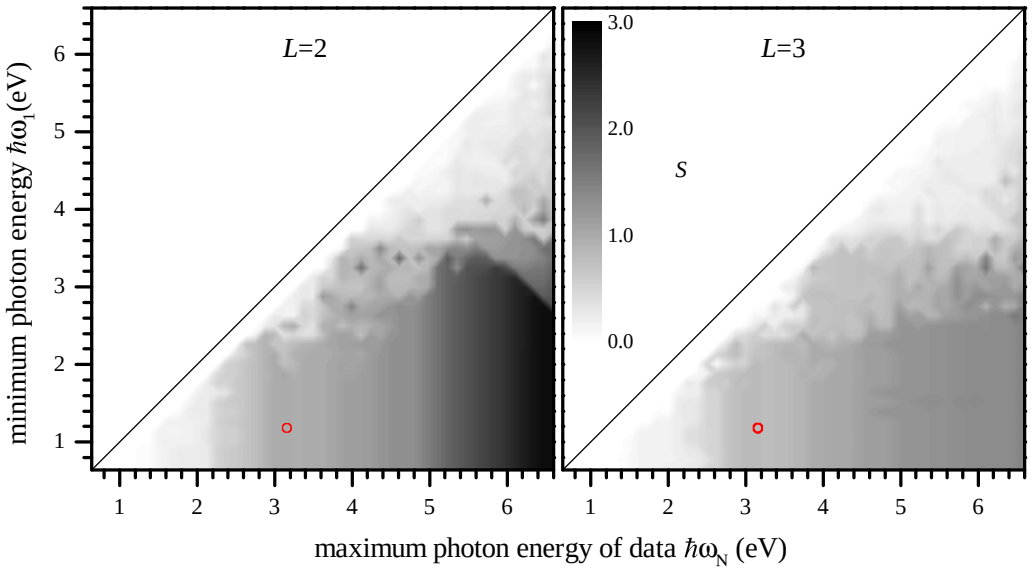

Figure 2.6: Error S for $L = 2$ and $L = 3$ on a gray scale as given as a function of both the lower and upper photon energy limits of the fitted data range for the Au data in [22]. The circle indicates the range $1.24 \leqslant \hbar\omega \leqslant 3.1\,\text{eV}$ used in [26].

errors, as seen by the gradient of S towards the lower right corner. We can see that any range of the available data can be described by the DL model with $L = 3$ with errors $S < \sqrt{2}$. The region of interest used in previous works[26, 30], $1.24 \leqslant \hbar\omega \leqslant 3.1\,\text{eV}$, is also indicated by red circles. Using the parameters of [26], corresponding to the model with $L = 2$, we find $S = 1.96$, which is larger than the value $S = 1$ we found (see Table 2.2). This can be attributed to the fact that in [26] the absolute error of ε was minimised, not taking into account the experimental errors. Such a minimisation corresponds in our case to setting $\Delta\varepsilon' = \Delta\varepsilon'' = 1$ for all data points. Using these errors, both in the definition of S and in the optimisation of the parameters, we find $S = 0.019$ for $L = 2$, while using the parameters of [26] results in $S = 0.028$. This confirms the high quality of our optimisation method.

The model with $L = 3$ optimised for the full data range is compared with the measured data in Fig. 2.7. The fitted parameters are given in Table 2.2. We see that the first two Lorentz poles are similar to those in the $L = 2$ model used for the limited range and shown in Fig. 2.4. To describe the full range, an additional pole at higher energy, having $\Omega_3' \sim 7.3\,\text{eV}$ and a half-width of $-\Omega_3'' \sim 21.8\,\text{eV}$, is needed. This pole describes the continuum of interband transitions, and takes over

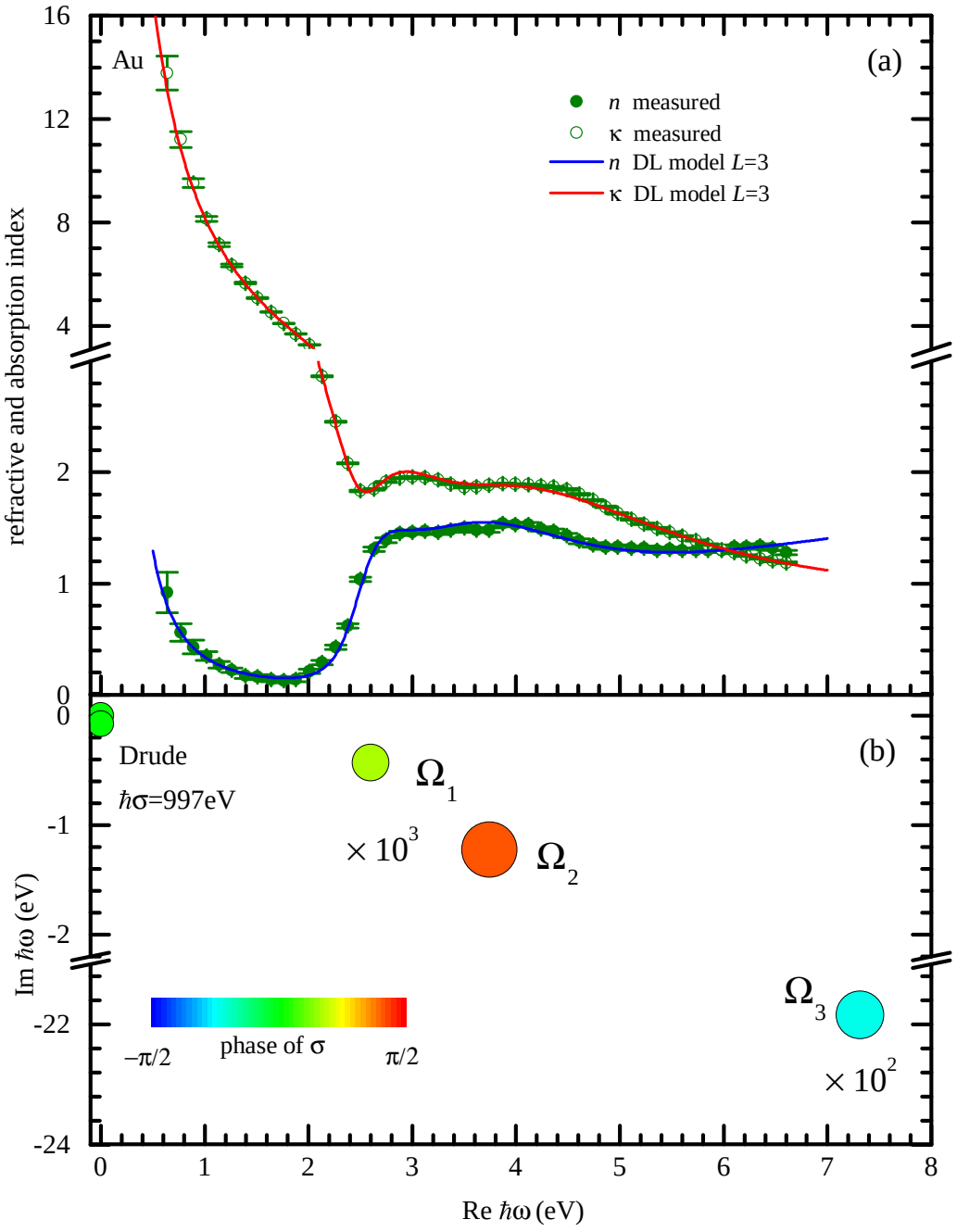

Figure 2.7: As Fig. 2.3, but for $L = 3$ and optimised for the full data range of $\hbar\omega$ given in [22], from 0.64 eV to 6.6 eV.

the role of ε_∞, which in this fit has a value below $\sqrt{2}$. The weight of the pole is about ten times higher than for the second pole, and the phase is close to $-\pi/4$. Fixing $\varepsilon_\infty = 1$, which is well suited for FDTD methods, the main difference (see Table 2.2) is a change in the high energy third pole.

L	1	2	3	3
ε_∞	3.9199	2.6585	−10.534	1
γ(eV)	0.0893	0.07247	0.07373	0.074018
σ(eV)	875.79	1056.9	997.41	995.13
Ω_1'(eV)	2.7326	2.5509	2.5997	2.6039
Ω_1''(eV)	−0.69021	−0.27427	−0.43057	−0.42417
σ_1'(eV)	3.0701	0.57604	1.4835	1.4145
σ_1''(eV)	2.9306	0.18443	0.88382	0.89754
Ω_2'(eV)	–	2.8685	3.7429	3.685
Ω_2''(eV)	–	−1.2195	−1.2267	−1.2475
σ_2'(eV)	–	4.1891	1.1372	1.5109
σ_2''(eV)	–	4.2426	3.8223	3.9555
Ω_3'(eV)	–	–	7.3145	17.087
Ω_3''(eV)	–	–	−21.843	−0.41705
σ_3'(eV)	–	–	225.27	−30.678
σ_3''(eV)	–	–	−193.27	13.987
$\hbar\omega_1$(eV)	1.24	1.24	0.64	0.64
$\hbar\omega_N$(eV)	3.1	3.1	6.6	6.6
$2N$	30	30	98	98
Fit parameters	7	11	15	14
S	2.4735	1.0029	1.4747	1.4872

Table 2.2: Optimised model parameters for different number of Lorentz pole pairs L and optimisation energy ranges corresponding to the data shown in Figs. 2.3, 2.4, and 2.7. The number of data values $2N$, the number of fit parameters, and the resulting error S are also given. The last column shows an example where we choose $\varepsilon_\infty = 1$.

2.4.1.1 Single-crystalline gold

In Fig. 2.8 we show results for gold using the newer experimental data from [32]. This data does not provide the experimental error. We therefore have chosen here to minimise the relative error instead, using $\Delta\varepsilon = \varepsilon$ in Eq. (2.8). We see a similar behavior as for the data from [22], see Fig. 2.5.

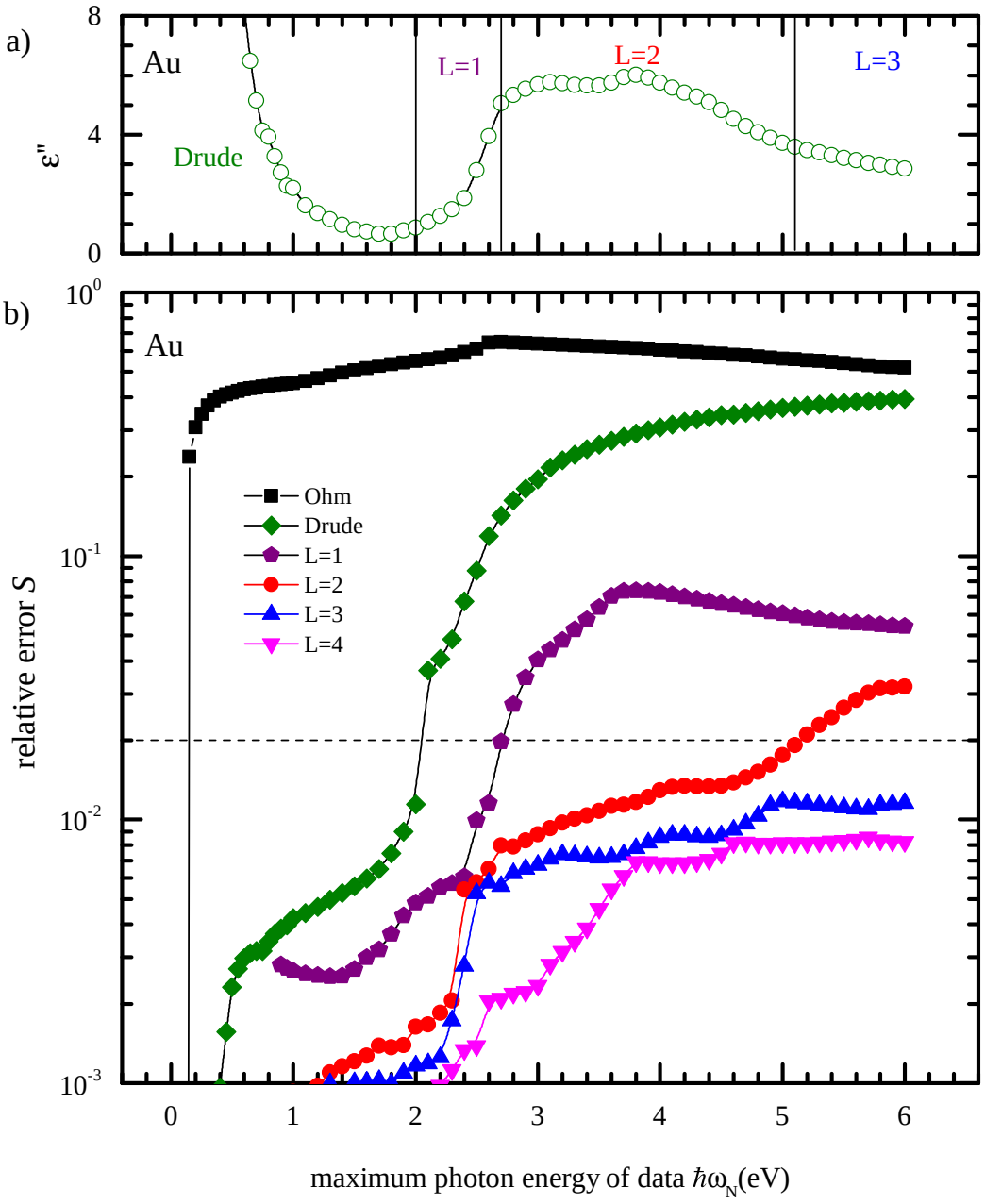

Figure 2.8: As Fig. 2.5, but for gold using data from [32]. We show a dashed line at 2% relative error as a guide to a satisfactory fit.

2.4.2 Silver and copper

Here we show the results of the fit of the DL model for silver. As in Fig. 2.5 of the main text, we use a variable upper limit $\hbar\omega_N$ of the optimisation range and show the resulting S values for different numbers of poles. In Fig. 2.9 we show results for silver using the data from [22], having the lower photon energy limit at $\hbar\omega_1 = 0.64\,\text{eV}$. Ag has interband transitions above 4 eV. We find that the Drude model is sufficient up

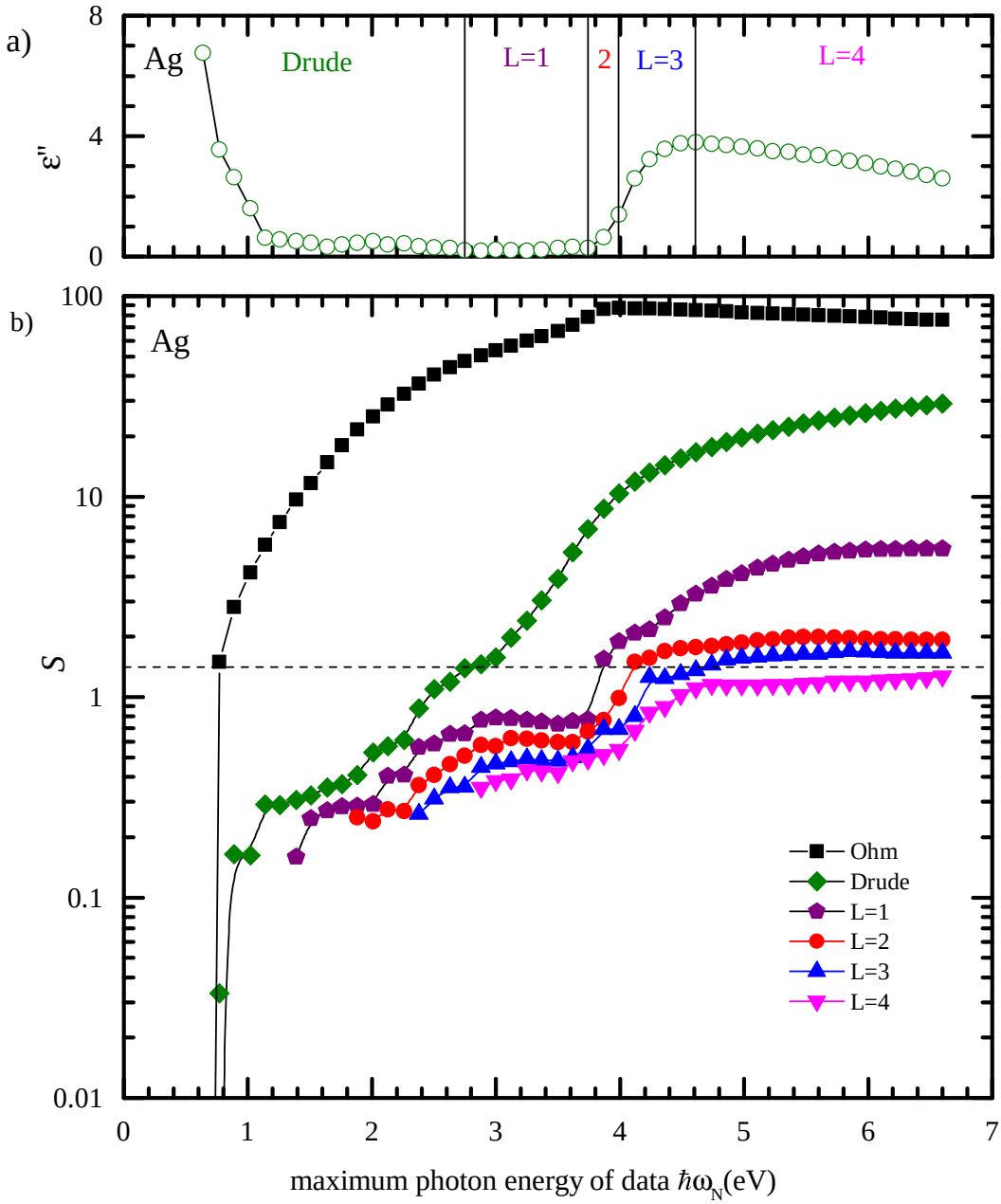

Figure 2.9: As Fig. 2.5, but for silver.

to photon energies of 2.4 eV, one additional pair of Lorentz oscillators up to 3.7 eV, two up to 4.0 eV, three up to 4.7 eV, and four up to a value above the upper limit of 6.6 eV.

In Fig. 2.10 we show results for copper using the data from [22], having the lower photon energy limit at $\hbar\omega_1 = 0.64$ eV. Cu has interband transitions above 2 eV. We find that the Drude model is sufficient up to photon energies of 1.9 eV, one additional pair of Lorentz oscillators up to 2.2 eV, two up to 4.7 eV and three up to 6 eV.

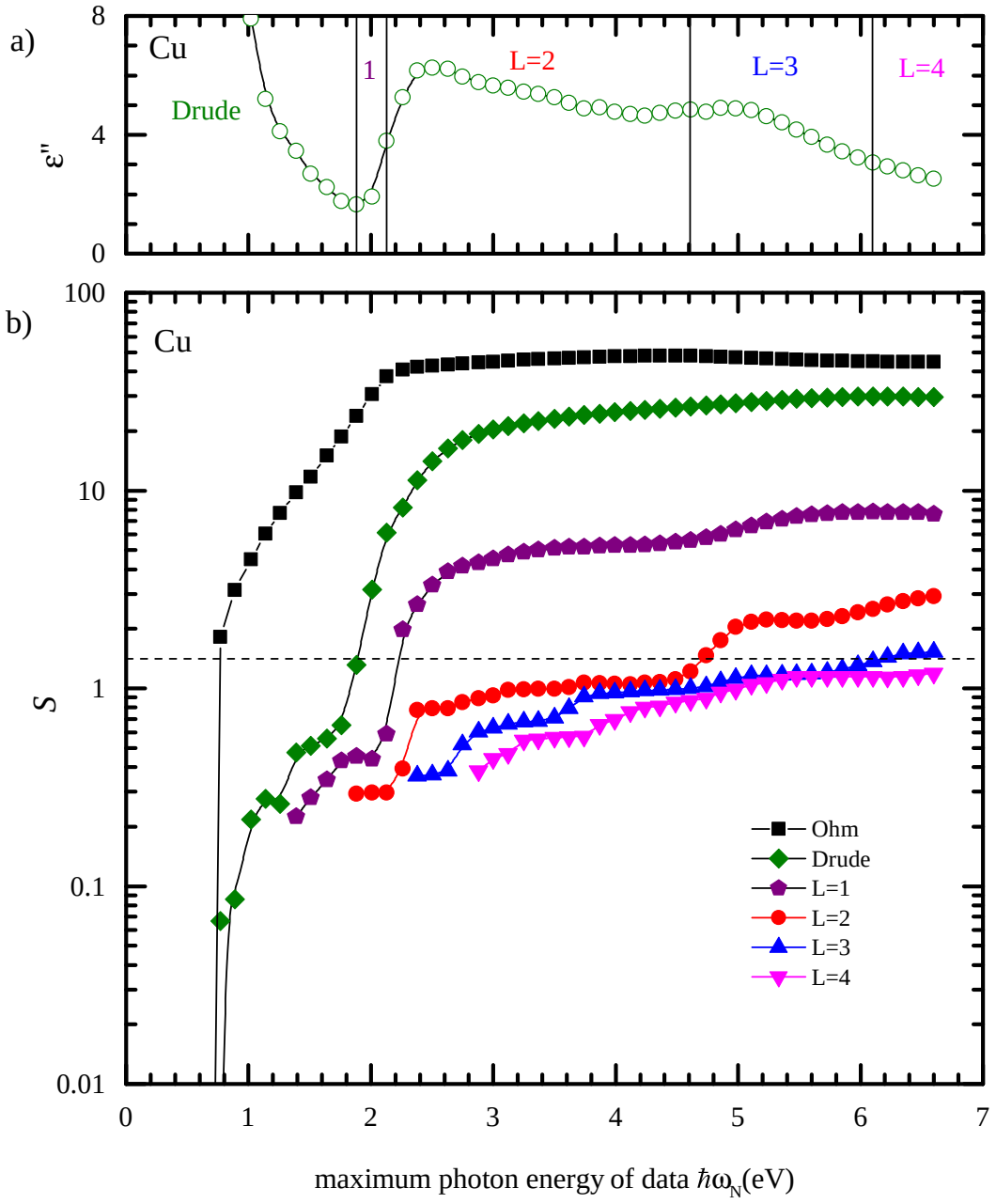

Figure 2.10: As Fig. 2.5, but for copper.

The parameters fitted for the full spectral range shown in Figs. 2.9, 2.10, and 2.8, with $L = 3$ and 4, are given in Table 2.3.

Material	Ag	Cu	Au	Au
L	4	4	3	4
ε_∞	0.77259	12.294	1.1584	0.83409
γ(eV)	0.02228	0.07044	0.02321	0.02334
σ(eV)	3751.4	1137.9	3155.3	3134.5
Ω_1'(eV)	3.9173	2.1508	2.1339	2.6905
Ω_1''(eV)	−0.06084	−0.23449	−3.4028	−0.16645
σ_1'(eV)	0.09267	0.95283	12.0	−0.01743
σ_1''(eV)	0.01042	−0.12983	−5.5574	0.3059
Ω_2'(eV)	3.988	4.6366	2.6319	2.8772
Ω_2''(eV)	−0.04605	−0.68811	−0.33701	−0.44473
σ_2'(eV)	−0.0015342	0.97953	1.0547	1.0349
σ_2''(eV)	−0.062233	0.48395	0.53584	1.2919
Ω_3'(eV)	4.0746	4.9297	4.0803	3.7911
Ω_3''(eV)	−0.63141	−4.6932	−0.99872	−0.81981
σ_3'(eV)	1.4911	−61.583	−1.3103	1.2274
σ_3''(eV)	0.40655	35.021	2.7819	2.5605
Ω_4'(eV)	4.6198	8.8317	–	4.8532
Ω_4''(eV)	−2.8279	−0.2679	–	−13.891
σ_4'(eV)	4.2843	−12.186	–	9.85
σ_4''(eV)	4.2181	5.1474	–	37.614
$\hbar\omega_1$(eV)	0.64	0.64	0.1	0.1
$\hbar\omega_N$(eV)	6.6	6.6	6.0	6.0
N	49	49	69	69
S	1.2684	1.0956	0.01151	0.00826

Table 2.3: As Table 2.2, but for the data[22] for Ag and Cu and for the data[32] for Au, corresponding to the full fit range shown in Figs. 2.9, 2.10, and 2.8, respectively.

2.5 Results for semiconductors

In this section we will describe semiconductors which have a negligible free carrier density, and thus a negligible Drude pole weight. Their susceptibility in the visible and ultraviolet range is dominated by interband transitions. We thus use a version of $\varepsilon(\omega)$ which contains only pairs of Lorentz poles,

$$\varepsilon(\omega) = \varepsilon_\infty + \sum_{k=1}^{L} \left(\frac{i\sigma_k}{\omega - \Omega_k} + \frac{i\sigma_k^*}{\omega + \Omega_k^*} \right) , \tag{2.19}$$

where L is the number of such pairs. Both the pole positions $\Omega_k = \Omega_k' + i\Omega_k''$ and generalised conductivities $\sigma_k = \sigma_k' + i\sigma_k''$ are complex.

As before, the model of the permittivity $\varepsilon(\omega)$ given by the analytic function Eq. (2.19) with $\Omega_k'' \leqslant 0$ respects the constrain of causality by construction. The parameters of the model, which are the conductivities and the resonance frequencies, have to be determined from the experimentally measured data.

Here we discuss examples of the Lorentz model optimised for measured material dispersions. We show results for crystals of silicon (Si), gallium arsenide (GaAs) and germanium (Ge) where the data is from[33]. As semiconductors do not have a significant free carrier density, they do not require a Drude pole, so we have fitted the experimental permittivity with the background term (ε_∞) and up to five pairs of Lorentz poles. We use a variable optimisation range, from the lowest measured photon energy $\hbar\omega_1$ to a variable upper boundary of the photon energy $\hbar\omega_N$ taking all available measured values. We show the resulting S values for Si in Fig. 2.11(b) for different numbers of poles taken into account. We can see that with an increasing number of poles, the error is decreasing, as expected considering the increasing number of parameters. Also, increasing $\hbar\omega_N$ results in larger S values, since a model of a given number of parameters is used to describe an increasing number of data.

As we have no experimental errors for the permittivity we use in this work $\Delta\varepsilon_j = \varepsilon_j$, which means that the S values we use are the normalised relative error. We show a dashed line in Fig. 2.11(b) at 2% relative error as a guide to a satisfactory fit.

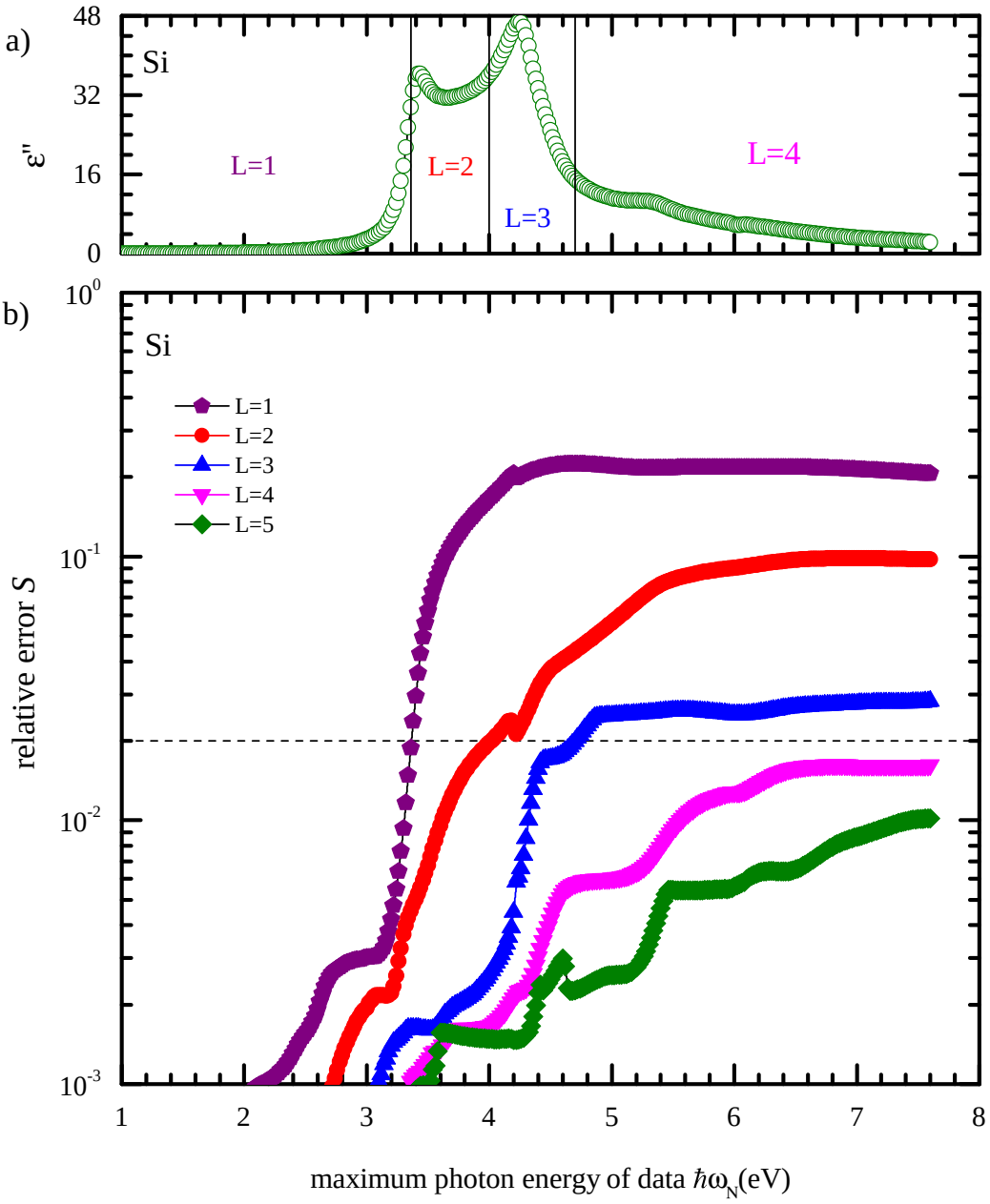

Figure 2.11: (a) ε_j'' as function of $\hbar\omega_j$ for Si. (b) Error S as function of the upper photon energy limit of the fitted data range for Si[33]. Results for various number of poles in the model are given. Lines are guides for the eye. The maximum photon energy ranges suited for the different number of poles are indicated in (a) by vertical lines.

For Si, adding the first pair of Lorentz poles ($L = 1$) we see the effect of the interband transitions can be described up to the first peak in ε'', around 3.4 eV. Adding the second pair of Lorentz poles ($L = 2$), the effect of the interband transitions can be described up to about 4 eV, as $\hbar\omega_N$ approaches another peak in ε''. Three pairs ($L = 3$) describe both peaks in ε'' up to 4.7 eV and finally four pairs of Lorentz poles

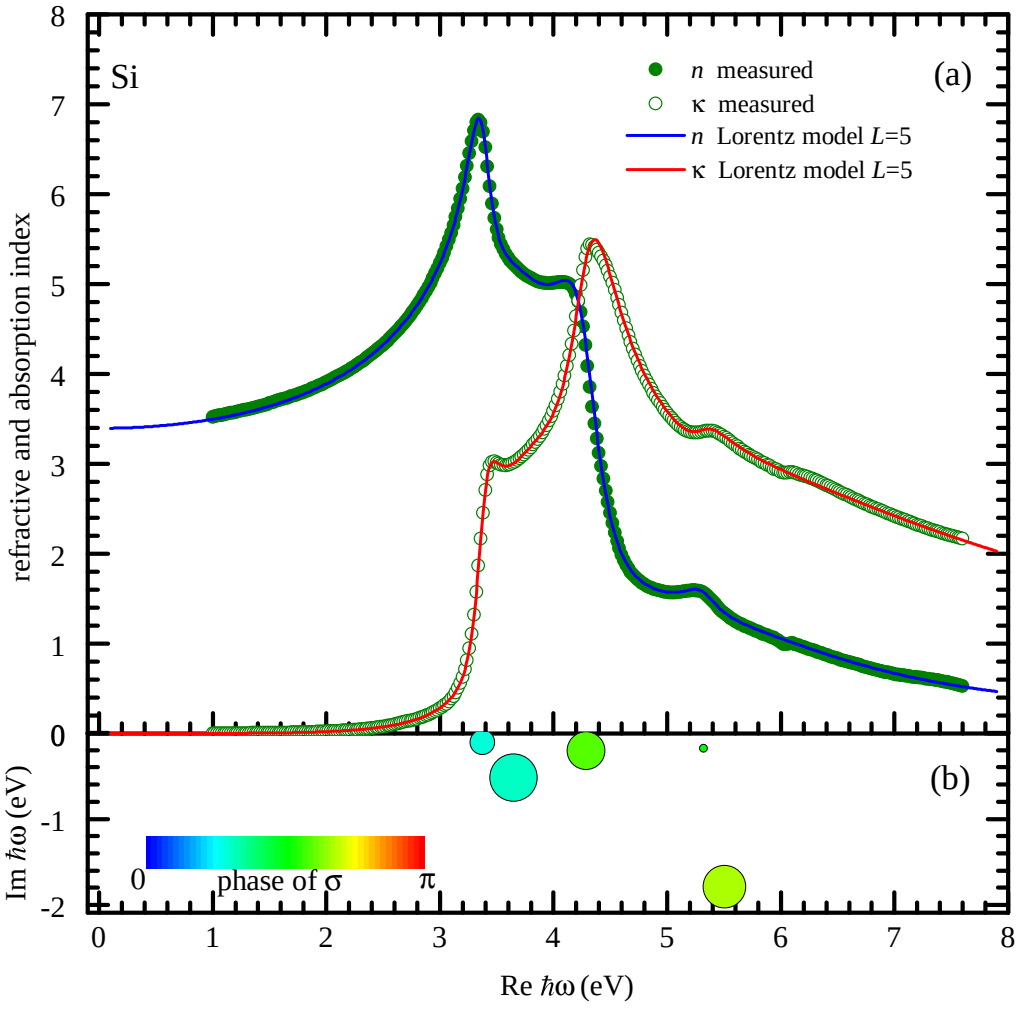

Figure 2.12: (a) Refractive index n and absorption index κ of Si according to[33] and the Lorentz model Eq. (2.19) for $L = 5$ (solid lines) as functions of the photon energy $\hbar\omega$. The fit is optimised for the full range $1.0 \leqslant \hbar\omega \leqslant 7.6\,\mathrm{eV}$ of available data. (b) Pole positions Ω_j (center of the circle) and weights σ_j of the fitted $\varepsilon(\omega)$. The circle area is proportional to $\sqrt{|\sigma_j|}$, and color gives the phase of σ_j as indicated.

adequately describes the full range of measured data up to 7.6 eV, with $S = 0.0162$. We do see a significant improvement in S when going to five pairs of poles.

The optimised model for Si with $L = 5$ is compared with the experimental data in Fig. 2.12(a). The refraction and absorption indices are shown as a function of the photon energy, with the measured data as circles and lines representing the fit functions of the Lorentz model. The poles of the model [see Eq.(2.19)] are shown as circles in Fig. 2.12(b), centered at their pole positions Ω_j in the complex photon energy plane, with the complex pole weight represented by the circle area propor-

tional to $\sqrt{|\sigma_j|}$ and the color giving the phase. We find $S = 0.0102$ for this fit, with other parameters given in Table 2.2. We can see that the Lorentz pole is properly positioned to model the interband transitions of silicon. The phases of all 5 poles are close to $\pi/2$, corresponding to a classical damped Lorentz oscillator, such as a mass on a spring or a pendulum. The resonances $\Omega_1' \sim 3.4\,\text{eV}$ and $\Omega_3' \sim 4.3\,\text{eV}$ are around the centers of the two interband transitions well seen in Fig1.(a) within the optimisation range, and the half-width of the resonances, $-\Omega_1'' \sim 0.1\,\text{eV}$ and $-\Omega_3'' \sim 0.2\,\text{eV}$, are approximately covering the half-width of these transitions.

We obtained similar results for GaAs and Ge, shown in Sec. B, which can be seen in Fig. B.1 and Fig. B.3. As in Fig. 2.11, we use a variable upper limit $\hbar\omega_N$ of the optimisation range and show the resulting S values for different numbers of poles. For GaAs we find that the model with one pair of Lorentz oscillators works well up to 1.6 eV, two up to 2.9 eV, three up to 4.6 eV, four up to 5 eV, and five up to a value above the upper limit of 6 eV. For Ge we find that the one pair of Lorentz oscillators is a good approximation up to 1.1 eV, two up to 2.2 eV, three up to 4.2 eV, four up to 5.6 eV, and five beyond the upper limit of 6 eV.

In Fig. B.2, the first Lorentz pole conductivity σ_1 is multiplied by a factor of 10 for clarity. We find phases of all poles close to $\pi/2$, corresponding to a classical damped Lorentz oscillator. There are similar results for Ge which can be seen in Fig. B.4, most poles having a phase close to $\pi/2$ with the exception of the first pole which has a phase very close to zero. We note that the indirect band gap of both Si and Ge is less suited for the modeling by simple poles, due to the phonon-assisted absorption leading to a weak tail in the absorption spectrum. We can see this clearly in the absorption index for $\hbar\omega < 1\,\text{eV}$, shown in Fig. B.4(a).

All parameters and values of S for the fits shown in Fig. 2.12, Fig. B.2 and Fig. B.4 can be found in Table 2.4.

2.6 Summary

In this chapter we discuss the advantages of using the Drude-Lorentz model for $\hat{\varepsilon}(\omega)$ due to the simple pole structure and the physical arguments such as the presence of resonances. This links back with the GF, explained in Sec. 1.2, which provides the complete system response and allows for the calculation of observables such as emission, scattering, or transmission. The pole structure is what leads to describing the permittivity of materials simply and accurately and further allows for the description of material properties through the GF.

With this analytic model, we can fit the experimental data by finding the parameters of the model which minimise the error weighted deviation between the analytic and the measured values. We use an exact minimisation of the linear parameters and a gradient decent method for the non-linear parameters. This gives us a more accurate fit across a larger range of data. We provide an efficient algorithm of fitting the data using an arbitrary number of Lorentz poles. We illustrate the resulting pole positions and their weights in the complex plane to give some physical insight how the model approximates the electronic transitions in real materials. This has been shown for metals, which require the Drude pole due to the high free electron density, and also for semiconductors, which we model using Lorentz poles only. In principle we can use this method to fit the frequency-dependent permittivity of any material.

Material	Si	GaAs	Ge
ε_∞	0.81568	−0.54651	0.79842
Ω_1'(eV)	3.3736	1.4377	1.168
Ω_1''(eV)	−0.11402	−0.05948	−0.33778
σ_1'(eV)	1.6934	0.01981	0.47159
σ_1''(eV)	2.084	0.01122	0.01002
Ω_2'(eV)	3.6519	2.7229	2.174
Ω_2''(eV)	−0.52378	−1.2972	−0.28077
σ_2'(eV)	5.2573	7.8336	3.2926
σ_2''(eV)	8.0106	8.3274	4.1239
Ω_3'(eV)	4.2877	2.8922	3.781
Ω_3''(eV)	−0.21116	−0.23992	−1.1461
σ_3'(eV)	−1.7164	2.706	0.86584
σ_3''(eV)	5.9939	1.616	18.898
Ω_4'(eV)	5.3188	4.5222	4.3232
Ω_4''(eV)	−0.18434	−0.42072	−0.20006
σ_4'(eV)	−0.00528	2.1137	−1.7377
σ_4''(eV)	0.32911	4.6445	2.5278
Ω_5'(eV)	5.5064	4.9278	5.6442
Ω_5''(eV)	−1.7892	−0.19972	−0.41214
σ_5'(eV)	−3.8438	−1.243	0.10451
σ_5''(eV)	6.9298	1.4424	1.0292
$\hbar\omega_1$(eV)	1.0	1.3	0.5
$\hbar\omega_N$(eV)	7.6	6.0	6.0
$2N$	662	190	222
$1+4L$	21	21	21
S	0.01016	0.01157	0.01327

Table 2.4: Optimised model parameters for different semiconductors, using the fit function with five pairs Lorentz pole and optimisation energy ranges corresponding to the data shown in Figs. 2.12, B.2, and B.4. The number of data values $2N$, the number of fit parameters $1+4L$, and the resulting error S are also given.

Chapter 3

Dispersive RSE

3.1 Formulism of dispersive RSE

So far the RSE has been applied to non-dispersive one-, two- and three-dimensional systems [4, 5, 13, 14]. Using non-dispersive permittivities is insufficient for realistic systems which always show a frequency dispersion of the refractive index, including dielectric materials such as glass. A previous paper [34] describes how we modify the RSE for such materials with dispersion, we discuss the method here. As previously discussed in Sec. 2.2, we can use the Drude-Lorentz model to fit the measured permittivity.

Quite generally, the permittivity $\hat{\boldsymbol{\varepsilon}}(\mathbf{r}, \omega)$ can be treated as an analytic function in the complex frequency plane, having a countable number of simple poles, see Eq. (2.1). Here we use both $k = \omega/c$ and ω for brevity of notations. We use a model which consists of an arbitrary number of poles given by

$$\hat{\boldsymbol{\varepsilon}}(\mathbf{r}, \omega) = \hat{\boldsymbol{\varepsilon}}_\infty(\mathbf{r}) + \sum_j \frac{i\hat{\boldsymbol{\sigma}}_j(\mathbf{r})}{\omega - \Omega_j}\,, \tag{3.1}$$

where ε_∞ is the permittivity at high frequencies and the generalised conductivities $\hat{\boldsymbol{\sigma}}_j(\mathbf{r})$ are complex. Eq. (3.1) is a generalisation of Eq. (2.1) with tensor weights for the poles enabling to describe anisotropic media.

We start with the dispersive basis of RSs which are the eigen solutions of the Maxwell wave equation Eq. (1.4), in which $\hat{\boldsymbol{\varepsilon}}(\mathbf{r}, \omega)$ is Eq. (3.1), with the outgoing

wave boundary conditions [13]. The GF of Maxwell's wave equation has the spectral representation [4, 13, 14] shown in Sec. 1.2,

$$\hat{\mathbf{G}}_k(\mathbf{r},\mathbf{r}') = \sum_n \frac{\mathbf{E}_n(\mathbf{r}) \otimes \mathbf{E}_n(\mathbf{r}')}{2k(k-k_n)}\,, \tag{3.2}$$

where the sum is taken over all RSs. We substitute Eq. (3.2) into Maxwell's equation Eq. (1.4) with a delta-function source term in the form of

$$-\nabla\times\nabla\times\hat{\mathbf{G}}_k(\mathbf{r},\mathbf{r}') + k^2\,\hat{\boldsymbol{\varepsilon}}(\mathbf{r},\omega)\hat{\mathbf{G}}_k(\mathbf{r},\mathbf{r}') = \hat{\mathbf{1}}\delta(\mathbf{r}-\mathbf{r}') \tag{3.3}$$

and using Eq. (1.4) and Eq. (3.3) we can obtain the closure relation [5]

$$\sum_n \frac{k^2\hat{\boldsymbol{\varepsilon}}(\mathbf{r},\omega) - k_n^2\hat{\boldsymbol{\varepsilon}}(\mathbf{r},\omega_n)}{2k_n(k-k_n)}\,\mathbf{E}_n(\mathbf{r})\otimes\mathbf{E}_n(\mathbf{r}') = \hat{\mathbf{1}}\delta(\mathbf{r}-\mathbf{r}')\,. \tag{3.4}$$

Given a single Lorentz pole of the form $\sigma/(\omega-\Omega)$ we can write Eq. (3.4) as

$$\frac{\sigma}{2\omega_n(\omega-\omega_n)}\left(\frac{\omega^2}{\omega-\Omega_j} - \frac{\omega_n^2}{\omega_n-\Omega_j}\right) = \frac{\sigma}{2(\omega_n-\Omega_j)} + \frac{\sigma\omega}{2(\omega-\Omega_j)}\left(\frac{1}{\omega_n} - \frac{1}{\omega_n-\Omega_j}\right), \tag{3.5}$$

with the constant term $\hat{\boldsymbol{\varepsilon}}_\infty(\mathbf{r})$ written as

$$\frac{k^2\hat{\boldsymbol{\varepsilon}}_\infty(\mathbf{r}) - k_n^2\hat{\boldsymbol{\varepsilon}}_\infty(\mathbf{r})}{2k_n(k-k_n)} = k\frac{\hat{\boldsymbol{\varepsilon}}_\infty(\mathbf{r})}{2k_n} + \frac{\hat{\boldsymbol{\varepsilon}}_\infty(\mathbf{r})}{2}\,. \tag{3.6}$$

We use Eq. (3.5) and Eq. (3.10) in Eq. (3.4) to give us another closure relation

$$\sum_n \frac{\hat{\boldsymbol{\varepsilon}}(\mathbf{r},\omega)}{2}\,\mathbf{E}_n(\mathbf{r})\otimes\mathbf{E}_n(\mathbf{r}') = \hat{\mathbf{1}}\delta(\mathbf{r}-\mathbf{r}') \tag{3.7}$$

and *sum rules*

$$\hat{\boldsymbol{\varepsilon}}_\infty(\mathbf{r})\sum_n \frac{\mathbf{E}_n(\mathbf{r})\otimes\mathbf{E}_n(\mathbf{r}')}{\omega_n} = 0 \tag{3.8}$$

and

$$\hat{\boldsymbol{\sigma}}_j(\mathbf{r})\sum_n \frac{\mathbf{E}_n(\mathbf{r})\otimes\mathbf{E}_n(\mathbf{r}')}{\omega_n-\Omega_j} = 0\,. \tag{3.9}$$

The latter holds for every Ω_j contributing to the permittivity given by Eq. (3.1).

Eq. (3.8) and Eq. (3.9) are used to modify GF Eq. (3.2) along with appropriate algebraic identities. Using the algebraic identity

$$\frac{1}{\omega_n(\omega-\omega_n)}-\frac{1}{2\omega\omega_n}=\frac{1}{2\omega(\omega-\omega_n)} \tag{3.10}$$

for the non-dispersive part, we obtain

$$\hat{\mathbf{G}}_k^0(\mathbf{r},\mathbf{r}')=\sum_n\frac{\mathbf{E}_n(\mathbf{r})\otimes\mathbf{E}_n(\mathbf{r}')}{2k_n(k-k_n)}-\frac{1}{2k}\sum_n\frac{\mathbf{E}_n(\mathbf{r})\otimes\mathbf{E}_n(\mathbf{r}')}{k_n}\,, \tag{3.11}$$

and using the identity

$$\frac{1}{\omega(2\omega-\omega_n)}+\frac{\Omega}{2\omega^2(\omega_n-\Omega)}=\frac{\omega_n(\omega-\Omega)}{2\omega^2(\omega_n-\Omega)(\omega-\omega_n)} \tag{3.12}$$

for the dispersive part we obtain

$$\hat{\mathbf{G}}_k^j(\mathbf{r},\mathbf{r}')=\hat{\mathbf{G}}_k^0(\mathbf{r},\mathbf{r}')+\frac{\Omega_j}{2k^2}\sum_n\frac{\mathbf{E}_n(\mathbf{r})\otimes\mathbf{E}_n(\mathbf{r}')}{\omega_n-\Omega_j}\,. \tag{3.13}$$

Along with the new forms of the GF, $\hat{\mathbf{G}}_k^0(\mathbf{r},\mathbf{r}')$ and $\hat{\mathbf{G}}_k^j(\mathbf{r},\mathbf{r}')$, we introduce

$$F_n^0(\omega)=\frac{1}{2k}\qquad\qquad F_n^j(k)=\frac{k_n}{2k^2}\,\frac{\omega-\Omega_j}{\omega_n-\Omega_j}\,, \tag{3.14}$$

to rewrite the GF as

$$\hat{\mathbf{G}}_k(\mathbf{r},\mathbf{r}')=\hat{\mathbf{G}}_k^j(\mathbf{r},\mathbf{r}')=\sum_n F_n^j(k)\frac{\mathbf{E}_n(\mathbf{r})\otimes\mathbf{E}_n(\mathbf{r}')}{k(k-k_n)}\,. \tag{3.15}$$

Eq. (3.15) is an *additional spectral representation* $\hat{\mathbf{G}}_k^j$ of the GF for each pole in the permittivity. Note that the Ohm's law dispersion introduces a $\omega=0$ pole in the permittivity which leads to the sum rule Eq. (3.9) with $\Omega_0=0$, identical to Eq. (3.8). The $\omega=0$ pole is actually present also in the non-dispersive system owing to the longitudinal $\omega_n=0$ modes [5], see Sec. 3.2. As a result, the sum rule Eq. (3.8) [or Eq. (3.9) with $\Omega_0=0$] holds even without dispersion[13, 14], due to the constant term $\hat{\boldsymbol{\varepsilon}}_\infty(\mathbf{r})$ which, physically, is the permittivity at high frequencies.

Let us now consider a perturbed system, in which $\hat{\boldsymbol{\varepsilon}}(\mathbf{r},\omega)$ is replaced by $\hat{\boldsymbol{\varepsilon}}(\mathbf{r},\omega)+\Delta\hat{\boldsymbol{\varepsilon}}(\mathbf{r},\omega)$, with the perturbation $\Delta\hat{\boldsymbol{\varepsilon}}(\mathbf{r},\omega)$ in the form of Eq. (3.16) described by $\Delta\hat{\boldsymbol{\varepsilon}}_\infty(\mathbf{r})$ and $\Delta\hat{\boldsymbol{\sigma}}_j(\mathbf{r})$, non-zero only inside the unperturbed system. The poles of the perturbation are at the same frequencies Ω_j but have different weights:

$$\Delta\hat{\boldsymbol{\varepsilon}}(\mathbf{r},\omega)=\Delta\hat{\boldsymbol{\varepsilon}}_\infty(\mathbf{r})+\frac{i\Delta\hat{\boldsymbol{\sigma}}_j(\mathbf{r})}{\omega-\Omega_j}. \tag{3.16}$$

The formal solution the electric field $\mathbf{E}(\mathbf{r})$ and the eigenfrequency k of a perturbed RS is found using the integral equation [35]

$$\mathbf{E}(\mathbf{r})=-k^2\int\hat{\mathbf{G}}_k(\mathbf{r},\mathbf{r}')\Delta\hat{\boldsymbol{\varepsilon}}(\mathbf{r}',\omega)\mathbf{E}(\mathbf{r}')d\mathbf{r}' \tag{3.17}$$

and can be split into the individual Lorentzian terms with the corresponding form of the GF used in each term

$$\mathbf{E}(\mathbf{r})=-k^2\int\hat{\mathbf{G}}^0_k(\mathbf{r},\mathbf{r}')\Delta\hat{\boldsymbol{\varepsilon}}_\infty(\mathbf{r})\mathbf{E}(\mathbf{r}')d\mathbf{r}'-k^2\sum_j\hat{\mathbf{G}}^j_k(\mathbf{r},\mathbf{r}')\frac{i\Delta\hat{\boldsymbol{\sigma}}_j(\mathbf{r})}{\omega-\Omega_j}\mathbf{E}(\mathbf{r}')d\mathbf{r}' \tag{3.18}$$

Expanding the perturbed RSs into the complete basis of unperturbed ones,

$$\mathbf{E}(\mathbf{r})=\sum_n c_n\mathbf{E}_n(\mathbf{r})\,, \tag{3.19}$$

and equating the expansion coefficients at different basis functions $\mathbf{E}_n(\mathbf{r})$ results in a quadrilateral eigenvector equation. This is the RSE with dispersion.

$$k_n\sum_m\left(\delta_{nm}+\frac{U_{nm}}{2}\right)c_m=k\sum_m\left(\delta_{nm}+\frac{V_{nm}}{2}\right)c_m \tag{3.20}$$

where the matrix elements defined by

$$V_{nm}=\int\mathbf{E}_n(\mathbf{r})\,\cdot\,\Delta\hat{\boldsymbol{\varepsilon}}_\infty(\mathbf{r})\mathbf{E}_m(\mathbf{r})\,d\mathbf{r} \tag{3.21}$$

$$U_{nm}=\sum_j\frac{B^j_{nm}}{\omega_n-\Omega_j} \tag{3.22}$$

$$B^j_{nm}=\int\mathbf{E}_n(\mathbf{r})\,\cdot\,\Delta\hat{\boldsymbol{\sigma}}_j(\mathbf{r})\mathbf{E}_m(\mathbf{r})\,d\mathbf{r}\,. \tag{3.23}$$

3.2 Eigenmodes of a sphere

Applying the RSE to a nanosphere requires us to first know the basis. We choose here the RSs of a nanosphere with dispersive permittivity of radius R surrounded by vacuum, since they are analytically known. The basis functions of a dielectric sphere are shown in a previous paper on the RSE in 3D systems [5]. The solutions of Maxwell's equations split into four groups: TE, TM, longitudinal electric (LE), and longitudinal magnetic (LM) modes [36] for a spherically symmetric system. In this section we will be considering TM solutions only as surface plasmons appear in TM polarisation. Note for this section we use $c = 1$ therefore $k = \omega$. The TM group of modes of a dispersive sphere can be written as

$$i\mathbf{H} = -\mathbf{r} \times \nabla f \qquad \text{and} \qquad \mathbf{E} = \frac{\nabla \times i\mathbf{H}}{\varepsilon(r,k)k}\,, \tag{3.24}$$

where $f(\mathbf{r})$ is a scalar function satisfying the Helmholtz equation

$$\nabla^2 f + k^2 \varepsilon(r,k) f = 0\,, \tag{3.25}$$

with the permittivity of the dielectric sphere in vacuum given by

$$\varepsilon(r,k) = \begin{cases} n_R(k)^2 & \text{for} \quad r \leqslant R \\ 1 & \text{for} \quad r > R\,, \end{cases} \tag{3.26}$$

where $n_R(k) = n(k) + i\kappa(k)$. Owing to the spherical symmetry of the system, the solution of Eq. (3.25) splits in spherical coordinates $\mathbf{r} = (r, \theta, \varphi)$ into the radial and angular components:

$$f(\mathbf{r}) = R_l(r,k) Y_{lm}(\Phi)\,, \tag{3.27}$$

where $\Phi = (\theta, \varphi)$ with the angle ranges $0 \leqslant \theta \leqslant \pi$ and $-\pi \leqslant \varphi \leqslant \pi$. The angular component is given by the spherical harmonics,

$$Y_{lm}(\Phi) = \sqrt{\frac{2l+1}{2}\frac{(l-|m|)!}{(l+|m|)!}} P_l^{|m|}(\cos\theta)\chi_m(\varphi)\,, \tag{3.28}$$

where $P_l^m(x)$ are the associated Legendre polynomials, which are the eigenfunctions of the angular part of the Laplacian $\hat{\Lambda}$,

$$\hat{\Lambda}(\Phi)Y_{lm}(\Phi) = -l(l+1)Y_{lm}(\Phi)\,, \tag{3.29}$$

Note that the azimuthal functions are defined here as real functions

$$\chi_m(\varphi) = \begin{cases} \pi^{-1/2}\sin(m\varphi) & \text{for} \quad m < 0 \\ (2\pi)^{-1/2} & \text{for} \quad m = 0 \\ \pi^{-1/2}\cos(m\varphi) & \text{for} \quad m > 0\,, \end{cases} \tag{3.30}$$

in order to satisfy the orthogonality condition without using the complex conjugate, as required by Eq. (1.5). The radial components $R_l(r,k)$ satisfy the spherical Bessel equation,

$$\left[\frac{d^2}{dr^2} + \frac{2}{r}\frac{d}{dr} - \frac{l(l+1)}{r^2} + \varepsilon(r,k)k^2\right] R_l(r,k) = 0 \tag{3.31}$$

and have the following form

$$R_l(r,k) = \begin{cases} j_l(n_R(k)kr)/j_l(n_R(k)kR) & \text{for} \quad r \leqslant R \\ h_l(kr)/h_l(kR) & \text{for} \quad r > R\,, \end{cases} \tag{3.32}$$

in which $j_l(z)$ and $h_l(z) \equiv h_l^{(1)}(z)$ are, respectively, the spherical Bessel and Hankel functions of the first kind, where $z = n_R(k)kR$.

In spherical coordinates, a vector field $\mathbf{E}(\mathbf{r})$ can be written as

$$\mathbf{E}(r,\theta,\varphi) = E_r\mathbf{e}_r + E_\theta\mathbf{e}_\theta + E_\varphi\mathbf{e}_\varphi = \begin{pmatrix} E_r \\ E_\theta \\ E_\varphi \end{pmatrix}\,,$$

where $\mathbf{e}_r$, $\mathbf{e}_\theta$, and $\mathbf{e}_\varphi$ are the unit vectors. The electric field of the RSs then has the form

$$\mathbf{E}_n^{\mathrm{TM}}(\mathbf{r}) = \frac{A_{\mathrm{TM}}(k_n)}{\varepsilon(r,k_n)k_n r}\begin{pmatrix} l(l+1)R_l(r,k_n)Y_{lm}(\Phi) \\ \dfrac{\partial}{\partial r} r R_l(r,k_n)\dfrac{\partial}{\partial\theta}Y_{lm}(\Phi) \\ \dfrac{\partial}{\partial r}\dfrac{rR_l(r,k_n)}{\sin\theta}\dfrac{\partial}{\partial\varphi}Y_{lm}(\Phi) \end{pmatrix} \tag{3.33}$$

for TM modes. We require that the RSs are normalized according to [14]

$$\begin{aligned} 1+\delta_{0,k_n} \;=\; & \int_V \mathbf{E}_n(\mathbf{r}) \cdot \left.\frac{\partial(k^2\hat{\boldsymbol{\varepsilon}}(\mathbf{r},k))}{\partial(k^2)}\right|_{k_n} \mathbf{E}_n(\mathbf{r})\, d\mathbf{r} \\ & + \frac{1}{2k_n^2}\oint_{S_V}\left(\mathbf{E}_n \cdot \frac{\partial \mathbf{G}_n}{\partial s} - \mathbf{G}_n \cdot \frac{\partial \mathbf{E}_n}{\partial s}\right) dS\,, \end{aligned} \tag{3.34}$$

where $\mathbf{G}_n = (\mathbf{r}\cdot\nabla)\mathbf{E}_n$, V is an arbitrary simply connected volume with a boundary surface S_V enclosing the inhomogeneity of the system, and the derivative $\partial/\partial s$ is taken along the outer surface normal. This leads to the following normalisation constant [27]:

$$A_{\mathrm{TM}}(k) = \frac{\sqrt{\frac{2\varepsilon}{l(l+1)R^3(\varepsilon-1)}}}{\sqrt{\left(\frac{j_{l-1}(z)}{j_l(z)} - \frac{l}{z}\right)^2 + \frac{l(l+1)}{k^2R^2} + \eta(k)C_l(k)}}\,, \tag{3.35}$$

where the dispersion has given rise to the terms

$$\eta(k) = \frac{1}{\varepsilon}\frac{\partial(k^2\varepsilon)}{\partial(k^2)} - 1 \tag{3.36}$$

$$C_l(k) = \frac{\varepsilon}{\varepsilon-1}\left(\frac{2(l+1)}{z^2} + \frac{j_{l+1}^2(z)}{j_l^2(z)} - \frac{j_{l+2}(z)}{j_l(z)}\right). \tag{3.37}$$

The Maxwell boundary conditions, namely the continuity of the tangential components of $\mathbf{E}$ and $\mathbf{H}$ across the spherical material-vacuum interface, lead to the the fields given by Eq. (3.24) to the following secular equation determining the RS wavenumbers k_n, ($z_n = n_R(k_n)k_nR$):

$$\frac{n_R(k)j_l'(z_n)}{j_l(z_n)} - \frac{n_R^2(k)h_l'(k_nR)}{h_l(k_nR)} - \frac{n_R^2(k)-1}{k_nR} = 0 \tag{3.38}$$

where $j_l'(z)$ and $h_l'(z)$ are the derivatives of $j_l(z)$ and $h_l(z)$, respectively. While the

LE modes are the RSs easiest to calculate due to a simple power-law form of their radial functions,

$$R_l(r,0) = \begin{cases} (r/R)^l & \text{for} \quad r \leqslant R \\ (R/r)^{l+1} & \text{for} \quad r > R\,, \end{cases} \tag{3.39}$$

we treat them in the RSE as part of the TM family of RSs. Indeed, for $r \leqslant R$ they coincide with the TM modes taken in the limit $k_n \to 0$:

$$\mathbf{E}_n^{\mathrm{LE}}(\mathbf{r}) = \sqrt{l(n_R^2(k_n)-1)} \lim_{\omega_n \to 0} \mathbf{E}_n^{\mathrm{TM}}(\mathbf{r})\,. \tag{3.40}$$

Even though $k_n = 0$ is not a solution to the secular equation Eq. (3.38), using the analytic dependence of the wave functions of TM modes on k_n is taken into account when calculating the matrix elements containing LE modes. This limit $k_n \to 0$ has to be carefully approached in the matrix eigenvalue problem Eq. (3.20) due to the divergent behaviour. We found that adding a finite negative imaginary part to static poles, $k_n R = -i\delta$, with δ typically of order 10^{-7} (determined by the numerical accuracy) is suited to the RSE converging to the correct solution [5]. Note this solution is not needed if we include a Drude pole due to the Ohm's law contribution having a pole at $k_n = 0$ already, as previously stated.

There are an infinite number of RSs in theory so we muist truncate them in order to have a finite set of states. The condition we use is $|n_R(k_n)k_n| < k_{\max}$ where $k_{\max} \approx 1$ and can be modified to select the most suitable states.

3.3 Dispersive to dispersive perturbation

Due to the nature of Eq. (3.38), we expect an infinite number of RS frequencies close to the poles in $\hat{\boldsymbol{\varepsilon}}(\mathbf{r}, \omega_n)$. These arise from the secular equation due to the argument of the spherical bessel functions diverging at the pole $z = n_R(\omega)kR$. The addition of a pole in $\hat{\boldsymbol{\varepsilon}}(\mathbf{r}, \omega_n)$ doubles the size of the basis compared with a constant permittivity, with $n_R(\omega)$ no longer constant there are non-degenerate solutions of the secular equation around the pole position.

In order to find suited starting points for the numerical solutions of Eq. (3.38)

for these solutions, we observe that the approximate values of these frequencies can be derived using an approximation for spherical Bessel functions,

$$j_l(z) \approx \frac{1}{z}\cos\left(z - \pi\frac{l+1}{2}\right) \tag{3.41}$$

$$\frac{j_l'}{j_l(z)} \approx -\tan\left(z - \pi\frac{l+1}{2}\right) \tag{3.42}$$

which can be used in Eq. (3.38), results in the approximate secular equation,

$$\tan\beta = -\frac{n_R(\omega)h_l'(kR)}{h_l(kR)} - \frac{n_R^2(\omega)-1}{z}\,, \tag{3.43}$$

where

$$\beta = z - \frac{\pi(l+1)}{2}. \tag{3.44}$$

This means that as the pole-related RSs get closer to the pole, $\tan\beta \to \infty$ giving us a set of solution for $\beta \approx \frac{\pi}{2}, \frac{3\pi}{2}, \frac{5\pi}{2}, ...$, therefore

$$\beta \approx \pi\left(m + \frac{1}{2}\right)\,.$$

with $m > 0$. Using Eq. (3.44), we can now write an expression for z

$$z = n_R(\omega)kR \approx \pi\left(\frac{l+2m}{2}\right)\,. \tag{3.45}$$

Eq. (3.45) can now be used to calculate the approximate position of the RS frequencies, with respect to the original Drude or Lorentz pole, by substituting in the appropriate values of the refractive index depending on the model. Assuming m is an infinite number of positive integer values, our new frequencies will get closer to the non-zero pole in $\hat{\boldsymbol{\varepsilon}}(\mathbf{r},\omega)$ as m increases.

For the Drude-Lorentz model the refractive index of the pole-related RSs around one of the poles is single term only, as all other terms are negligible due to $\omega - \Omega_j$ being very small,

$$n_R^2(\omega) = \varepsilon(\omega) \approx -\frac{i\sigma_j}{\Delta\omega_j} \tag{3.46}$$

where $\Delta\omega_j = \omega - \Omega_j$ and $\omega \approx \Omega_j$. Here $\Delta\omega_j$ is used to represent the separation

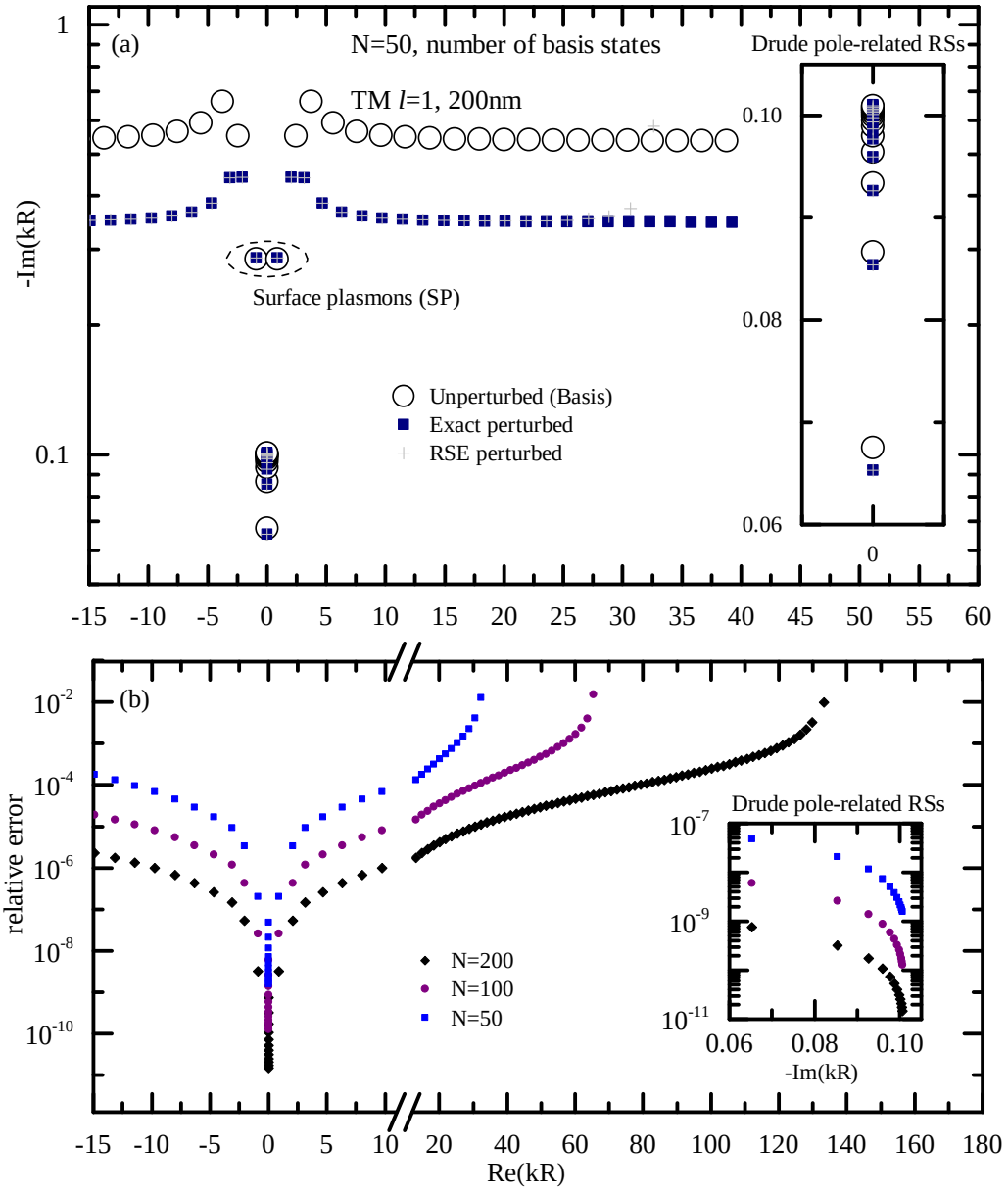

Figure 3.1: (a) Frequency space graph showing the basis states as well as both the exact and RSE perturbed solutions, inset shows the same for the Drude pole-related RSs. n is perturbed from 1.5 to 2.5 and the conductivity of the Drude pole $\hbar\sigma = 100$ to 110eV. Drude pole position is $-0.1i$. (b) The relative error with an inset showing the error of the Drude pole-related RSs.

between the pole and the pole-related RSs. By combining Eq. (3.45) and Eq. (3.46), we can write an expression for the separation between the pole-related RSs and the exact position of the pole

$$\Delta\omega_j \approx \frac{i\sigma_j \Omega_j^2 R^2}{\pi^2 \left(\frac{l}{2} + m\right)^2}. \tag{3.47}$$

We use $\omega = \Omega_j + \Delta\omega_j$ as a guess value for solving Eq. (3.38).

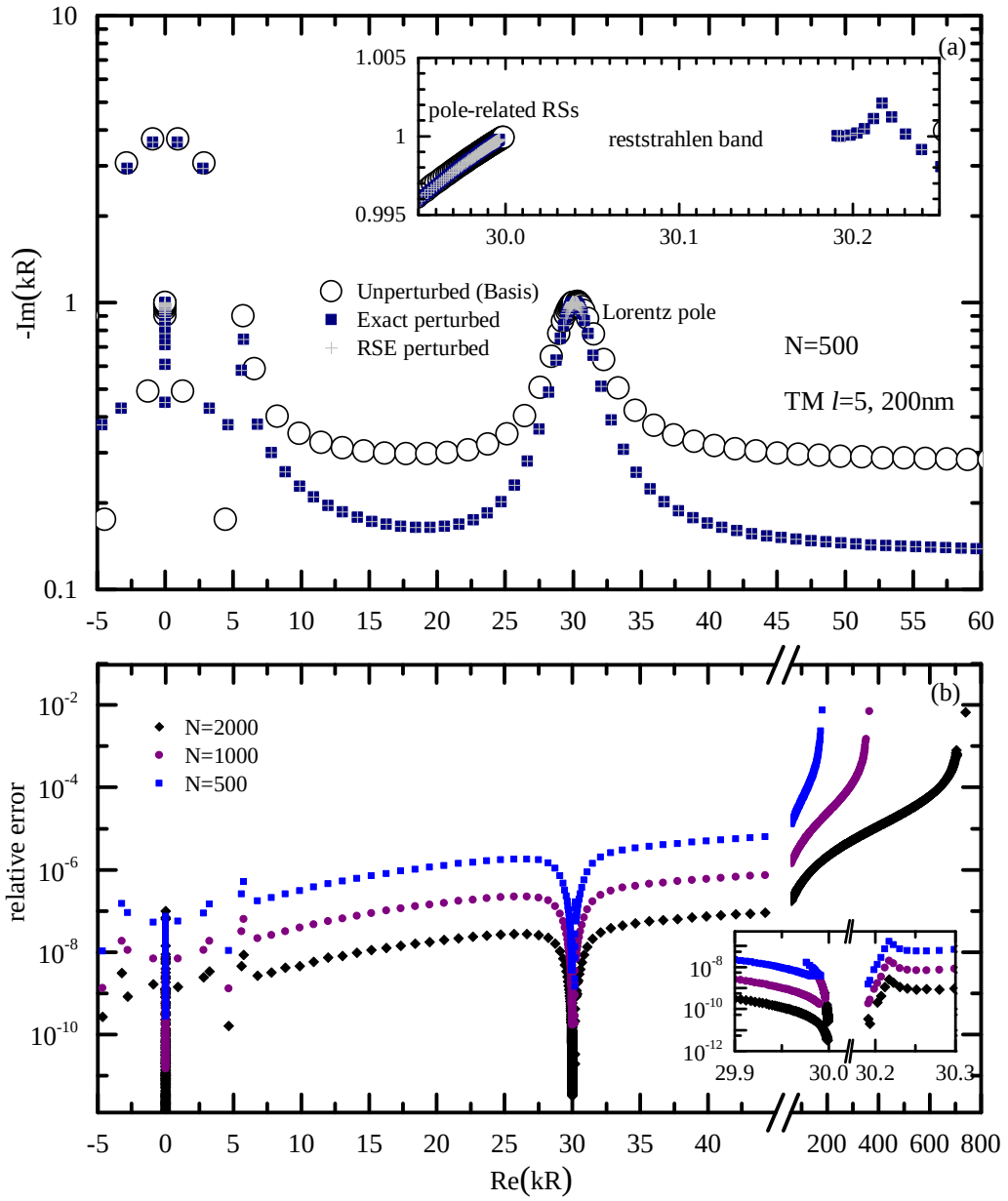

Figure 3.2: (a) As Fig. 3.1, but the inset also shows the reststralen band where no modes exist. n is perturbed from 1.5 to 2.5 and the conductivity of the Drude pole $\hbar\sigma$= 10 to 110eV with the Drude pole at $-i$. $\Omega_1 = 30 - i$ with σ_1 perturbed from 1.0 to 4.0 eV. (b) The relative error with an inset showing the error of the Lorentz pole-related RSs.

The inclusion of Drude or Lorentz poles is a step closer toward a realistic model with which to model metallic spheres. From Fig. 3.1, which shows the perturbation of a dispersive basis with a Drude pole. The RSE solution is compared with the exact solution which is found in the same way as the basis but with the perturbed permittivity. The error of RSE solution diverges away from the exact solution at

high frequencies when approaching the edge of the basis used. This is an expected effect of the finite basis, and can be controlled via the basis size chosen. The goal is to not calclate the exact solution at all as the RSE is much faster, however we need to include some checks to make sure the calculations are staying on track from a computational point of view. This can be done by calculating a few prominent and sensitive RSs in order to check against the RSE solution and prevents spurious solutions.

The inset of Fig. 3.1(a) shows the new pole-related frequencies which come from the solution to Eq. (3.38). As in Fig. 1.2, we see the error scale as $\frac{1}{N^3}$, where N is the number of RSs, which means the RSE solution converges very quickly to the exact solution, equal to the non-dispersive RSE . We choose a cut off criteria for the basis states where $|n_R(k_n)k_n| < k_{\max}$ which limits the RSs at the high frequencies and the pole-related RSs with large $n_R(k_n)$ ($k_{\max} \approx 1$).

We also see the introduction of surface plasmons (SPs) in Fig. 3.1 which comes from modelling a metallic nanosphere which are important modes for applications such as plasmonic biosensing. These are modes which propagate along the surface of the sphere [37, 38] and are the conduction electrons resonating with an incoming ray of light. The resonance is at the interface and decays exponantially either side. As previously mentioned, they only appear with TM polarisation, due to the permeability (μ) of any material always being positive so there is never an electric field component along the surface for excitaion during TE polarisation.

In Fig. 3.2 we expand upon that by introducing a Lorentz pole into $\hat{\boldsymbol{\varepsilon}}(\mathbf{r}, \omega)$. We still see excellent agreement between the exact solution and the RSE with the relative error scaling as $\frac{1}{N^3}$. The inset of Fig. 3.2(a) shows what we call the 'rest-strahlen band' which appears as a result of the presence of the Lorentz pole. This phenomenon is discussed in more detail in Sec. 3.5.3.

3.4 Infinitesimal-dispersive basis to dispersive

In this section we apply the dispersive RSE to metal and semiconductor nanoparticles, by taking as the basis (unperturbed) system a dielectric sphere with no dis-

persion. This approach has been already used in [34], however in the case of the Drude model only. Here we apply the same method to a system with dispersion of the permittivity involving up to three pairs of Lorentz poles.

The reason for using an infinitesimal-dispersive basis for the RSE is to be able to perturb σ_j from zero to something finite, essentially creating poles where there weren't any before. As previously mentioned, due to the nature of Eq. (3.16) we expect an infinite number of RSs close to the poles in $\hat{\boldsymbol{\varepsilon}}(\mathbf{r}, \omega_n)$ ($\omega_n = k_n c$), for an infinitesimal-dispersive basis this manifests itself as an infinite number of degenerate modes sitting at the pole position which has zero weight in the permittivity ($\sigma_j \to 0$). Technically, this causes divergences in Eq. (3.22) because $\omega_n = \Omega_j$ but this can be solved by introducing a factor which equals zero for the pole-related RSs and one for normal RSs. This factor, which we call α_n, removes the divergences by multiplying them by zero giving us a finite value (due to zero divided by zero):

$$\alpha_n = \begin{cases} 1 & \text{for normal RSs} \\ \sqrt{\frac{\omega_n - \Omega_j}{\Omega_j}} & \text{for degenerate modes.} \end{cases} \tag{3.48}$$

This allows us to properly take the limit $\sigma \to 0$ as $\sqrt{\omega_n - \Omega_j}$ due to the new RSE matrix equation remaining finite. This new equation, along with the perturbation matrices are defined using this new factor α_n.

We will first look at the divergence in the normalisation of the perturbation matrices which stems from η Eq. (3.36). If we assume our permittivity is of the form

$$\varepsilon(\omega) = \varepsilon_\infty + \frac{\sigma}{\omega - \Omega}\,, \tag{3.49}$$

in the limit that $\sigma \to 0$ and $\omega \to \Omega$ we can write $\omega_n - \Omega = \sigma/\beta_n$ where $\varepsilon(\omega) = \varepsilon_\infty + \beta_n = \varepsilon_n$. We cannot solve the secular equation Eq. (3.38) for the frequencies directly, due to the divergences, but we can solve for n_R due to all the frequency degenerate modes having a unique n_R. Here $\varepsilon_n = n_R^2$. The divergence is within the differential of $\varepsilon(\omega)$

$$\frac{d\varepsilon(\omega)}{d\omega}(\omega_n) = -\frac{\beta_n}{\omega_n - \Omega} \to \infty \tag{3.50}$$

which, if we look at Eq. (3.36), leads to

$$\eta = \frac{\omega}{2\varepsilon(\omega)}\frac{d\varepsilon(\omega)}{d\omega}\bigg|_{\omega_n} = -\frac{\omega_n}{2\varepsilon_n}\frac{\beta_n}{\omega_n - \Omega} \to \infty. \tag{3.51}$$

This can be solved with the factor α_n we introduced earlier by modifying η to no longer be divergent:

$$\overline{\eta} = \eta\alpha_n^2 = -\frac{\omega_n}{2\varepsilon_n}\frac{\beta_n}{\omega_n - \Omega}\alpha_n^2 = \frac{(\varepsilon_\infty - \varepsilon_n)}{2\varepsilon_n}\frac{\omega_n}{\Omega_j}. \tag{3.52}$$

The normalisation for TM polarisation (Eq. (3.35)) can be written as

$$\frac{1}{A_{\mathrm{TM}}} = \frac{l(l+1)R^3(\varepsilon(\omega)-1)}{2\varepsilon(\omega)}\left[\underbrace{\left(\frac{j_{l-1}(z)}{j_l(z)} - \frac{l}{z}\right)^2 + \frac{l(l+1)}{k^2R^2}}_{A} + \eta C_l(k)\right] \tag{3.53}$$

where for the the new normalisation we replace η and multiply A by α_n^2 to ensure the factor has been universally applied, which gives us

$$\frac{1}{\overline{A}_{\mathrm{TM}}} = \frac{l(l+1)R^3(\varepsilon_n - 1)}{2\varepsilon_n}\left[A\alpha_n^2 + \overline{\eta}C_l(k)\right] \tag{3.54}$$

We introduce two new and finite perturbation matrices and eigenvectors

$$S_{nm} = \frac{U_{nm}{\alpha_n}^2}{2\alpha_n\alpha_m}, \qquad Q_{nm} = \frac{V_{nm}}{2\alpha_n\alpha_m}, \qquad b_n = \alpha_n c_n, \tag{3.55}$$

and substitute them into Eq. (3.20) to give us a new, but mathematically identical, RSE equation

$$\sum_m \left(\delta_{nm}\omega_n - S_{nm}\right) b_m = \omega \sum_m \left(\delta_{nm} + Q_{nm}\alpha_n^2\right) b_m. \tag{3.56}$$

In order for S_{nm} and Q_{nm} to be finite and Eq. (3.56) resolves all divergences, we have use the new normalisation $\overline{A}_{\mathrm{TM}}$ which compensates for $\alpha_n\alpha_m$ in the denominator.

In general we can say

$$\widetilde{A}_{\mathrm{TM}} = \begin{cases} A_{\mathrm{TM}} & \text{for normal RSs} \\ \overline{A}_{\mathrm{TM}} & \text{for pole-related RSs.} \end{cases} \tag{3.57}$$

When using the RSE to calculate the new RSs it is also important to note there are multiple terms for the matrix equations, but the contributions for the pole-related RSs come only from the corresponding terms in Eq. (3.22) as all other terms are removed by α_n. For the Lorentz poles, which are made up of a pair of poles, even the equal and opposite pole is removed. We take Eq. (3.23) and split it into the corresponding pole. For the Drude pole

$$B_{nm} = \int \mathbf{E}_n(\mathbf{r}) \cdot \Delta\hat{\boldsymbol{\sigma}}(\mathbf{r})\mathbf{E}_m(\mathbf{r})\, d\mathbf{r}\,, \tag{3.58}$$

and for the Lorentz poles where p is the Lorentz pole number ($p = 1, 2, 3, ...$),

$$B^{p}_{nm} = \int \mathbf{E}_n(\mathbf{r}) \cdot \Delta\hat{\boldsymbol{\sigma}}_p(\mathbf{r})\mathbf{E}_m(\mathbf{r})\, d\mathbf{r} \tag{3.59}$$

$$B^{p*}_{nm} = \int \mathbf{E}_n(\mathbf{r}) \cdot \Delta\hat{\boldsymbol{\sigma}}^*_p(\mathbf{r})\mathbf{E}_m(\mathbf{r})\, d\mathbf{r}. \tag{3.60}$$

The independence of the poles is shown below using Eq. (3.22), Eq. (3.58), Eq. (3.59) and Eq. (3.60). By starting with U_{nm} for a fully dispersive set of basis states which includes a Drude and a Lorentz pole,

$$U_{nm} = \underbrace{\frac{-\gamma B_{nm}}{\omega_n + i\gamma}}_{\text{Drude part}} + \underbrace{\frac{\omega_n B^1_{nm}}{\omega_n - \Omega_1} + \frac{\omega_n B^{1*}_{nm}}{\omega_n + \Omega^*_1}}_{\text{Lorentz part}} \tag{3.61}$$

we can show what it would look like, for example, for the infinitesimal-dispersive Drude pole-related RSs only (all Lorentz terms are removed),

$$U_{nm}\alpha_n^2 = \frac{-\gamma B_{nm}}{\omega_n + i\gamma}\frac{\omega_n + i\gamma}{-i\gamma} = -iB_{nm}. \tag{3.62}$$

With this set up we are able to perturb basis states from one realistic material to another by having the poles for both materials present in the basis RSs. This is a

good approach when the materials differ greatly i.e. non-dispersive to dispersive. This approach can also be used for changes in the positions of poles. However if the change in position is small enough this change can be accounted for using a 1^{st}-order perturbation, see Sec. 3.7.2.

3.5 Results for infinitesimal-dispersive basis

3.5.1 Results for metals

As described in Sec. 2 we can fit any experimental data for the permittivity with the Drude-Lorentz model and can do so by choosing the value for ε_∞. This is favourable for us when using the RSE as we can adjust this parameter to give us the best set of RSs for optimum accuracy. The parameters for this fit are shown in Table 3.1 In Fig. 3.3(a) we see a fit using $\varepsilon_\infty = 0.5$ and a Drude and three Lorentz poles. This has been fitted to the data for gold from Johnson and Chrity's paper with an S-value of roughly $\sqrt{2}$ fulfilling our condition for an accurate fit ($S = 1.48$).

We start with a nanosphere of silica ($n = 1.4585$) in the basis with the Drude and Lorentz poles for gold present but with zero weight, these are denoted in Fig. 3.3(b) by γ and Ω_k where $k = 1, 2, 3$. They are lined up with our fit for n and κ to illustrate how they influence the line shape. Note that we need to have the $\omega_n = 0$ pole in the basis as the dispersion is infinitesimally small so behaves like a dielectric.

After pertubation we see the SPs appear due to the nanosphere now being metallic. While in Fig. 3.1 the SPs are clearly seen, for our model of a gold nanosphere of radius 10nm there seem to be multiple modes which can be described as SPs. This is unexpected and seemed to not be the case for spheres modelled with the Drude model only[34]. We will look at the evolution of these modes with respect to radius in Sec. 3.5.2, however for now we can say that there are three SPs in total for this model of gold, one for each of the Lorentz poles. There is also a possible SP above the Drude pole.

The inset in Fig. 3.3(b) shows the pole-related RSs for the first Lorentz pole. For this radius they behave like the RSs for the Drude pole, with the real part opf the frequency hardly changing at all.

We can also see from the figure that the RSE solution matches very well with the exact perturbed solution much like Fig. 3.1, however due to the position of the Lorentz poles it is difficult to reproduce the exact solution for all modes reliably from Eq. (3.38). The RSE can find these solutions without issue due to the completeness of RSs and should work for systems without analytic solutions. Investigating the relative error shows a familiar $\frac{1}{N^3}$ dependence on the number of states we have in our basis. While this is the case for almost all modes, the plasmonic modes seem to saturate at an error in the order of 10^{-6}. This can be seen in the inset of Fig. 3.3(c). While they do decrease as we increase the basis size they converge to the exact solution at a much slower rate than the other modes. We assume that the relative errors we see for the plasmonic modes are sufficient to say the infinitesimal-dispersive RSE is an effective method.

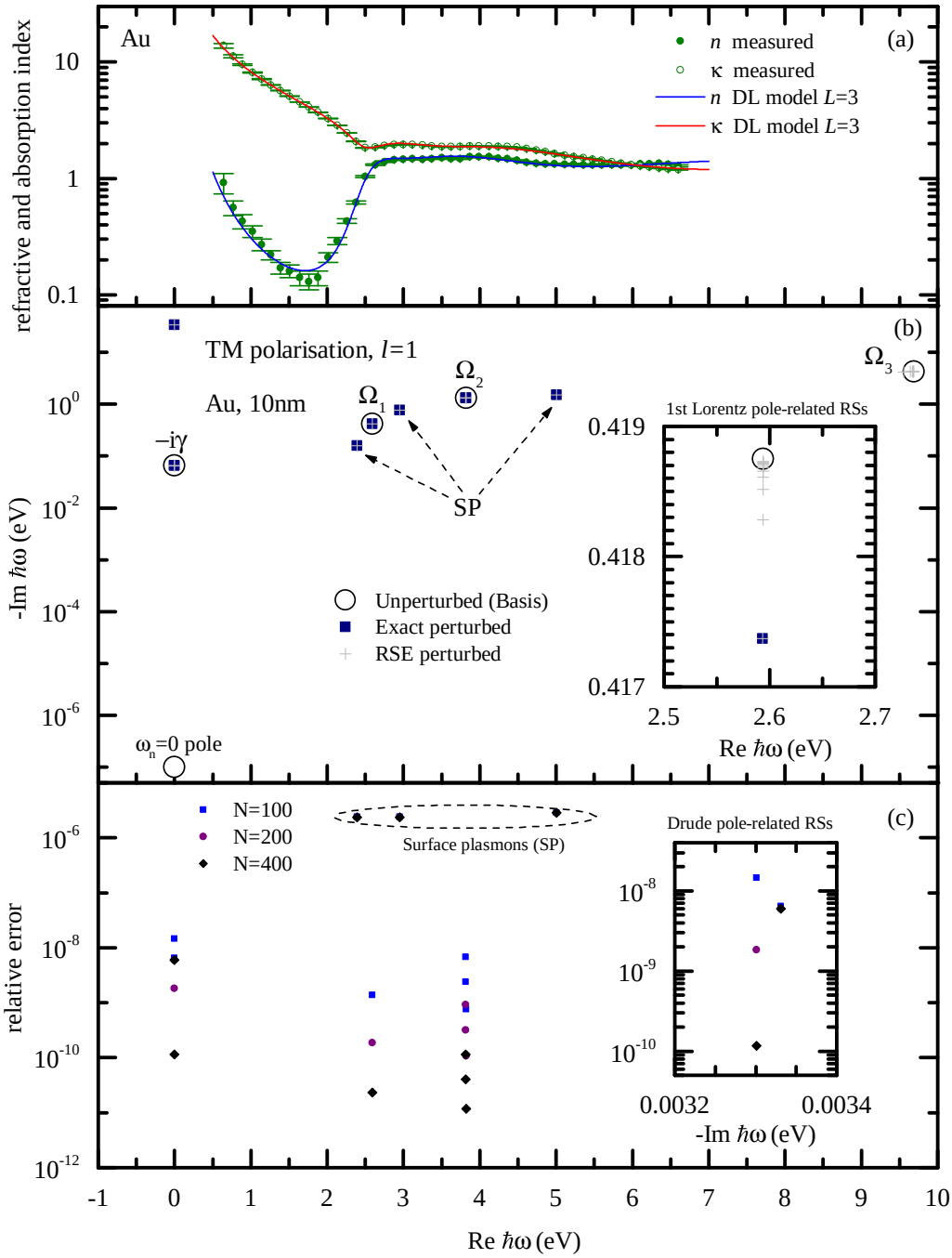

Figure 3.3: (a) Refractive index n and absorption index κ of gold according to [22] (circles and error bars) and the DL model Eq. (2.4) for $L = 3$ (solid lines) as functions of the photon energy $\hbar\omega$. (b) Silica ($n = 1.4585$) to gold (parameters in Table 3.1) with inset showing the first Lorentz pole-related RSs. (c) Relative error of RSE solution compared with the exact perturbed solution. Inset showing the error for the Drude pole-related RSs.

3.5.2 Plasmonic modes

In Sec. 3.5.1, we introduced the phenomenon of multiple SPs at small radii for gold nanospheres. In Fig. 3.4 we look at the evolution of these SPs with respect to nanosphere radius to see which is the fundemental one. In a previous paper on the dispersive RSE [34], we see the prescence of one SP in the RSs of a gold nanosphere which was modelled using the Drude model only, which red-shifts and broadens with radius. Here, the energetically close interband transitions, and thus Lorentz poles, complicate the situation, leading to multiple dipole modes, one for each pole. We show three but there are four in total (including the Drude pole) with the fourth one being ill-defined using the secular equation Eq. (3.38). The absoprtion lineshape is therefore not just a single resonance, but more complex, as also observed in the experiment.

We check the presence of these SPs across a range of 1nm to 100nm in increments of 1nm. We choose a maximum radius of 100nm because with larger spheres the electric field cannot penetrate and stays on surface making the uses of the gold nanoparticles limited. Here we use the dipole mode, $l = 1$ for TM, which contains the fundamental SP. The fundamental SP will have the lowest real part of the energy. We find for small radii, in the dipole limit, the lowest SP has an energy of 2.35 eV and a linewidth of about 0.3 eV, comparable to the absorption features seen in experiments. The second SP at around 2.8 eV has a linewidth of 1.5 eV, and will mostly account for the intraband absorption features seen in the experiments. Note however that in calculating the absorption and scattering properties, these SPs will interfere [18], so that the lineshape is expected to be non-lorentzian, again in agreement with experiment.

With increasing radius, the second SP mode is red-shifting, crossing the first mode around 80nm radius. This will lead to a redshift and broadening of the observed SP resonance in absorption, in qualitative agreement with experiment [39]. To analyse this in more detail, the absorption and scattering cross-sections should be calculated, extending the treatment of [18] to the dispersive RSE, which is beyond the scope of this thesis.

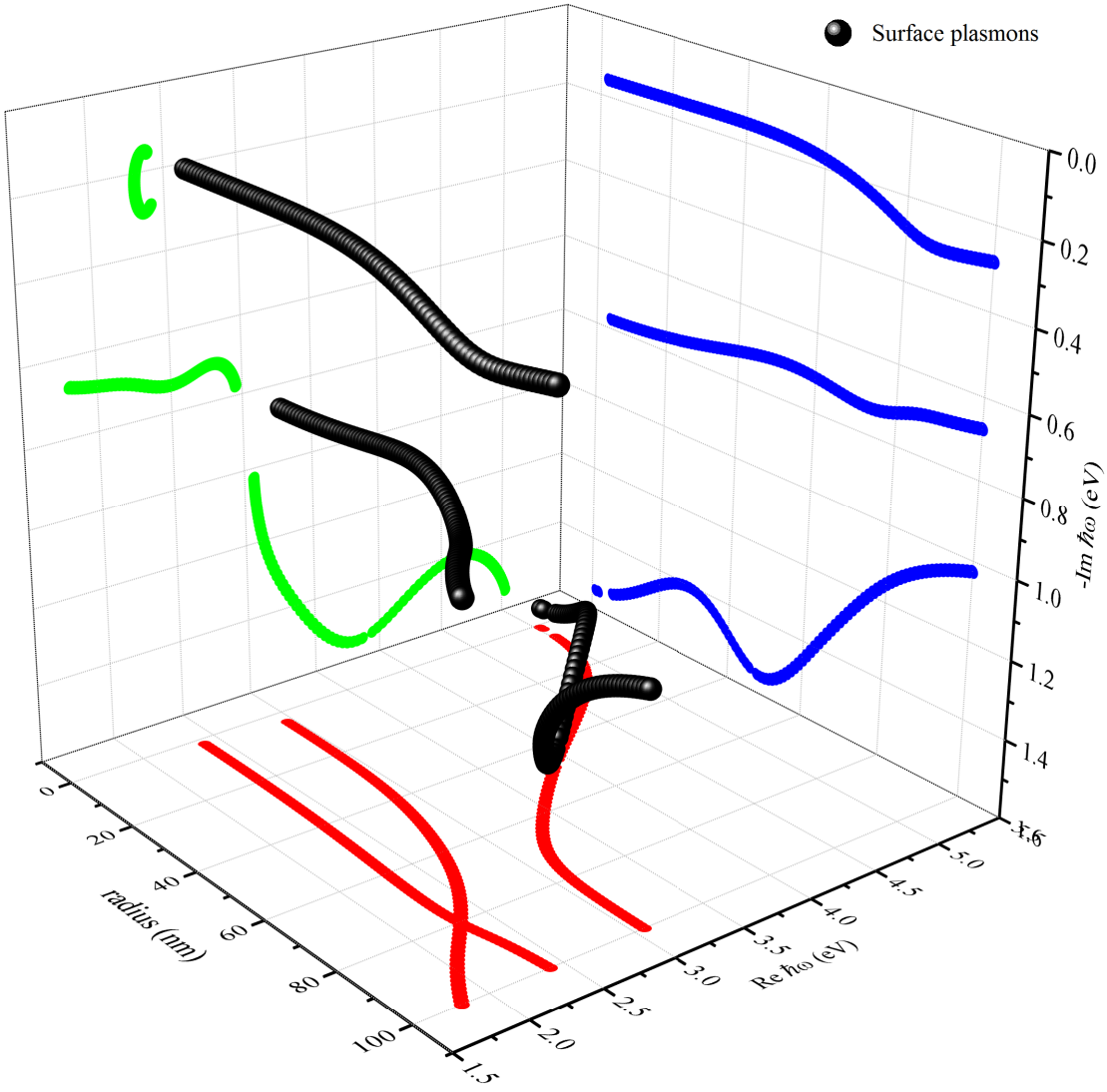

Figure 3.4: 3-D plot of the real and imaginary part of the energy of three SPs with l=1 (dipolar modes), as they evolve with increasing radius of a gold nanosphere. The black spheres show the size evolution in complex space while the projections show the real and imanginary parts separately with respect to radius and to each other.

3.5.3 Results for GaAs

There is a sharp resonance at the phonon energy range (28-40 meV) in GaAs which we can describe by simply using a single Lorentz pole which has a purely imaginary conductivity. This translates to a purely real pole weight and represents a classic Lorentz oscillator as described in Sec. 2.2.1. Fig. 3.5(a) shows the fit of this region. We use the infinitesimal-dispersive RSE to perturb a dielectric nanoshpere, with the same ε_∞ term as GaAs fitted at this range, to the fully dispersive GaAs. Here we choose the l-number and radius of the nanosphere in order for the resonance energy to be in the same range as the WGM.

From Fig. 3.5(b) we see in the inset that there is a gap at the Lorentz pole where there are no modes. This is the reststrahlen band; a region where there are no modes because the permittivity is dominantly negative, so that the waves are non-oscillatory but exponentially decaying which is the case for the real frequencies. Because the permittivity is negative, i.e. $\kappa >> n$, in this region the nanosphere has metallic behaviour.

We can also see this gives us two sets of WGMs either side of the resonance after perturbation. Below the resonance there is an infinite set of WGMs with increasing radial quantum number which are getting denser due to the diverging index and above the reststrahlen band you have a similar set, again increasing the radial quantum number, and merging with the Fabry-Pérot modes.

We have the same situation as Fig. 3.3 where it is difficult to find the exact solution to all of the pole-related RSs while the RSE is able to find them without issue.

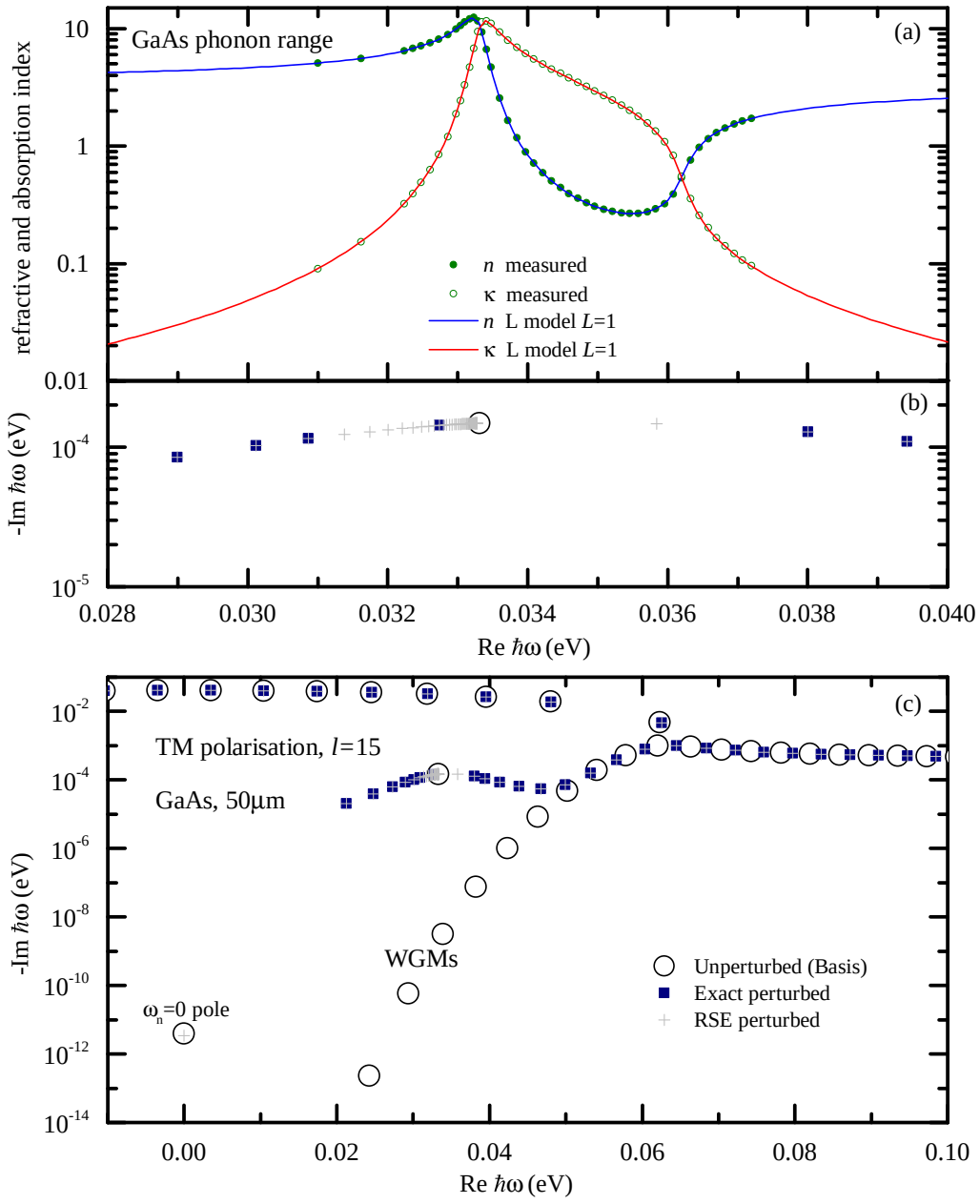

Figure 3.5: (a) Refractive index n and absorption index κ of GaAs in the phonon range [40](circles) and the Lorentz model Eq. (2.4) for $L = 1$ (solid lines) as functions of the photon energy $\hbar\omega$. (b) Dielectric material ($n = 3.317$) to GaAs perturbation showing the Lorentz pole-related RSs and the reststrahlen band around the resonance where there are no RSs. (c) Full picture showing the WGMs and the inclusion of $\omega_n = 0$ due to no drude pole.

3.6 Gain

We simulate gain by fitting the first optical interband transition with Lorentz poles with purely real weights (imaginary conductivities), as in Sec. 3.5.3, and changing the sign of σ_1 from positive to negative. Physically, this results in an increase in optical power due to the sphere transferring energy to the electric field.

In Fig. 3.6(a) we fit the range 1.3-1.65 eV with four Lorentz poles, three of which are at the transition and are very sharp and the fourth being further out and much broader. We can also see the effect of changing the first Lorentz pole into one with gain causing the absorption index κ to become negative around 1.5 eV.

This perturbation is simulated using the RSE in Fig. 3.6(b) and shows the RSs lined up with the energy of the absorption index fit. We can see after the perturbation some of the RSs dip below into the region where they have a positive imaginary part of the frequency which corresponds to gain modes. We only expect a few gain modes due to the small amount of gain we see when we change the conductivity. We chose a sphere of radius 10 microns to show the circular arrangement of pole-related RSs. This arrangement of RSs close to the gain pole (GP), which appears due to the reversed influence of the resonance to the refractive index (n). The refractive index decreases approaching the resonance from lower energies, such that $n_R k$ is limited ($k = \omega/c$), and thus the number of modes is limited. This is the opposite to what is seen for the phonons in GaAs in Fig. 3.5. The Lorentz-pole related RSs then form a circle-shape starting below the pole in the real part, and then circling around to above the pole in real part, where the refractive index is increased, and then towards the pole, where the refractive index diverges and an countable infinite number of RSs are present.

We show a similar plot for modelling gain using a radius of 940nm in Fig. 3.7. We chose this specific radius because the resonance lines up with one of the WGMs and causes it to shift into the positive imaginary region. We also show the evolution of this WGM into a gain mode (GM) as we incrementally change the conductivity from positive to negative with the same magnitude.

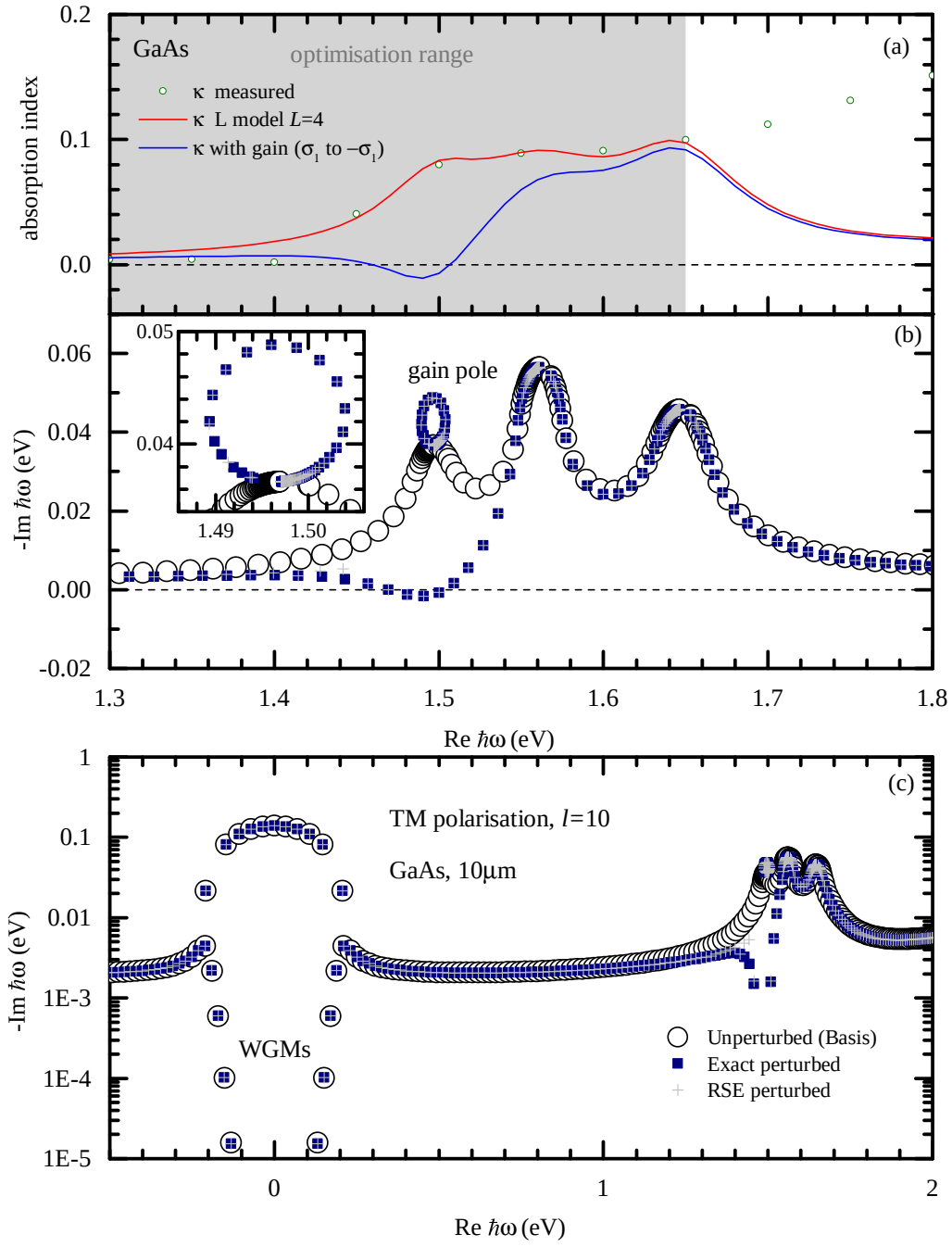

Figure 3.6: (a) Absorption index κ of GaAs in the band gap range at the first interband transition 1.3-1.65eV[40](circles) and the Lorentz model Eq. (2.4) for $L = 4$ (red line) as a function of the photon energy $\hbar\omega$. The blue line models gain in energy for GaAs shown by the absorption index moving into the negative range. (b) Absorption to gain perturbation showing the Lorentz pole-related RSs for the first three Lorentz poles (the fourth is outside the optimisation range). The inset shows the RSs of the perturbed Lorentz pole. (c) Picture in log scale for Im $\hbar\omega$ showing the WGMs and the leaky modes.

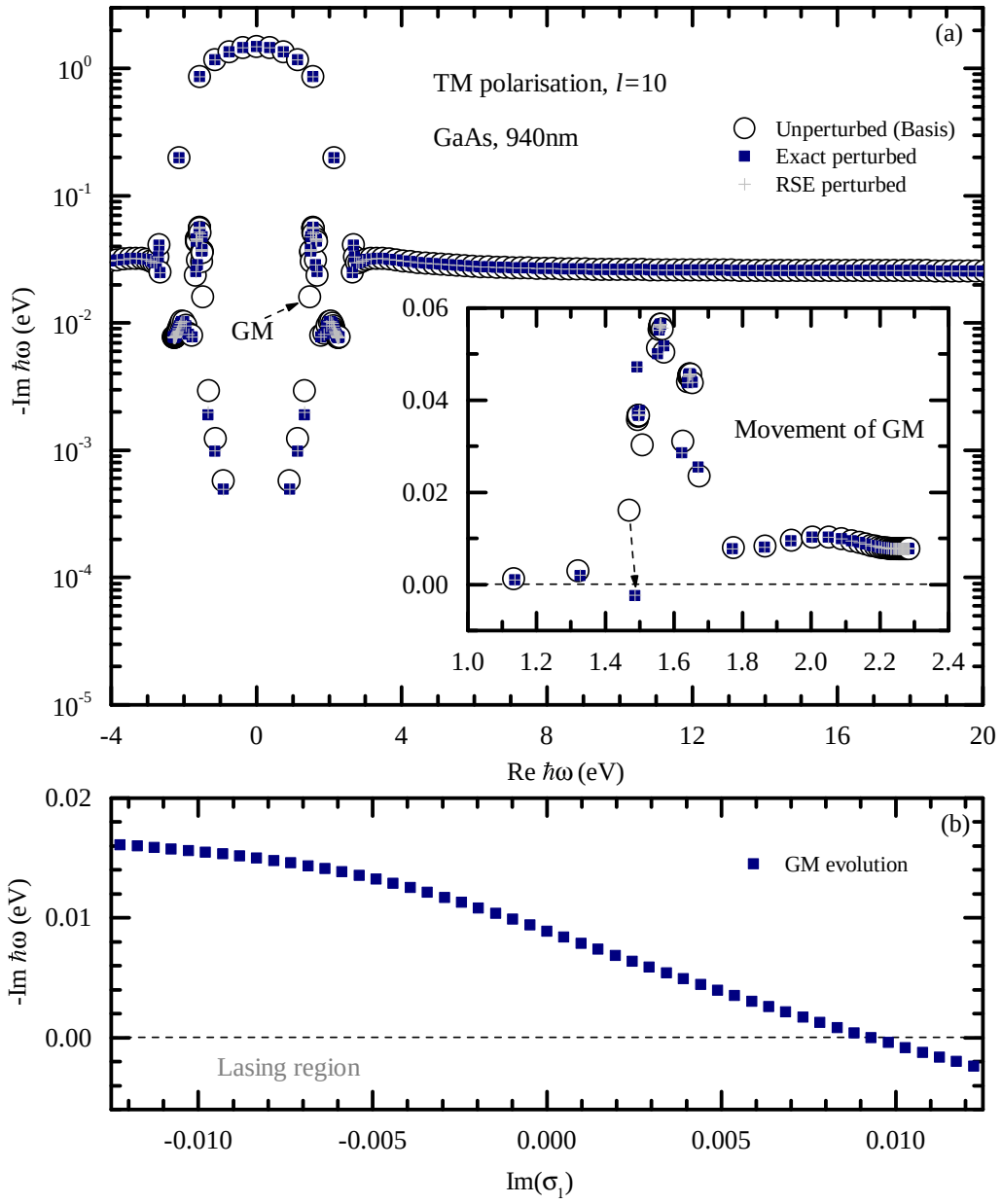

Figure 3.7: (a) Absorption to gain perturbation for GaAs at the first interband transition showing the evolution of a GM. Inset shows the movement from negative to positive Im $\hbar\omega$. (b) Detailed picture of the evolution of the GM with respect to imaginary part of the conductivity Im(σ_1).

3.7 Pole position perturbation

Being a perturbative approach, the RSE is a very efficient method for treating small perturbations of the refractive index, when treating non-dispersive optical systems, or small perturbations of the conductivities, when treating systems with frequency dispersion and using as basis RSs of a dispersive system with the same poles of the permittivity. Indeed, small perturbations of the conductivity or refractive index require only a few RSs to be taken into account in the basis. However, even small changes in the positions of the poles of the permittivity becomes a challenge for the RSE, as they would require to add the shifted pole-related RSs. We therefore explore a possible solution to this problem by replacing small perturbations of the pole positions with changes only of the conductivities in the Drude-Lorentz model and another method where we use 1$^{\text{st}}$-order perturbation, i.e. no off-diagonal matrix elements.

3.7.1 Attempt at an analytic model

By incorporating the pole position shift into $\Delta\sigma_j$ we were hoping to have an elegant solution to a slight prturbation (<5%) to the pole position. While it did not give us the results we wanted it is worth exploring the method for future implementation.

Let's take a pair of symmetric Lorentz poles at postion Ω which has been pertubed to $\widetilde{\Omega}$, the changed part of the permittivity is

$$\Delta\varepsilon(\omega) = \frac{i\Delta\sigma}{\omega - \widetilde{\Omega}} + \frac{i\Delta\sigma^*}{\omega + \widetilde{\Omega}^*} = \sigma f_1(\omega) + \sigma^* f_2(\omega) \tag{3.63}$$

where σ is the old conductivity and

$$f_1(\omega) = \frac{i}{\omega - \widetilde{\Omega}} \qquad\qquad f_2 = \frac{i}{\omega + \widetilde{\Omega}^*}. \tag{3.64}$$

We want to approximate this change by introducing

$$\widetilde{\Delta\varepsilon}(\omega) = \frac{i\Delta\widetilde{\sigma}}{\omega - \Omega} + \frac{i\Delta\widetilde{\sigma}^*}{\omega + \Omega^*} = \widetilde{\sigma} g_1(\omega) + \widetilde{\sigma}^* g_2(\omega) \tag{3.65}$$

where the pole has the same position but a new conductivity $\widetilde{\sigma}$ and

$$g_1(\omega) = \frac{i}{\omega - \Omega} \qquad\qquad g_2 = \frac{i}{\omega + \Omega^*}. \tag{3.66}$$

We do this, in a similar way to Eq. (2.8), by minimising the error

$$E = \int_{-\infty}^{\infty} \left|\Delta\varepsilon - \widetilde{\Delta\varepsilon}\right|^2 \tag{3.67}$$

$$= \int_{-\infty}^{\infty} d\omega \left(\sigma^* f_1^* + \sigma f_2^* - \widetilde{\sigma}^* g_1^* - \widetilde{\sigma} g_2^*\right)\left(\sigma f_1 + \sigma^* f_2 - \widetilde{\sigma} g_1 - \widetilde{\sigma}^* g_2\right) \tag{3.68}$$

by requiring $\frac{\partial E}{\partial \widetilde{\sigma}^*} = 0$ which results in $A\widetilde{\sigma} + B\widetilde{\sigma}^* = C\sigma + D\sigma^*$ where

$$A = \int_{-\infty}^{\infty} d\omega \left(g_1^* g_1 + g_2^* g_2\right) \qquad B = \int_{-\infty}^{\infty} d\omega \left(2 g_1^* g_2\right)$$

$$C = \int_{-\infty}^{\infty} d\omega \left(g_1^* f_1 + f_2^* g_2\right) \qquad D = \int_{-\infty}^{\infty} d\omega \left(g_1^* f_2 + f_1^* g_2\right).$$

From these expressions we can finally obtain an equation for $\widetilde{\sigma}$

$$\frac{\widetilde{\sigma}}{\Omega^* - \Omega} + \frac{\widetilde{\sigma}^*}{2\Omega^*} = \frac{\sigma}{\Omega^* - \widetilde{\Omega}} + \frac{\sigma^*}{\Omega^* + \widetilde{\Omega}^*}. \tag{3.69}$$

We can solve this approximately for small $\widetilde{\Omega} - \Omega$ by substituting in $\Omega = \Omega_0 - i\Gamma$ and $\widetilde{\Omega} = \Omega + \Delta\Omega$ to obtain an expression and taking the complex conjugate of that to obtain a second expression. Use the expressions to eliminate $\widetilde{\sigma}^*$ to produce an expression for $\widetilde{\sigma}$

$$\widetilde{\sigma}\left(\frac{\Omega^*}{i\Gamma} + \frac{i\Gamma}{\Omega}\right) = 2\sigma\left(\frac{\Omega^*}{2i\Gamma - \Delta\Omega} + \frac{i\Gamma}{2\Omega + \Delta\Omega}\right) + 2\sigma^*\left(\frac{\Omega^*}{2\Omega^* + \Delta\Omega^*} - \frac{i\Gamma}{2i\Gamma + \Delta\Omega^*}\right). \tag{3.70}$$

Eq. (3.70) is the exact expression but by using the 1^{st}-order Taylor expansion we obtain

$$\widetilde{\sigma}\left(\frac{\Omega^*}{i\Gamma} + \frac{i\Gamma}{\Omega}\right) \approx \sigma\left(\frac{\Omega^*}{i\Gamma} + \frac{i\Gamma}{\Omega}\right) + \frac{\sigma\Delta\Omega}{2}\left(\frac{\Omega^*}{(i\Gamma)^2} - \frac{i\Gamma}{\Omega^2}\right) + \frac{\sigma^*\Delta\Omega^*}{2}\left(\frac{1}{i\Gamma} - \frac{1}{\Omega^*}\right). \tag{3.71}$$

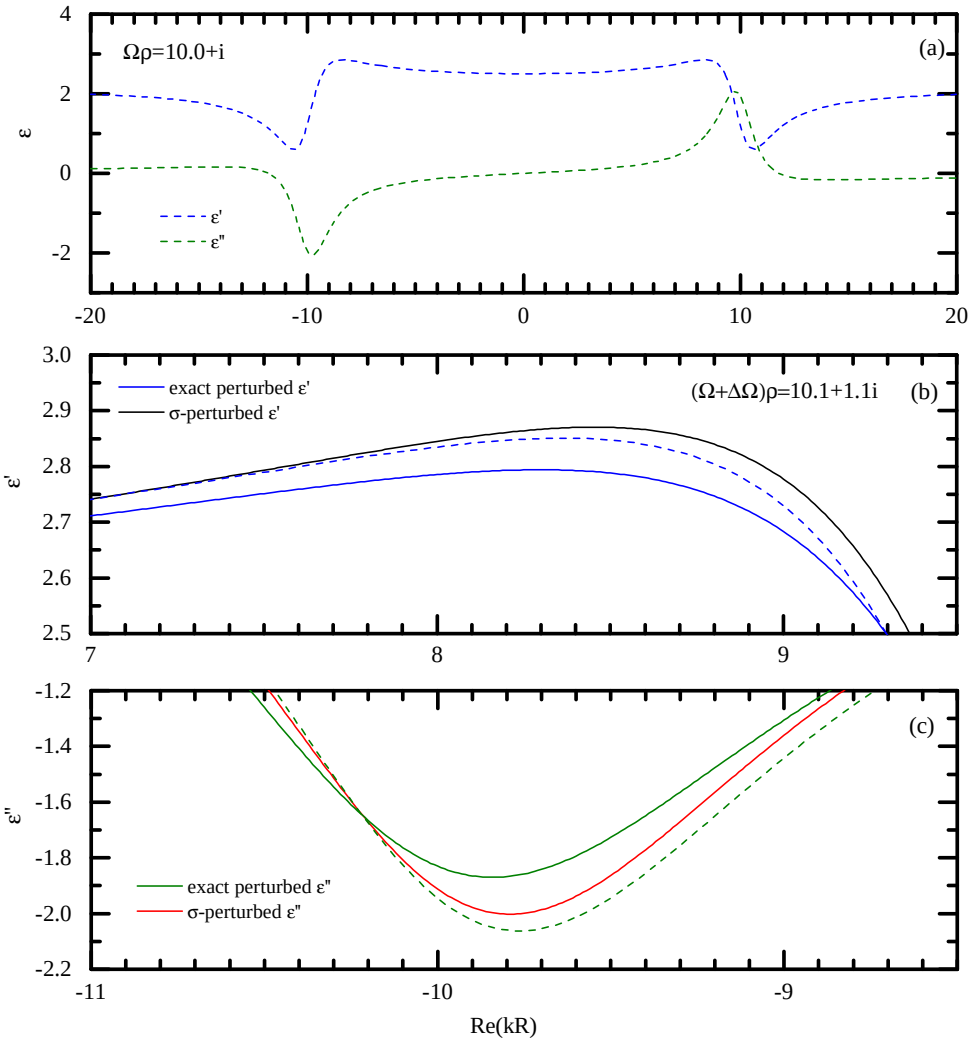

Figure 3.8: (a) Real and imaginary parts of the unperturbed permittivity for an ε with a single Lorentz pole. We use $\rho = R/c$ to maintain units. (b) Comparison between unperturbed, exact perturbed and σ-perturbed for ε' at resonance. (c) As (b) but for ε''.

Using Eq. (3.71) we have an expression for $\widetilde{\sigma}(\Delta\Omega)$. This is what we call σ-perturbation for the pole position Ω. Fig. 3.8 shows comparison between the σ-perturbation and the exact solution found using Eq. (3.38). We can see that the solution match poorly. For ε' we can even see that, at the resonance, the σ-perturbed solution has a much higher ε' than the unperturbed ε', moving the opposite way to the exact perturbed solution.

3.7.2 1st-order perturbation

A simple method we developed was to use the pole-related RSs for the original pole position to reproduce the pole-related RSs for the perturbed pole position. This is achieved by only using the diagonal elements of the matrix equation which translates to a 1st-order perturbation. The reasoning behind this is that the pole-related RSs dominate and all off-diagonal terms are negligible due to a very small perturbation.

If we look at Eq. (3.20), we can take $n = m$ and write a much simpler equation for the pertubed RSs

$$k_n = k\left(\frac{2}{2 + U_{nn}}\right) \tag{3.72}$$

which is the diagonal matrix problem for 1st-order perturbations using the RSE. In this case $V_{nn} = 0$ and

$$U_{nn} = \left[\frac{1}{k_n - \widetilde{\Omega}} - \frac{1}{k_n - \Omega}\right] \int \mathbf{E}_n(\mathbf{r}) \cdot \hat{\boldsymbol{\sigma}}_j(\mathbf{r}) \mathbf{E}_m(\mathbf{r})\, d\mathbf{r} \tag{3.73}$$

where $\widetilde{\Omega}$ is the perturbed pole position.

We previously described, in Sec. 3.4, that one method would be to have the all of the pole-related RSs in the basis for both the original pole location and the perturbed location. Simply by "turning" one pole position on an the other off we would be able to accurately demonstrate pole position change. This is a computationally inefficient method though and here we show that you only need to find the pole-related RSs for the unperturbed pole position and these are enough to reproduce most of the perturbed RSs. The argument here is while the perturbed pole-related RSs are different than the unperturbed ones, the wavefunctions are similar enough that for small pole position changes ($\sim 1\%$) we can use them in the RSE to approximate the RSs.

Fig. 3.9 shows that the RSE solution will converge with the exact solution as you get to modes which are further away from the Lorentz pole. As expected we do not get perfect convergence which would require another set of basis states at the new pole location, but many modes can be reproduced if the perturbation is small enough.

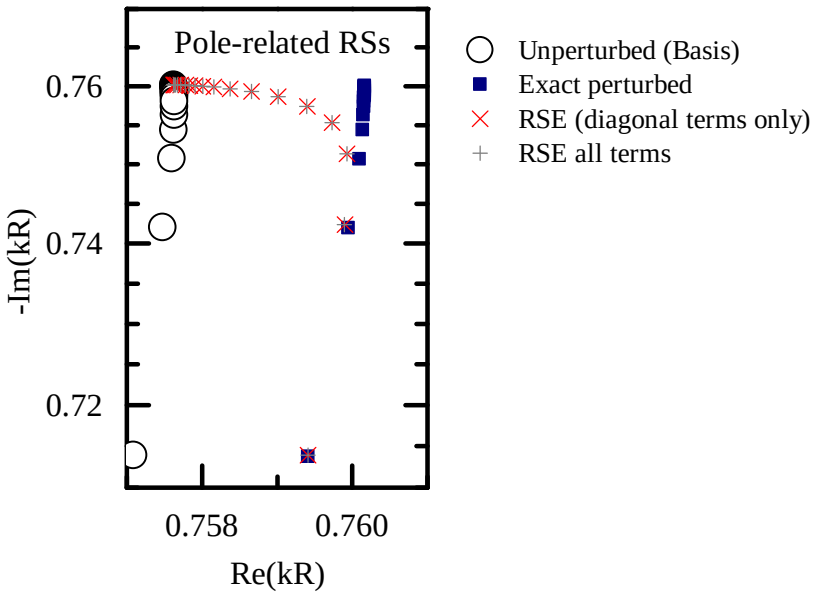

Figure 3.9: Frequency-space graph showing the pole-related RSs for 1st-order pole position perturbation of $\sim 1\%$.

We show the RSE with all terms in the perturbation matrix as well as the RSE with diagonal terms only as they will dominate in a set up such as this. The off-diagonal terms which correspond the normal RSs have very little influence on the RSE result. This is seen by both verisons of the RSE agreeing very well. While this is not an ideal solution for the problem of the pole position shifting it demonstrates the ability to produce meaningful results using the RSE for such situations. The physical properties in scattering and absorption are expected to be dominated by the RSs further way from the poles, as they contain a larger fraction of external field - close to the pole the permittivity is very high, screening the outside field. Furthermore, for the response at real frequencies the specific position of the RSs close to the poles are expected to be of minor influence.

These are qualitative arguments, the efficiency of this method should be investigated in a scattering calculation along [18] .

3.8 Summary

In this chapter we show the previously published methods of how to find the eigenmodes of a dielectric sphere modified for one with frequency dispersion. We show

Material	Au	GaAs (phonon range)	GaAs (band gap range)
ε_∞	0.5	11.0	8.6013
γ(eV)	-0.065748	–	–
σ(eV)	1133.0	–	–
Ω_1'(eV)	2.5936	0.033314	1.497
Ω_1''(eV)	-0.41875	1.4904×10^{-4}	-0.03665
σ_1'(eV)	1.4029	0.0	0.0
σ_1''(eV)	0.76857	0.033262	0.01224
Ω_2'(eV)	3.8192	–	1.5612
Ω_2''(eV)	-1.3246	–	-0.05643
σ_2'(eV)	0.41939	–	0.0
σ_2''(eV)	4.5468	–	0.02432
Ω_3'(eV)	9.6899	–	1.6463
Ω_3''(eV)	-4.2933	–	-0.0457
σ_3'(eV)	0.012244	–	0.0
σ_3''(eV)	14.817	–	0.02404
Ω_4'(eV)	–	–	2.2853
Ω_4''(eV)	–	–	-0.00778
σ_4'(eV)	–	–	0.0
σ_4''(eV)	–	–	2.9302
$\hbar\omega_1$(eV)	0.64	0.031	1.3
$\hbar\omega_N$(eV)	6.6	0.0372	1.65
$2N$	49	47	8
S	1.4795	0.0372	0.0055

Table 3.1: Optimized model parameters for Au and GaAs (phonon and optical ranges), using the fit function with optimization energy ranges corresponding to the data shown in Figs. 3.3, 3.6 and 3.7, and 3.5. The number of data values $2N$ and the resulting error S are also given. For gold the experimental errors were used leading to a higher value for S.

the extension of the RSE to work with frequency dispersion in the basis along with associated normalisations, by using the Drude-Lorentz model for the permittivity. Using arbitrary parameters in the DL model, we show the accuracy of the RSE for dispersive nanospheres. We extend the RSE further by introducing the infinitesimal-dispersive basis, which allows us to perturb a dielectric material to one with frequency dispersion. This is tested using realistic parameters, for Au and GaAs, found using the fit program we develop, shown in chapter 2. We also show the evolution of surface plasmons in Au and model gain in energy for GaAs. With regards to the problem of pole position perturbation, we show an attempt at an analytic solution and a much simpler method using only 1^{st}-order perturbation.

Chapter 4

Conclusion

We started with the RSE method developed to be able to reproduce the perturbed eigenmodes of a dielectric sphere and the goal of this thesis was to further develop this method to include materials with frequency dispersion modelled using the Drude-Lorentz model. We wanted to model realistic materials so created a fit program to reliably provide accurate parameters for measured data of dispersive materials.

4.1 Fit program

We have presented an optimisation algorithm to determine the parameters of a generalised Drude-Lorentz model for the permittivity of materials. For L pairs of Lorentz poles and D Drude poles taken into account, the developed algorithm uses an analytic minimisation over the $2L + D + 1$ linear parameters of the model (the generalised conductivities and high frequency value ε_∞), and a gradient descent method for determining the $2L + D$ nonlinear parameters of the model (the Drude and Lorentz pole frequencies), with a suited choice of the starting values, resulting in fast and reliable determination of the best global fit.

Comparing our results with previous literature[26], we find that the weighted error is improved by a factor of two for the same number of poles. For gold, we find that the Drude model is sufficient up to photon energies of 2 eV, one additional pair of Lorentz oscillators up to 2.6 eV, two up to 4.8 eV, and three up to 6.5 eV. We

provide parameters for more materials in the Appendix, including a recent dataset for monocrystalline gold[32].

We have also demonstrated the performance of our optimisation algorithm to determine the parameters for the permittivity of semiconductors, which can be modeled with Lorentz poles only. For L pairs of Lorentz poles taken into account, the developed algorithm uses an analytic minimisation over the $2L+1$ linear parameters of the model. Examples of the fit using up to 5 pairs of Lorentz poles are provided for Si, GaAs and Ge.

The optimisation program implementing the described algorithm is provided [24] for modelling any measured data for the refractive index or permittivity.

4.2 Dispersive RSE

We show the RSE method for using a frequency-dependent permittivity modelled using the DL model. We show the accuracy of the dispersive RSE due to the error scaling as N^{-3}, similar to the dielectric case, where N is the number of basis modes. They also show the phenomenon of pole-related RSs, which are required for the high accuracy of the RSE. We introduce the infinitesimal-dispersive RSE which allows us to perturb a dielectric material into one with frequency dispersion by having the required pole-related RSs exist in the basis with zero weight.

Using our fit program for the accurate parameters, we fit gold with one pole and three Lorentz poles. We perturb a 10nm nanosphere of sand, with these poles in the basis, into a gold nanosphere showing the error also scaling as N^{-3}. We also analyse the evolution of the surface plasmons showing the interference of the first and second SP around 80nm radius.

As with gold, we use the fit program to fit the phonon range, 31-37.2 meV, for GaAs with a single Lorentz pole, and perturb a dielectric 50μm sphere to GaAs. We also see two sets of WGMs either side of the resonance after perturbation. Fitting the band gap range of GaAs, 1.3-1.65 eV, we perturb $\sigma_1 \to -\sigma_1$ resulting in gain. For a sphere of 10μm we see the refractive index decrease approaching the resonance limiting the number of modes and causing a circular set of modes at the resonance.

For a sphere of 940nm we line the resonance up with a WGM causing it to shift to the positive imaginary part after perturbation.

We also show an attempt to incorporate a pole position perturbation into a $\Delta\sigma$ perturbation. While this was unsuccessful we provide a successful method using 1^{st}-order perturbation which, for small position perturbations (1%), reproduces the perturbed modes with greater accuracy the further the modes are from the resonance.

4.3 Future work

We plan to publish the work covered in chapter 3 in a paper showing the infinitesimal-dispersive RSE, the evolution of SPs and modelling gain in GaAs. The development of the RSE is still ongoing and we want to have it as a tool to use the optical resonances of gold nanoparticles as the basis for advanced biosensors. The fit program will continue to be updated to include more options, there is also strong interest for it to be included in an open source integrated photonics toolbox as the interface between data and solver.

Appendix A

Derivation of the Drude model

First we define how material polarisation $\vec{P}$ is taken account of in the electric field displacement,

$$\vec{D} = \varepsilon_0 \vec{E} + \vec{P} = \varepsilon_0 \varepsilon \vec{E} = \varepsilon_0 \vec{E} + \varepsilon_0 \chi \vec{E}\,, \tag{A.1}$$

where ε_0 is the permittivity of free space and ε is the relative permittivity. From Eq. (A.1) we can write

$$\vec{P} = \varepsilon_0 \chi \vec{E} \tag{A.2}$$

$$\varepsilon = 1 + \chi \tag{A.3}$$

where χ is the susceptibility.

Using the idea of resonance and simple harmonic motion we can use the equation of motion of a displaced electron, where $\vec{r}$ is the displacement, as a starting point to derive the Drude model.

$$\underbrace{m\frac{\partial^2 \vec{r}}{\partial t^2}}_{\substack{\text{acceleration force}\\ \text{where } m{=}m_e\\ \text{(mass of electron)}}} + \underbrace{m\Gamma\frac{\partial \vec{r}}{\partial t}}_{\substack{\text{frictional force}\\ \text{where } \Gamma \text{ is the}\\ \text{damping rate}}} + \underbrace{m\omega_0^2 \vec{r}}_{\substack{\text{restoring force}\\ \text{where } \omega_0 \text{ is the}\\ \text{natural frequency}}} = \underbrace{-q\vec{E}}_{\text{electric force}} \tag{A.4}$$

We want to use the Drude model for modelling metals primarily so we assume free electrons which are not bound to the nucleus. This gives us a negligible restoring force and we do not have a natural frequency removing the third term from Eq. (A.4). We can now take the Fourier Transform of Eq. (A.4) which, after simplification, gives

us

$$\left(-m_e\omega^2 - i\omega m_e\Gamma\right)\vec{r}(\omega) = -q\vec{E} \tag{A.5}$$

which we can rearrange to give us the displacement

$$\vec{r}(\omega) = \frac{-q\vec{E}(\omega)}{m_e(-\omega^2 - i\omega\Gamma)}. \tag{A.6}$$

We then use the definition for the electric dipole moment to give us

$$\vec{d}(\omega) = -q\vec{r}(\omega) = \frac{q^2\vec{E}(\omega)}{m_e(-\omega^2 - i\omega\Gamma)}. \tag{A.7}$$

By linking the electric dipole moment ($\vec{d}$) and the electric field ($\vec{E}$) we arrive at an expression for the polarisability for a single electron $\alpha(\omega)$

$$\vec{d}(\omega) = \alpha(\omega)\vec{E}(\omega) \tag{A.8}$$

$$\alpha(\omega) = \frac{q^2}{m_e(-\omega^2 - i\omega\Gamma)}. \tag{A.9}$$

We now need to define the polarisation per unit volume V as a function of the average dipole moment over N electrons

$$\vec{P}(\omega) = \frac{1}{V}\sum_V \vec{d}_i(\omega) = N\left\langle \vec{d}_i(\omega)\right\rangle \tag{A.10}$$

to give us an expression for the susceptibility which is frequency dependent. Using Eq. (A.2), Eq. (A.8), Eq. (A.9) and Eq. (A.10) we can say

$$\chi(\omega) = \frac{N\alpha(\omega)}{\varepsilon_0} = \left(\frac{Nq^2}{\varepsilon_0 m_e}\right)\frac{1}{-\omega^2 - i\omega\Gamma} = \frac{\omega_p^2}{-\omega^2 - i\omega\Gamma} \tag{A.11}$$

where the plasma frequency is

$$\omega_p^2 = \frac{Nq^2}{\varepsilon_0 m_e}. \tag{A.12}$$

Recall that $\varepsilon(\omega) = 1 + \chi(\omega)$ and we can write

$$\varepsilon(\omega) = 1 - \frac{\omega_p^2}{\omega^2 + i\omega\Gamma} \tag{A.13}$$

for a material in a vacuum. This is essentially the Drude model, however for our purposes we have a background permittivity greater than that of free space ε_∞ which effectively takes into account the background effect of the other resonances, at higher frequencies, not treated. We also rewrite the plasma frequency as $\omega_p^2 = \sigma\Gamma$ where σ is the conductivity. This gives us the expression we use as the Drude model

$$\varepsilon(\omega) = \varepsilon_\infty - \frac{\sigma\Gamma}{\omega^2 + i\omega\Gamma} \tag{A.14}$$

which is identical to Eq. (1.25).

Using the Drude model, an isolated electron will accumulate momentum as it travels. If we neglect the momentum of the electron the expression for the current density is

$$\vec{J}(\omega) = -Nq\vec{r}(\omega) \tag{A.15}$$

which, using Eq. (A.6) and then Eq. (A.12), we can rewite as

$$\vec{J}(\omega) = i\omega\frac{Nq^2}{m_e}\frac{\vec{E}(\omega)}{\omega(\omega + i\gamma)} = i\omega\frac{\varepsilon_0\omega_p^2\vec{E}(\omega)}{\omega(\omega + i\gamma)}\,. \tag{A.16}$$

Usings Ohm's Law $\vec{J}(\omega) = \sigma(\omega)\vec{E}(\omega)$ we can writer an expression for the conductivity $\sigma(\omega)$

$$\sigma(\omega) = \frac{i\omega\varepsilon_0\omega_p^2}{\omega(\omega + i\gamma)}\,. \tag{A.17}$$

From Eq. (A.11), we can see that $\sigma(\omega) = i\varepsilon_0\chi(\omega)$ which in turn can be rewritten, using Eq. (A.3), as the Ohm's Law dispersion permittivity $\varepsilon(\omega)$

$$\varepsilon(\omega) = \varepsilon_0 + \frac{i\sigma}{\omega}. \tag{A.18}$$

Fig. A.1 shows the comparison of the Ohm's Law Eq. (A.18) and the Drude model Eq. (A.14). While the Ohm's Law is very similar to the Drude model for ε' at high

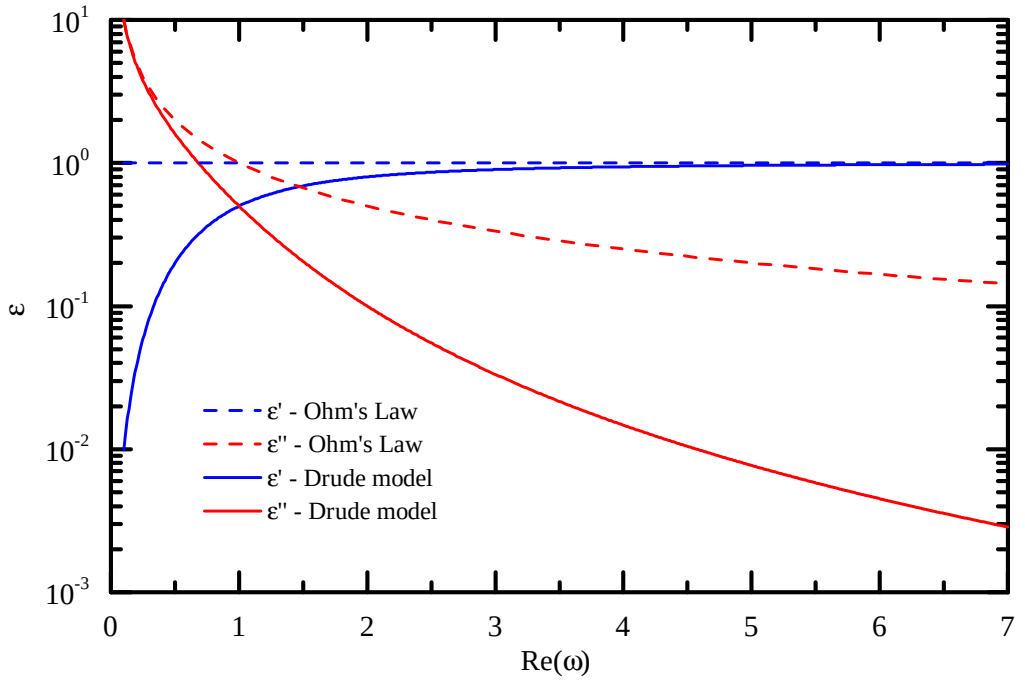

Figure A.1: Ohm's Law permittivity and the Drude model where $\varepsilon_\infty = 1$, $\sigma = 1$ and $\gamma = 1$. We also take $\hbar = c = 1$.

frequencies, it is unsuitable for the lower frequencies where the Drude model can describe the high electron density in metals much better as shown in chapter 2.

Appendix B

Results for semiconductors cont.

Here we show the results of the fit program for GaAs and Ge in a similar style to Si (Fig. 2.11 and Fig. 2.12).

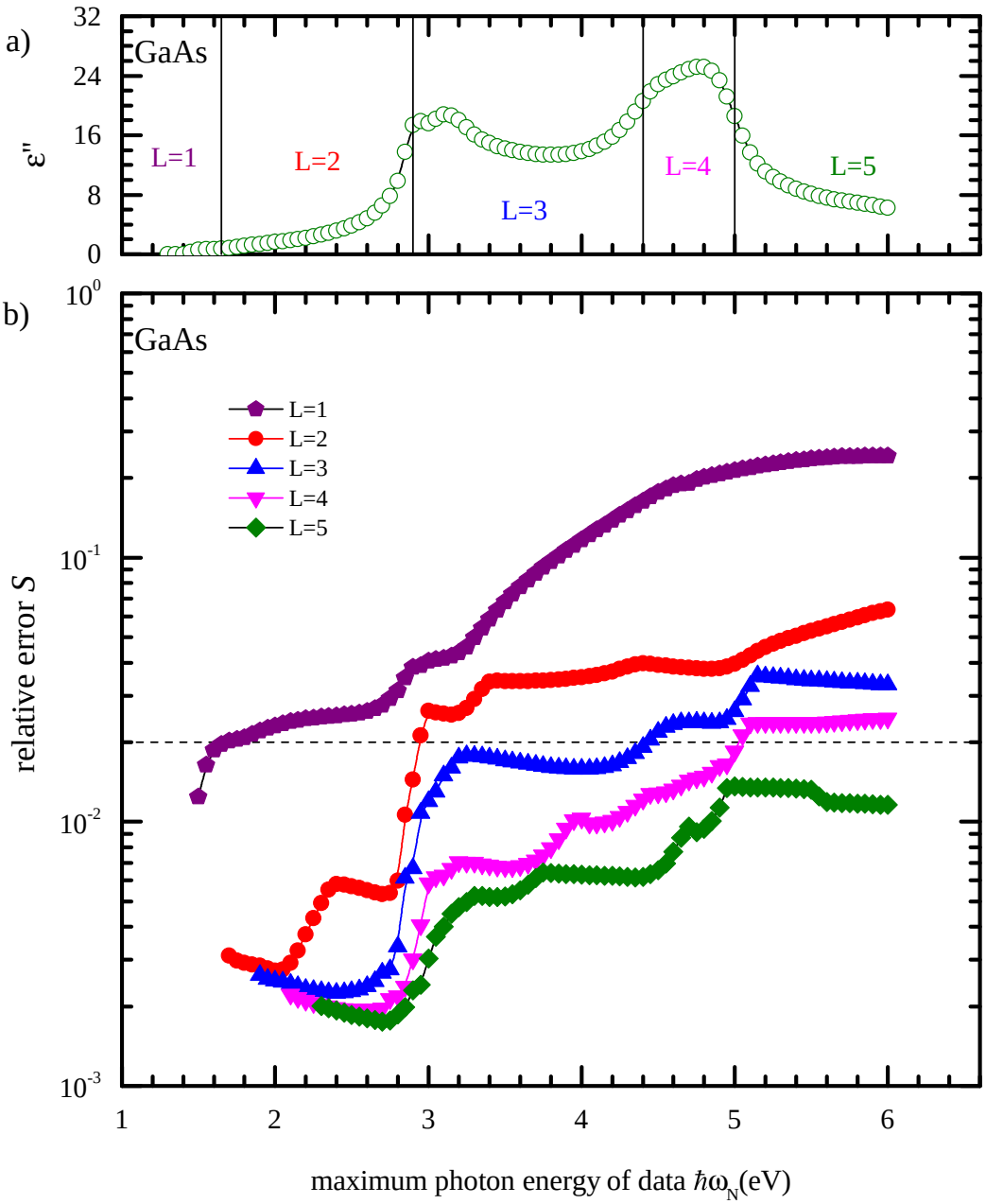

Figure B.1: As Fig. 2.11, but for GaAs.

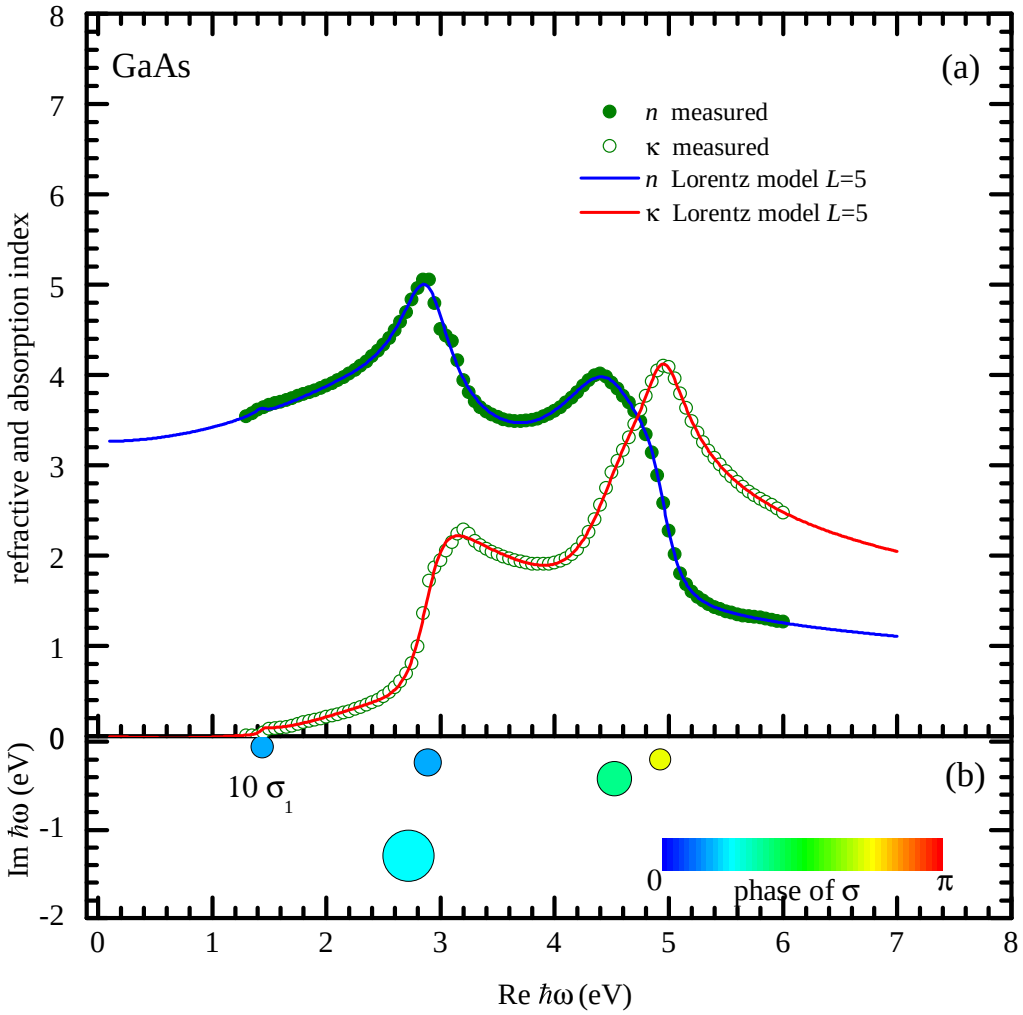

Figure B.2: As Fig. 2.12, but for GaAs and optimised for the full data range of $\hbar\omega$ given in[33], from 1.3 eV to 6.0 eV.

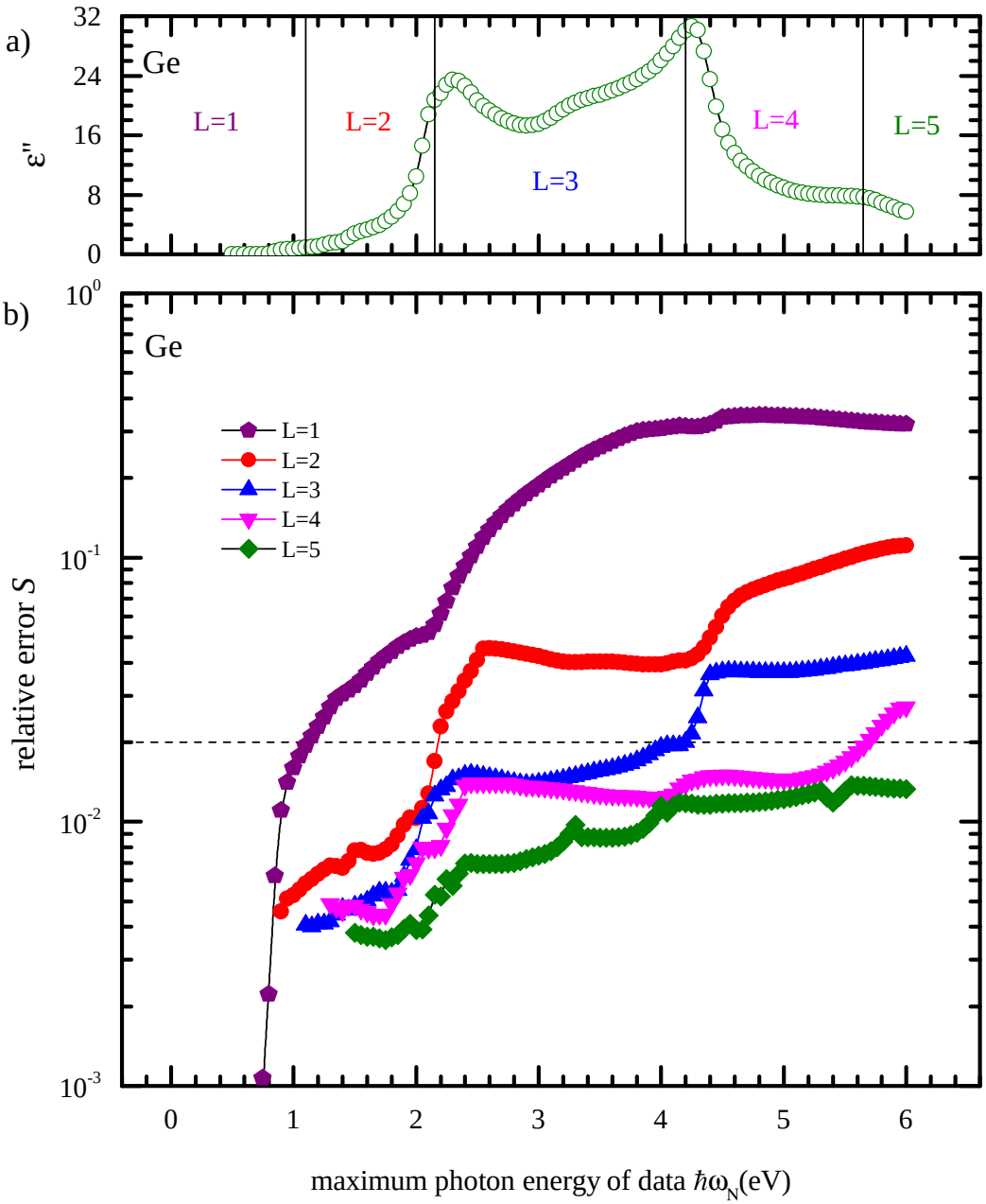

Figure B.3: As Fig. 2.11, but for Ge.

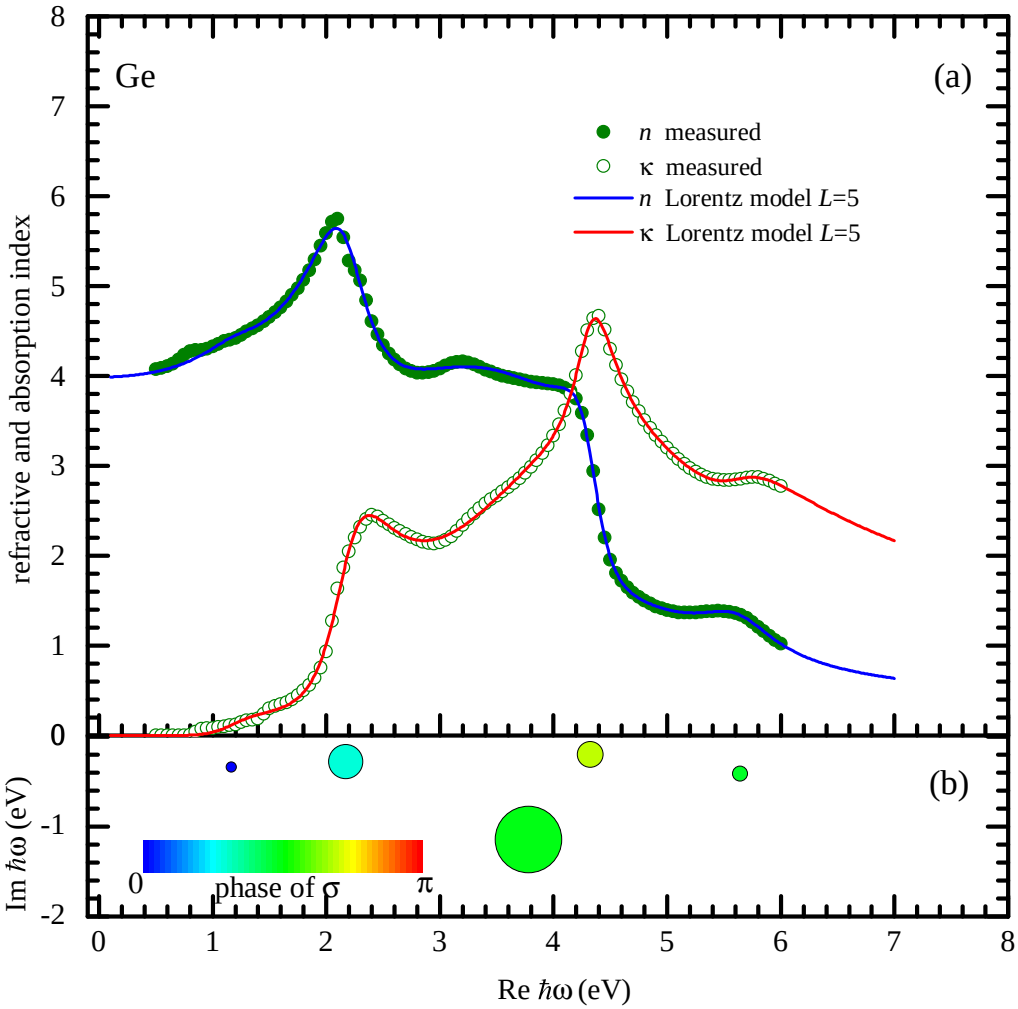

Figure B.4: As Fig. 2.12, but for Ge and optimised for the full data range of $\hbar\omega$ given in[33], from 0.5 eV to 6.0 eV.

List of Figures

List of Tables

Bibliography

[1] G Gamow. Zur Quantentheorie des Atomkernes. *Zeitschrift für Physik*, 51(3):204–212, 1928.

[2] A J F Siegert. On the Derivation of the Dispersion Formula for Nuclear Reactions. *Phys. Rev.*, 56(8):750–752, oct 1939.

[3] Lev Albertovich Weinstein and David Dutton. Open Resonators and Open Waveguides, 1970.

[4] E A Muljarov, W Langbein, and R Zimmermann. Brillouin-Wigner perturbation theory in open electromagnetic systems. *EPL*, 92(5), 2010.

[5] M B Doost, W Langbein, and E A Muljarov. Resonant-state expansion applied to three-dimensional open optical systems. *Physical Review A - Atomic, Molecular, and Optical Physics*, 90(1):1–14, 2014.

[6] Schrödinger E. Quantisierung als Eigenwertproblem. *Annalen der Physik*, 384(6):489–527, jun 1926.

[7] Hiu Lai, P T. Leung, Kenneth Young, P W. Barber, and S C. Hill. *Time-independent perturbation for leaking electromagnetic modes in open systems with application to resonances in microdroplets*, volume 41. jun 1990.

[8] H M Lai, C C Lam, P T Leung, and K Young. Effect of perturbations on the widths of narrow morphology-dependent resonances in Mie scattering. *Journal of the Optical Society of America B*, 8(9):1962–1973, 1991.

[9] K M Lee, P T Leung, and K M Pang. Iterative perturbation scheme for

morphology-dependent resonances in dielectric spheres. *Journal of the Optical Society of America A*, 15(5):1383–1393, 1998.

[10] P T Leung, S Y Liu, S S Tong, and K Young. Time-independent perturbation theory for quasinormal modes in leaky optical cavities. *Phys. Rev. A*, 49(4):3068–3073, apr 1994.

[11] P T Leung and K M Pang. Completeness and time-independent perturbation of morphology-dependent resonances in dielectric spheres. *Journal of the Optical Society of America B*, 13(5):805–817, 1996.

[12] R Dubertrand, E Bogomolny, N Djellali, M Lebental, and C Schmit. Circular dielectric cavity and its deformations. *Physical Review A*, 77(1):13804, jan 2008.

[13] Mark B Doost, Wolfgang Langbein, and Egor Muljarov. Resonant state expansion applied to two-dimensional open optical systems. *Physical Review A - Atomic, Molecular, and Optical Physics*, (February), 2013.

[14] L J Armitage, M.Â B. Doost, W.Â Langbein, and E.Â A. Muljarov. Resonant-state expansion applied to planar waveguides. *Physical Review A*, 89(5):53832, may 2014.

[15] S C Hagness, D Rafizadeh, S T Ho, and A Taflove. FDTD microcavity simulations: design and experimental realization of waveguide-coupled single-mode ring and whispering-gallery-mode disk resonators. *Journal of Lightwave Technology*, 15(11):2154–2165, 1997.

[16] Jan Wiersig. Boundary element method for resonances in dielectric microcavities. *Journal of Optics A: Pure and Applied Optics*, 5(1):53, 2003.

[17] B M A Rahman, F A Fernandez, and J B Davies. Review of finite element methods for microwave and optical waveguides. *Proceedings of the IEEE*, 79(10):1442–1448, 1991.

[18] S V Lobanov, W Langbein, and E A Muljarov. Resonant-state expansion of three-dimensional open optical systems: Light scattering. (Ml):1–18, 2018.

[19] Roger G Newton. Analytic Properties of Radial Wave Functions. *Journal of Mathematical Physics*, 1(4):319–347, jul 1960.

[20] R M More. Theory of Decaying States. *Physical Review A*, 4(5):1782–1790, nov 1971.

[21] L.D. LANDAU and E.M. LIFSHITZ. Electrostatics of Dielectrics. In L D LANDAU and E M B T Electrodynamics of Continuous Media (Second Edition) LIFSHITZ, editors, *Electrodynamics of Continuous Media*, volume 8, pages 34–85. Pergamon, Amsterdam, 1984.

[22] P B Johnson and R W Christy. Optical Constants of the Noble Metals. *Physical Review B*, 6(12):4370–4379, dec 1972.

[23] P G Etchegoin, E C Le Ru, and M Meyer. An analytic model for the optical properties of gold. *Journal of Chemical Physics*, 125(16):1–4, 2006.

[24] H S Sehmi, W Langbein, and E A Muljarov. Optimizing the Drude-Lorentz model for material permittivity: Method, program, and examples for gold, silver, and copper. *Physical Review B*, 95(11):1–8, 2017.

[25] H S Sehmi, Wolfgang Langbein, and E A Muljarov. Optimizing the Drude-Lorentz model for material permittivity: Examples for semiconductors. In *Progress in Electromagnetics Research Symposium*, volume Part F1343, pages 994–1000, 2017.

[26] Alexandre Vial and Thierry Laroche. Description of dispersion properties of metals by means of the critical points model and application to the study of resonant structures using the FDTD method. *Journal of Physics D: Applied Physics*, 40(22):7152–7158, 2007.

[27] E A Muljarov and Wolfgang Langbein. Exact mode volume and Purcell factor of open optical systems. *Physical Review B*, (23), 2016.

[28] a D Rakic, a B Djurisic, J M Elazar, and M L Majewski. Optical properties of metallic films for vertical-cavity optoelectronic devices. *Applied optics*, 37(22):5271–5283, 1998.

[29] A Vial and T Laroche. Comparison of gold and silver dispersion laws suitable for FDTD simulations. *Applied Physics B: Lasers and Optics*, 93(1):139–143, 2008.

[30] A Vial, T Laroche, M Dridi, and L Le Cunff. A new model of dispersion for metals leading to a more accurate modeling of plasmonic structures using the FDTD method. *Applied Physics A: Materials Science and Processing*, 103(3):849–853, 2011.

[31] J W Allen and J C Mikkelsen. Optical properties of CrSb, MnSb, NiSb, and NiAs. *Physical Review B*, 15(6):2952–2960, mar 1977.

[32] Shaista Babar and J H Weaver. Optical constants of Cu , Ag , and Au revisited. 54(3):477–481, 2015.

[33] The data for the measured indices of light refraction and absorption is taken from http://sspectra.com/sopra.html.

[34] E A Muljarov and Wolfgang Langbein. Resonant-state expansion of dispersive open optical systems: Creating gold from sand. *Physical Review B*, 93(7), 2016.

[35] E M Purcell, H C Torrey, and R V Pound. Resonance Absorption by Nuclear Magnetic Moments in a Solid. *Physical Review*, 69(1-2):37–38, jan 1946.

[36] Julius Adams Stratton 1901-. *Electromagnetic theory / by Julius Adams Stratton.* International series in physics. McGraw-Hill, New York, 1941.

[37] S S Martinos. Surface electromagnetic modes in metal spheres. *Physical Review B*, 31(4):2029–2032, feb 1985.

[38] Filippo Alpeggiani, Stefania D'Agostino, and Lucio Claudio Andreani. Surface plasmons and strong light-matter coupling in metallic nanoshells. *Physical Review B*, 86(3):35421, jul 2012.

[39] Viktor Myroshnychenko, Jessica Rodriguez-Fernandez, Isabel Pastoriza-Santos, Alison M Funston, Carolina Novo, Paul Mulvaney, Luis M Liz-Marzan, and

F Javier de Abajo. Modelling the optical response of gold nanoparticles. *Chem. Soc. Rev.*, 37(9):1792–1805, 2008.

[40] J S. Blakemore. *Semiconducting and Other Major Properties of Gallium Arsenide*, volume 53. nov 1982.